



Master's Thesis 45 ECTS

Transport Properties and Derived Effects of Neutrals in Turbulent Edge Plasma

Design and implementation of the discrete particle model PISAM
and its coupling with the 2D turbulent edge plasma model HESEL

Author: Kristoffer Kvist

In collaboration with Department of Physics, DTU

Internal Supervisor: Troels Haugbølle

External Supervisors: Anders Henry Nielsen & Alexander Simon Thrysøe

The PISAM-HESEL code is available at:

<https://github.com/kristofferkvist/PISAM-HESEL>

Submitted: March 2023

Abstract

On the low field side of magnetically confined fusion devices, field perpendicular transport is dominated by advective turbulent motion in the vicinity of the last closed flux surface. Minimizing this turbulence is paramount in designing profitable fusion reactors, and producing sustainable energy on a commercial scale. This thesis investigates the transport properties and derived effects of deuterium atoms and molecules in turbulent edge plasma. Detailed knowledge about the behavior of neutrals in fusion plasma is necessary to assess the efficiency of fueling systems and understand recycling processes and their influence on the plasma.

This work presents the development and implementation of the discrete particle model PISAM (**P**lasma **I**nteracting **S**uper **A**toms and **M**olecules) and its coupling to the fluid model HESEL (**H**ot **E**dge **S**OL **E**lectrostatic), designed to describe plasma edge turbulence at the outboard midplane of a Tokamak. To account for the introduction of neutral source terms in HESEL, the neutral augmented HESEL equations (nHESEL) are derived from first principles. As part of this derivation, several mistakes, regarding higher-order terms, in their current formulation are corrected.

PISAM is the manifestation of an attempt to close the gap between physically inadequate but numerically tractable fluid models and precise but slow kinetic Monte Carlo solvers. Numerical tractability is ensured by performing justified approximations to reformulate the description of neutrals interacting with a fusion plasma as an embarrassingly parallel problem. The implementation of PISAM is in close analogy with our understanding of gas as a collection of free particles with short-range interactions. This simplicity combined with the application of the most recent quantum mechanical data describing the interactions between neutrals and plasma particles makes PISAM a reliable alternative to current neutral models. The MPI parallel Python implementation of PISAM is coupled with a C++ implementation of HESEL using MPI. An MPI coupling of python with C++ is in itself pioneering work and is shown to yield excellent communication speed and reliable operation in simulations conducted using the coupled PISAM-HESEL model on the HPC cluster Marconi. The results of these simulations serve as a persuading verification of PISAM's ability to supply HESEL with source terms from inelastic plasma-neutral interactions. The source terms provided by PISAM illuminate the underlying mechanisms of transport phenomena mediated by neutrals with great clarity. The measured influences of neutrals on the plasma field profiles are found to be in great qualitative agreement with previous measurements and detailed kinetic simulations.

Contents

1	Introduction	1
1.1	Fusion Power	1
	Limitations in Supporting Fuel Consumption of Fusion Reactors	2
	Energy Balance of a Fusion Reactor	2
1.2	The Tokamak	4
1.3	Anomalous Transport	6
1.4	Interchange Dynamics	7
1.5	Neutrals and Plasmas	11
1.6	Modeling Neutrals	12
2	Plasma Fluid Theory	14
2.1	The Boltzmann Equation	14
2.2	Transport equations	15
	Moments of velocity	16
3	Collision Theory	20
3.1	Collision Rate of a Single Particle Interacting with a Fluid	20
	Electron-Neutral Collisions	21
	Ion-Neutral Collisions	22
3.2	Elastic Binary Collisions in Fluids	25
	Steady State of a Fluid	25
	Relaxation time	29
	Relaxation of Neutrals	30
4	The nHESEL Equations	31
4.1	Fluid Closure	31
	Conditions of Applicability	34
4.2	Drift Ordering	35
4.3	Specifications for the HESEL Model	38
	Domain and Field Geometry	39
	Thin Layer Approximation and Similar Approximations	39

Approximations to Perpendicular Diffusion	40
Approximations to Heat Transport Terms	41
Parameterization of Parallel Dynamics	41
4.4 Model equations	42
4.5 Dimensionality of HESEL	45
5 PISAM	46
5.1 Overview of Reaction Channels	47
5.2 Atoms	47
Excitation and Ionization of the Deuterium Atom	47
Charge Exchange of Deuterium Atoms and Deuterium Ions	51
5.3 Molecules	54
Molecular Dissociation Into Neutral Fragments (MD)	55
Ionization of Molecular Deuterium	63
Molecular Ion Dissociation (MID)	64
6 Numerical Implementation	73
6.1 Implementation of PISAM in Python	73
Neutral Injection and Boundary Conditions	74
Calculating Decay Probabilities from Decay Frequencies	75
Advantages and Drawbacks of using Python	75
6.2 Implementation of HESEL in BOUT++	76
6.3 Parallelization and Coupling	77
Parallelization of PISAM	77
Coupling of PISAM with HESEL	78
7 Timestep Determination and Estimation of Neglected Collisions	80
7.1 Qualitative Verification	80
7.2 Time Step Determination	82
7.3 Particle Weight and Source Smoothing	85
Smoothing	86
Locality of Inelastic Collisions	87
Numerical Measure of Smoothness	88
7.4 Elastic Collisions Between Neutrals and Plasma Particles	90
Elastic Electron-Neutral Collisions	91
Elastic Ion-Neutral Collisions	92
7.5 Radiative Recombination	93
8 Results	95

8.1	PISAM with Static Fields	95
	Plasma Density Source	95
	Electron Energy Density Source	95
	Ion Energy Density Source	96
8.2	PISAM-HESEL	97
	Source Terms Provided by PISAM	98
	Plasma Density and Temperature Profiles	103
8.3	Influence of Neutrals on the Electric Field	103
8.4	Neutral Densities	105
9	Discussion	108
9.1	Including Vibrational States	108
9.2	Momentum Transfer Mediated by Neutrals	109
9.3	Coupling of Models with Different Dimensionalities	109
9.4	Coupling a Discrete Model with a Continues Model	110
9.5	Optimal Conditions and Injection Temperature	111
9.6	Future Experiments	112
9.7	Beyond the Outboard Midplane and Beyond Fusion Plasma .	113
10	Conclusion	114
References		117
Appendix A : Definitions in Kinetic Theory		129
A.1	Average Macroscopic Variables	129
A.2	Generalized Pressure	130
A.3	The Viscous Stress Tensor	130
Appendix B : Derivation of the Boltzmann Collision Operator		132
Appendix C : Asymmetry of Charge Exchange Reactions		135
C.1	Validation	136
C.2	Asymmetry	136
Appendix D : Design of the PISAM Implementation		138

1 Introduction

Due to economic growth and an increasing human population the demand for electronic devices, household heat and electricity, non-local groceries, and personal transport is rising, [1]. As a consequence, the demand for energy is as well, [2]. Unfortunately, this development in itself seems inevitable. If the heating of the globe is to be minimized, the energy needed to meet this increased demand must be supplied by cheap sustainable energy sources. The current sustainable energy sources all have drawbacks making them unfit to sustain a reliable power grid by themselves. The output of wind and solar power is highly volatile to weather conditions meaning that energy conservation methods, far more efficient than those available today, are a necessity to ensure the security of the power supply. Furthermore, the small asynchronous turbines of windmills are unfit to sustain a stable AC current in the power grid, by current technologies, [3]. Fission energy overcomes these problems, but leaves undesired radioactive waste, and generally meets public skepticism due to previous accidents such as those of Chernobyl and Fukuyama, [4]. Certain characteristics of fusion power have elevated it to the status of the ultimate sustainable energy source. The reasons for this optimism as well as the current challenges are outlined in the following section.

1.1 Fusion Power

Fusion devices currently being designed and build produce energy through deuterium(²H)-tritium(³H) fusion

$$D + T \rightarrow \alpha(3.5\text{MeV}) + n(14.1\text{MeV}), \quad (1.1)$$

where α denotes a ⁴He nucleus. This fusion reaction is targeted due to its ease of initiation in comparison to other fusion reactions [5, 6].

Limitations in Supporting Fuel Consumption of Fusion Reactors

The fusion reaction of (1.1) immediately leads to a drawback of fusion power regarding long-term sustainability. Tritium is β^- unstable with a half-life of 12.33 years, [7], resulting in very little tritium being present on earth. As a consequence tritium is bred from ^6Li , [8]



The reserves of lithium on earth are limited, and the metal is already requested by several industries. By current lithium extraction techniques, the timescale on which the lithium need of fusion can be supplied is of the order of hundreds of years [9]. However, at that time the technology of magnetic plasma confinement might be mature enough for other fusion reactions to be ignited in fusion reactors. Should we become able to master deuterium-deuterium fusion, the abundance of deuterium in seawater would make fusion a practically inexhaustible energy source.

Energy Balance of a Fusion Reactor

The general challenge in fusion research is to contain the energy of the plasma to an extent where the energy loss at the confinement boundary is balanced by the energy supply from fusion reactions. This section is concerned with the mathematical formulation of this condition. As the ratio of neutron and α -particle masses is 1/4, the neutron of (1.1) carries 4/5 of the released energy. As neutrons are not charged, and thus unaffected by the magnetic field, they escape the plasma and collide with the wall containing the fusion device. These collisions produce the heat used for electricity creation. Surprising as it may seem, most fusion research is more concerned with the 3.5MeV alpha particles than the more energetic neutrons directly used for power production. Fusion plasma must be extremely hot for a sufficient amount of fusion reactions to occur, and thus inevitably lose heat to its colder surroundings. For ignition to occur this heat loss must be balanced by the heating delivered by the α -particles. The α -particle heat source is given by

$$\mathcal{E}_\alpha = E_\alpha n_D n_T \langle \sigma_{DT} v \rangle, \quad (1.3)$$

where σ_{DT} is the cross section of the reaction (1.1), v is the relative velocity of colliding deuterium and tritium ions, and the brackets $\langle \rangle$ denote an average over velocity space. The expression $\langle \sigma v \rangle$ is generally referred to as the rate of

the reaction with cross section σ . These concepts, as well as the derivation of expressions like (1.3) are thoroughly accounted for in chapter 2 and 3. The rate of deuterium-tritium fusion in a plasma with a Maxwellian velocity distribution is peaked at a temperature of 70keV ¹, [6]. (1.3) can be somewhat misconceiving as it seems that fusion power can be achieved by simply cranking up the plasma density. In reality, however, increasing the density leads to cooling of the plasma unless the energy density is equally increased. It is thus instructive to rewrite (1.3) in terms of the pressure, better reflecting the limitation of magnetically confined fusion devices

$$\mathcal{E}_\alpha = \frac{1}{16} p^2 \frac{\sigma_{DT}}{T^2}, \quad (1.4)$$

where the pressure $p = 2nT$, and n is the electron density. The ion species are assumed to have equal densities, and the plasma is assumed quasi-neutral such that $n_D = n_T = n/2$. The rate of heat loss in a fusion reactor is usually approximated by

$$\mathcal{E}_k = \frac{3}{2} \frac{p}{\tau_E}, \quad (1.5)$$

where τ_E represents the e-folding relaxation time of the plasma energy due to loss of heat to the surroundings, usually excluding the unavoidable Bremsstrahlung losses, [5],

$$\mathcal{E}_B = \frac{C_B}{4} \frac{p^2}{T^{3/2}}, \quad (1.6)$$

where $C_B = 5.35 \cdot 10^3$ is a numerical constant. At the usual production temperature and pressure of a fusion reactor, Bremsstrahlung losses are small compared to other heat losses, [5].

In actual fusion devices, the plasma is heated externally e.g. in a Tokamak² a toroidal current, necessary to create a poloidal magnetic field, gives rise to ohmic heating. External heating shall however be neglected in the current simple analysis of energy balance, thus describing the condition for what is referred to as ignition within fusion research. The requirement of ignition can be written

$$\mathcal{E}_\alpha = \mathcal{E}_B + \mathcal{E}_K. \quad (1.7)$$

¹In kinetic theory and fusion research it is customary to do the contraction $T k_B \rightarrow T$, where k_B is the Boltzmann constant. This convention is adopted in this work, with the immediate consequence that unless explicitly stated any temperature T in this thesis actually reads $k_B T$, and has units of energy.

²The Tokamak is introduced in the next section

Combining (1.4), (1.5), (1.6) and (1.7) yields the well known Lawson criterion, [5, 10],

$$p\tau_e \geq \frac{\frac{3}{2}p^2}{\frac{E_\alpha}{16}\langle\sigma_{DT}v\rangle - \frac{C_B}{4}T^{1/2}}. \quad (1.8)$$

The RHS of (1.8) has its minimum at around 15keV, indicating that this temperature sets the lowest demands for a fusion reactor in terms of the Lawson parameter $p\tau_E$. As briefly mentioned, true ignition expressed by the Lawson criterion is not obtainable in current devices as they are dependent on external heating to some extent. As a figure of merit for fusion reactors the Q-factor, defined as the ratio of output power to input power, is introduced. This is approximated by [5] as

$$Q = 5 \frac{p\tau_E}{(p\tau_E)_I - p\tau_E}, \quad (1.9)$$

where $(p\tau_E)_I$ is the Lawson parameter required for ignition. (1.9) shows, as expected, that the Q-factor diverges towards infinity when the Lawson parameter goes towards $(p\tau_E)_I$ corresponding to non-assisted steady-state fusion. (1.9) makes it clear that the goal of fusion research is to design fusion reactors with a Lawson parameter as close as possible to that required for ignition. This is attempted by the use of magnetic confinement devices. The most widespread of these is known as a Tokamak, which is described in the following section. In a later section, the effects influencing τ_E shall be discussed, as an understanding of these is clearly paramount in reactor design. For now, I will note that a more sophisticated analysis of the energy balance of a fusion reactor, including the temperature dependence of τ_E , reveals that it can be operated in a stable equilibrium, [5] i.e. an increase in temperature will give rise to a larger increase in heat loss than in fusion energy release, and vice versa. The result is that runaway power creation, known to cause meltdowns in fission reactors, does not pose a safety risk to fusion reactors.

1.2 The Tokamak

This section presents the confinement device known as a Tokamak. The general idea of magnetic confinement is introduced, and it is shown how the demand for stable equilibria naturally leads to the Tokamak.

In chapter 2, the momentum equation of a fluid is derived. At this point, I shall simply state, that in a simplified case where the fluid in question is

non-viscous, shows no explicit collisional effects³, and is subject to a force \mathbf{F} , the equation of motion can be written

$$mn \left(\frac{\partial}{\partial t} + \mathbf{u} \cdot \nabla \right) \mathbf{u} = -\nabla p + \mathbf{F}, \quad (1.10)$$

where \mathbf{u} is the fluid velocity. In modern fusion reactors such as ITER, the maximum pressure will be of the order of 10^6 Pa , [11], meaning that significant pressure gradients towards the center of the device are inevitable. In dealing with pressured gasses for everyday and industrial purposes the ∇p -term of (1.10) is usually counteracted by a solid container. This approach is futile in containing a fusion plasma with a temperature of $\sim 20 \text{ keV}$, as no material will withstand such temperatures. Instead, containment is achieved by utilizing the magnetic part of the Lorentz Force with the fact that plasma consists of charged particles. Inserting the Lorentz force, $nq(\mathbf{E} + \mathbf{u} \times \mathbf{B})$ where q is the charge of the plasma particles, into (1.10) and taking the cross product with the magnetic unit vector $\hat{\mathbf{b}}$ yields

$$\mathbf{u}_\perp = \frac{\mathbf{E} \times \hat{\mathbf{b}}}{B} + \frac{\hat{\mathbf{b}} \times \nabla p}{nqB} + \frac{m}{qB} \hat{\mathbf{b}} \times \left(\frac{\partial}{\partial t} + \mathbf{u} \cdot \nabla \right) \mathbf{u}, \quad (1.11)$$

The terms on the RHS are known as the $\mathbf{E} \times \mathbf{B}$ -drift, the diamagnetic drift, and the polarization drift, respectively. (1.11) reveals that in the simplified case of a homogeneous uniform magnetic field, the problematic ∇p -term has been reduced to a transverse diamagnetic current, advecting fluid along isobaric surfaces and thus causing no further trouble than partially canceling the external magnetic field⁴. This founding idea of magnetic confinement has, however, introduced less fortunate drift terms. The problematic $\mathbf{E} \times \mathbf{B}$ -drift causes bulk plasma motion across field lines. In the ideal MHD ordering where the $\mathbf{E} \times \mathbf{B}$ -drift causes the only field-perpendicular motion of the plasma, [5], multiple field geometries capable of producing an equilibrium exists. These set the starting point of any reactor magnetic confinement device.

The most simple equilibrium geometry is an infinite cylinder where a plasma can be held in equilibrium by what is referred to as a θ -pinch, since the current producing the magnetic field flows in the azimuthal direction. For a finite cylinder, the nonuniform magnetic field at the ends causes problems making the cylindrical field geometry intractable. In order to achieve

³As we shall see it is not sensible to consider a fluid without collisions, hence the notion of explicit collisional effects.

⁴In an inhomogeneous magnetic field the diamagnetic drift gives rise to a charge dependent drift causing stability issues, which shall be detailed later.

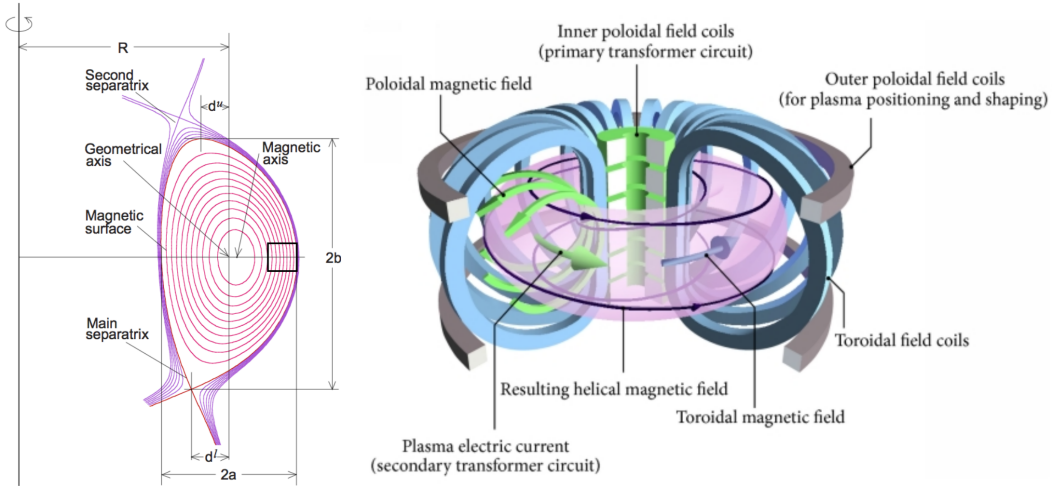


Figure 1.1: The left figure shows the detailed cross-sectional geometry of a Tokamak, where the **Outboard Midplane** (exaggerated in size) is marked by the **black box**. The right figure shows a schematic illustration of a Tokamak. The figures are available at [12] and [13] respectively.

equal properties over the full surface of the confined plasma Poincare's hairy ball theorem, [14] suggests that the geometry of the magnetic field should be toroidal. Bending a solenoid into a torus does, however, destroy the uniformity and homogeneity of the magnetic field. It can be shown, [5], that in toroidal geometry, the θ -pinch gives rise to no equilibria. A Poloidal component of the magnetic field, as shown by the green arrows of 1.1, is a necessity. The means of creating this poloidal field separates the Tokamak, from the other toroidal confinement device still being researched, the Stellarator, [15]. The Tokamak, which shall be discussed here, achieves the poloidal component of the magnetic field by inducing a toroidal current in the plasma, shown as the green arrow in the toroidal direction in figure 1.1. Unfortunately, even by combining toroidal and poloidal magnetic fields, it is not practically possible to produce a fusion plasma confined in static equilibrium. The inevitable motion of the plasma gives rise to heat transport which is the subject of the next section.

1.3 Anomalous Transport

As evident from (1.9) the energy confinement time, τ , is a key aspect of a fusion reactor. Calculating τ_E is however tremendously complicated and it is usually determined by empirical measurements, [16]. The total energy loss is partly constituted by the *classical* losses of energy loss due to diffusion and heat conduction. These losses can be calculated from the transport coefficients. Determining the transport coefficients is a complex task in itself, which is the very goal of kinetic theory. For two-fluid plasmas, approximations of these

coefficients were first presented by Braginskii in his celebrated article of 1965, [17]. Calculating the energy loss from diffusion and conduction by use of the transport coefficients shows that they only account partly for the total energy loss. The actual energy loss of a Tokamak is found to exceed that predicted by diffusion and conduction losses by a factor of order unity, [18–20]. This discrepancy is due to multi-scale turbulence on the plasma edge producing a net radial flux of particles and energy due to the advection [21]. The magnitude of the radial advective energy caused by turbulence depends on the specific device, but also on the specific setup and experiment. In 1982 a regime of high containment was discovered on the Tokamak ASDEX, [22]. This regime of high containment was characterized by a decrease in edge turbulence and heat transport making the reactor operate at an increased pressure with an improved energy confinement time, which according to the former discussion of energy balance is obviously very desirable. This operation mode is known as H-mode, while a reactor not operating in this desired mode is said to be in L-mode. The exact mechanisms of transport reduction in H-mode are still not completely uncovered. There is however substantial evidence that edge turbulence is decreased by a radially sheared poloidal flow at the plasma edge, thus limiting transport [23–25]. A subject raising further unanswered questions is the physics governing transitions between L-mode and H-mode, which remains one of the most actively researched areas in magnetically confined fusion programs across the world [26–29].

In this thesis, edge plasma at the outboard midplane⁵ is modeled using the HESEL model [30], a successor of the ESEL model [31]. Specifically, the influence of neutral gas on edge plasma dynamics is investigated. Before venturing into the subject of plasma-neutral interactions, the relevant mechanism for turbulence creation at the outboard midplane is introduced. This mechanism is known as interchange dynamics, leading to the ballooning instability, [32], and is the subject of the following section.

1.4 Interchange Dynamics

This section introduces the basic theory of interchange dynamics known to give rise to a wide range of collective plasma phenomena in plasma confinement experiments including global confinement loss, [33–36], and radial propagation of localized blobs across the LCFS (**L**ast **C**losed **F**lux **S**urface) and into the

⁵See figure 1.1

SOL (Scrape Off Layer) [37–40], the latter of which is the concern of this thesis. To understand the origin of interchange dynamics, consider the single fluid momentum equation for a quasi-neutral plasma in a magnetic field \mathbf{B} , [41],

$$\left(\frac{\partial}{\partial t} + \mathbf{u} \cdot \nabla \right) \mathbf{u} + \nabla \cdot \bar{\boldsymbol{\pi}} = -\nabla p + \mathbf{J} \times \mathbf{B}, \quad (1.12)$$

where \mathbf{u} is the fluid velocity, p is the scalar pressure, $\bar{\boldsymbol{\pi}}$ is the viscous stress tensor and \mathbf{J} is the current density⁶. In static equilibrium, the LHS of (1.12) vanishes leaving

$$\nabla p = \mathbf{J} \times \mathbf{B}. \quad (1.13)$$

By Amperes law the current density can be written $\mu_0 \mathbf{J} = \nabla \times \mathbf{B}$, which lets one express the Lorentz force term of (1.12)

$$\mathbf{J} \times \mathbf{B} = \frac{B^2}{\mu_0} (-\nabla_{\perp} \ln B + \boldsymbol{\kappa}), \quad (1.14)$$

thus defining the magnetic curvature vector $\boldsymbol{\kappa} = (\hat{\mathbf{b}} \cdot \nabla) \hat{\mathbf{b}}$ where $\hat{\mathbf{b}}$ is the field aligned unit vector. This leads to the definition $\nabla_{\perp} = \nabla - \hat{\mathbf{b}}(\hat{\mathbf{b}} \cdot \nabla)$. Furthermore, the standard notation $\nabla \ln s = \frac{\nabla s}{s}$, where s is an arbitrary scalar field, is applied. (1.13) and (1.14) imply that in equilibrium, a confined plasma with a magnetic pressure, B^2/μ_0 , that is large compared to the plasma pressure, p , is subject to the condition

$$\nabla_{\perp} \ln B \approx \boldsymbol{\kappa}. \quad (1.15)$$

This approximation amounts to neglecting the cancellation of the magnetic field by the diamagnetic current. Denoting $(\frac{\partial}{\partial t} \mathbf{u} + \nabla \cdot \mathbf{u}) \mathbf{u} + \nabla \cdot \bar{\boldsymbol{\pi}}$ by \mathbf{f} , taking the curl of (1.12) and manipulating the resulting equation using (1.14) one can derive the expression, [42],

$$\mathbf{B} \cdot (\nabla \times \mathbf{f} - 2\boldsymbol{\kappa} \times \mathbf{f}) = B^2 \mathbf{B} \cdot \nabla \left(\frac{J_{\parallel}}{B} \right) + 2\mathbf{B} \cdot \boldsymbol{\kappa} \times \nabla p, \quad (1.16)$$

known as the Shear-Alfvén law. (1.16) is often referred to as the vorticity equation as the LHS, describing the plasma response to the forces on the RHS, is primarily constituted by the vorticity of the $\mathbf{E} \times \mathbf{B}$ -drift, which dominates plasma advection in most conditions relevant to magnetically confined plasma. The first term on the RHS of (1.16) describes vorticity creation due to parallel currents. This work focuses on turbulence creation due to perpendicular dynamics, and so only the second term shall be discussed here.

⁶See appendix A for a definition of these quantities

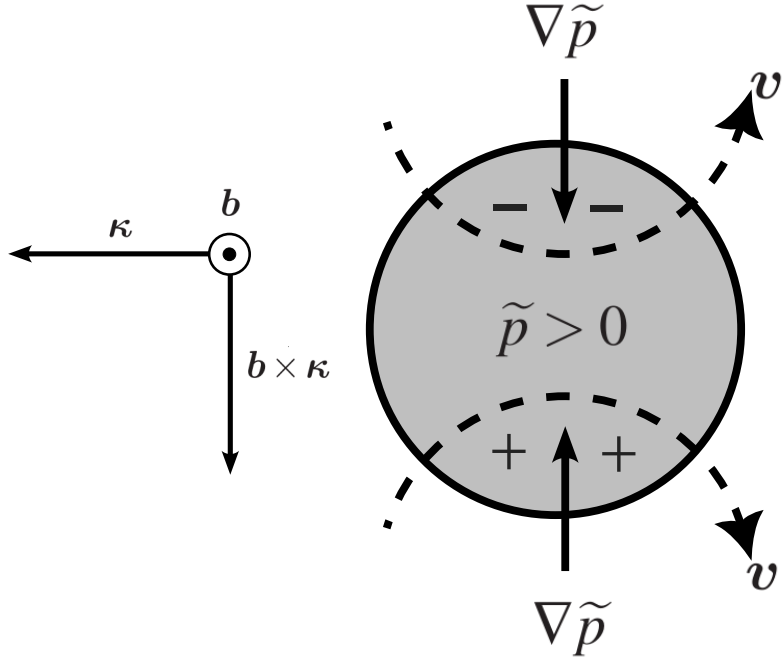


Figure 1.2: Pressure gradient driven instability of a plasma in a nonuniform magnetic field. This figure was originally printed in [41], and is reprinted here by courtesy of Odd Erik Garcia.

Figure 1.2 serves to illustrate how the second term of (1.16) can lead to instability. The grey part of the image shows a small section of magnetized plasma. This plasma is subject to a perturbation, making the pressure in this region larger than the neighboring regions along the vertical axis of the figure. When pressure gradients have components perpendicular to κ , the last term of (1.16) dictates that plasma must exhibit vorticity characterized by a curl of velocity oriented along the magnetic axis. This vorticity is indicated in figure 1.2 by the curved velocity arrows, causing advection in a direction anti-parallel to κ . If the plasma advected into the grey area is characterized by a larger pressure than the fluid leaving it, the initial pressure perturbation is increased and the process is self-enhancing i.e. unstable. Denoting the equilibrium pressure by p_{eq} , we thus conclude, that if κ and ∇p_{eq} have parallel components i.e. $\kappa \cdot \nabla p_{eq} > 0$, the plasma perturbation in figure 1.2 is unstable while the opposite is true if $\kappa \cdot \nabla p_{eq} < 0$. To understand the underlying mechanism leading to the advective interchange motions, we shall step into the particle picture. It is well known that ∇B and curvature drifts give rise to charge dependent guiding center drifts perpendicular to the magnetic field. The current arising from these drifts is given by, [41],

$$\mathbf{J}_B = \frac{p}{B} \left(\hat{\mathbf{b}} \times \nabla \ln B + \hat{\mathbf{b}} \times \kappa \right). \quad (1.17)$$

As indicated by (1.15) both terms contribute equally to \mathbf{J}_B . The drifts cause

positive charges to move vertically downwards in figure 1.2 while negative charges move up as indicated. This charge separation creates an electric field causing particles to $\mathbf{E} \times \mathbf{B}$ -drift in a direction anti-parallel to κ .

The analysis of interchange motion given above reveals three characteristics of interchange dynamics important to the current work. Firstly, turbulence creation through interchange dynamics is driven by the equilibrium pressure gradient, which can be affected in gas puffing experiments. Secondly, the orientation of the curvature vector relative to the equilibrium pressure gradient determines the stability of interchange dynamics, resulting in the outer edge of a Tokamak being unstable to these dynamics while the inside is stable. The outside is said to exhibit unfavorable curvature while the curvature on the inside is favorable. More specifically $\kappa \cdot \nabla p_{eq}$ is maximized at the outboard midplane, making this region most susceptible to interchange instability. A consequence is that the radial advection due to interchange motions is poloidally asymmetric i.e. it is maximized at the outboard midplane and decreases in the positive and negative poloidal directions. Thirdly the considerations in terms of particle motion have revealed that ∇B and curvature drifts in conjunction with the $\mathbf{E} \times \mathbf{B}$ -drift explain the mechanism behind interchange dynamics. Given this mechanism, it is clear that no equilibria exist for a plasma in a purely toroidal magnetic field. This problem can however be solved by adding a poloidal field component. To understand the stabilizing effect of a poloidal field component, consider a positively charged particle in the lower half of a Tokamak. The ∇B and curvature drift will make this particle drift across magnetic field lines with a velocity whose radial component is positive. The opposite will be true if the same particle is in the upper half of the Tokamak. Adding a poloidal component to the magnetic field will thus help to cancel the effect of ∇B and curvature drifts as a charged particle moves along magnetic field lines. In the vicinity of the LCFS the poloidal component of the magnetic field is relatively small compared to the toroidal component suppressing the cancellation of the polarization current causing the interchange instability. Outside the LCFS the magnetic field lines do not close on themselves but interfere with divertors, completely diminishing the stabilization of interchange dynamics. At the outboard midplane where the interchange instability is most significant this gives rise to large blobs of plasma escaping into the SOL, a phenomenon known as ballooning.

1.5 Neutrals and Plasmas

Several internal sources of neutral particles exist in a fusion reactor. Outside the LCFS temperatures can be sufficiently low for neutral atoms to be created by recombination. More importantly, turbulent transport advects plasma radially across the LCFS. The majority of this unconfined plasma will move along the magnetic field lines until impacting on a divertor where recycling creates neutral particles. The neutral source due to recombination is generally small compared to that of divertor recycling implying that the neutral densities of these naturally occurring sources are largest in the divertor regions ⁷, and thus expected to be small at the outboard midplane. The focus of this thesis is thus neutrals supplied from external sources, which is common for fueling and imaging purposes.

The plasma of a fusion reactor in production is gradually contaminated by helium from fusion processes and impurities entering from plasma-wall interactions. To accomplish steady-state fusion the plasma must be able to exhaust these impurities, and new fuel has to be supplied. Fueling can be achieved by multiple methods, the simplest of which is gas puffing, where cold gas is injected into the reactor chamber and ionized by the plasma. For fueling to be successful, ionization has to take place within the LCFS. One of the applications of the current work is to analyze the ability of gas puffing to supply the confined plasma with new fuel. To ensure the required penetration depth the alternative methods of *super-sonic molecular beam injection*, [43], and *high speed frozen fuel pellets*, [44], have been designed.

Neutrals can also be added to the plasma for diagnostic purposes. The image contrast is created from the excitement and decay of neutrals causing emission of radiation [45]. Furthermore, high energy neutral beams are used as a common method for plasma heating. The use of this method gave rise to the first discovery of H-mode [22, 46]. Finally, neutral gas can be used to cool the plasma outside the LCFS to protect the material surfaces. The neutral model presented in this work is, in principle, capable of simulating all of these phenomena.

From the brief revision on anomalous transport given above it is clear that an understanding of turbulent transport at the plasma edge is of great importance in designing future fusion reactors. The focus of this thesis is to investigate how the injection of neutral gas at the outboard midplane affects edge dynamics, along with the ability of the neutral particles to penetrate

⁷The ends of the red line on the left of figure 1.1.

beyond the last closed flux surface, thus fueling the plasma. These efforts are motivated by experimental findings, [47], suggesting that gas puffing with molecular deuterium reduces the pressure gradient in the edge region, which could affect the radial flux due to advection caused by interchange dynamics. Furthermore, gas puffing is believed to be able to cause a transition from H-mode to L-mode [48–50], an event that must be avoided when fueling modern reactors.

1.6 Modeling Neutrals

Modeling of neutrals has been part of fusion research for decades and has been approached with fluid as well as kinetic models. Several applications coupling fluid models to edge turbulence models have already been published e.g. the coupling of a 2D fluid neutral model with HESEL, [51, 52], which is closely related to this work. However, due to the long mean free path of neutrals in the plasma edge region, [53], a fluid description of neutrals is not strictly valid. For this reason, most neutral models are based on kinetic approaches. These often seek to solve the Boltzmann equation⁸ by Monte Carlo methods. A well-known result of such an approach is the EIRENE model [54]. Originally the neutral models were used to model the behavior of neutrals, without letting the neutrals influence the plasma dynamics. Later on, they were self-consistently coupled to plasma dynamics as in [55]. Attempts to couple EIRENE and similar kinetic neutral codes to plasma edge turbulence codes have been found to lead to excessive computational costs, [56]. In the last decade, however, several successful attempts in coupling kinetic neutral codes with plasma edge turbulence codes have been published [57–60]. A common characteristic of these is that they, unlike the present work, only include a single mono-atomic neutral species.

As an alternative kinetic method for neutral modeling, this work uses a DSMC(Direct Simulation Monte Carlo)-like simulation scheme [61]. In DSMC models a system of physical particles is modeled by a statistically representative⁹ number of super-particles, each representing a large number of physical particles. In each time step, the particle motions are calculated deterministically, while the collisions are treated statistically. The current model deviates from usual DSMC calculations as it neglects elastic collisions

⁸To be introduced in chapter 2 and chapter 3.

⁹The understanding of representative in the current context is detailed in chapter 7.

between neutrals. This might seem strange but is not uncommon even in highly sophisticated modeling of neutrals in edge plasma [60]. The result of neglecting collisions between neutrals is that the problem can be expressed as embarrassingly parallel i.e. it can be divided into arbitrarily many sub-tasks without the need to communicate and without loss of generality. This fact alone makes DSMC a highly interesting alternative to the usual kinetic methods whose parallelism is limited by the grid dimensions and relies on extensive communication between the subdomains. Another advantage of DSCM is its close analogy with our perception of the physical system it describes, as a neutral gas is a large number of particles moving in straight lines between collisions characterized by a small spatial and temporal extent. This direct coupling makes the implementation of complicated chemical reactions and interpretation of the produced results easier and more intuitive than is the case for comparable Monte Carlo solvers. As the model presented in this thesis tracks super-atoms and -molecules that only interact with the plasma and not with each other, it shall be named PISAM (**P**lasma **I**nteracting **S**uper **A**toms and **M**olecules).

2 Plasma Fluid Theory

This chapter introduces the Boltzmann equation and derives the transport equations of the defining properties of a plasma subject to electric and magnetic fields, including elastic as well as inelastic collisions. This chapter thus presents the first step in the derivation of the nHESEL equations. The reader that is not well acquainted with the notion of the phase space distribution function, f , and the definitions of density, n , fluid velocity, \mathbf{u} , temperature T , scalar pressure, p and the viscous stress tensor $\bar{\pi}$, in the context of kinetic theory should consult appendix A. In the following the velocity of a particle in a common reference frame, S , is denoted \mathbf{v} while the random velocity shall be defined $\mathbf{w} = \mathbf{v} - \mathbf{u}$, where \mathbf{u} is also expressed with respect to S .

2.1 The Boltzmann Equation

The development of the phase space distribution function is given through phase space conservation as expressed by Louville's theorem, [62],

$$\frac{\partial \tilde{f}}{\partial t} + \mathbf{v} \cdot \nabla \tilde{f} + \tilde{\mathbf{a}} \cdot \nabla_{\mathbf{v}} \tilde{f} = \frac{\partial \tilde{f}}{\partial t} + \mathbf{v} \cdot \nabla \tilde{f} + \frac{\tilde{\mathbf{F}}}{m} \cdot \nabla_{\mathbf{v}} \tilde{f} = 0. \quad (2.1)$$

Where \tilde{f} denotes the microscopic phase space distribution function, and $\tilde{\mathbf{a}}$ denotes accelerations on all length scales, including those of collisions. The apparent simplicity of (2.1) is misleading due to the fact that it describes the evolution of the microscopic phase space distribution which is essentially a sum of Dirac delta functions [63]. Furthermore, the magnetic and electric fields going into the force term, if (2.1) is applied to describe a plasma, will be spiky as it includes the rapidly fluctuating micro fields that arise when charged particles come very close to each other [17]. Solving (2.1) thus amounts to solving the electromagnetic many-body problem, a completely hopeless task. Instead \tilde{f} shall be replaced by f which represents a smoothed density function over a volume containing a large number of particles. Likewise, $\tilde{\mathbf{F}}$ shall be replaced by the macroscopic force \mathbf{F} representing the force averaged over a large number of particles and thus not including the rapidly fluctuating forces

arising due to collisions between these particles. To account for any processes with spatial and temporal scales too short to be resolved by f and \mathbf{F} a collision operator \mathcal{C} is introduced, yielding what is known as the Boltzmann equation

$$\frac{\partial f}{\partial t} + \mathbf{v} \cdot \nabla f + \frac{\mathbf{F}}{m} \cdot \nabla_v f = \mathcal{C} = \mathcal{E} + \mathcal{I}, \quad (2.2)$$

where the last equality indicates a division of the collision operator into contributions from elastic and inelastic collisions respectively. The following chapter is devoted to the theory of binary collisions and will introduce the collision operators in detail. For now, note that the collision operator includes collisions with all species in the fluid, including the species itself.

2.2 Transport equations

Multiplying the Boltzmann equation, (2.2), by a physical quantity ϕ and integrating over velocity space, one can derive the spatial transport equation for the macroscopic quantity $\langle \phi \rangle$, where $\langle \cdot \rangle$ denotes an average over velocity space. Rather than deriving a transport equation for the most general case $\phi = \phi(\mathbf{r}, \mathbf{v}, t)$, we shall simplify the task by assuming that $\phi = \phi(\mathbf{v})$ i.e. it is a function of velocity only. The reason for such a simplification is that the macroscopic variables in which we want to express our fluid equations, n , \mathbf{u} , and T^{10} are all moments of velocity. By the use of (A.3), and utilizing that since integrating runs over the full velocity space the integration limits are independent of t and \mathbf{r} , the first two terms of the transport equation become

$$\int \phi \frac{\partial f}{\partial t} d\mathbf{v} = \frac{\partial n \langle \phi \rangle}{\partial t} \quad \text{and} \quad \int \phi v_i \frac{\partial f}{\partial r_i} d\mathbf{v} = \frac{\partial n \langle v_i \phi \rangle}{\partial r_i} \quad (2.3)$$

where Einstein notation for dummy indices has been employed in the latter, which will be assumed for the rest of this thesis. To rewrite the third term, it is assumed that f falls off rapidly with $|\mathbf{v}| \rightarrow \infty$, which is certainly the case for a Maxwellian distribution. Moreover, assume that \mathbf{F} is divergence-free in velocity space i.e. $\nabla_v \cdot \mathbf{F} = 0$, which is notably true for the Lorentz force, and obviously true for any force not depending on velocity. The third term is now readily evaluated:

¹⁰These will simply be referred to as *the macroscopic variables*.

$$\begin{aligned}
\frac{1}{m} \int \phi \mathbf{F} \cdot \nabla_v f d\mathbf{v} &= \frac{1}{m} \int \nabla_v \cdot (\phi f \mathbf{F}) d\mathbf{v} - \frac{1}{m} \int f \nabla_v \phi \cdot \mathbf{F} d\mathbf{v} \\
&\quad - \frac{1}{m} \int \phi f \nabla_v \cdot \mathbf{F} d\mathbf{v} \\
&= \frac{1}{m} \oint \phi f \mathbf{F} \cdot d\mathbf{s} - \frac{n}{m} \langle F_i \frac{\partial \phi}{\partial v_i} \rangle = -\frac{n}{m} \langle F_i \frac{\partial \phi}{\partial v_i} \rangle.
\end{aligned} \tag{2.4}$$

The collisional terms shall be denoted

$$\int \phi (\mathcal{E} + \mathcal{I}) d\mathbf{v} = E^{(\phi)} + I^{(\phi)}, \tag{2.5}$$

and the transport equation for $\phi = \phi(\mathbf{v})$ can thus be written

$$\frac{\partial n \langle \phi \rangle}{\partial t} + \frac{\partial n \langle v_i \phi \rangle}{\partial r_i} - \frac{n}{m} \langle F_i \frac{\partial \phi}{\partial v_i} \rangle = E^{(\phi)} + I^{(\phi)}. \tag{2.6}$$

The fluid equations are now obtained by setting ϕ equal to 1, $m\mathbf{v}$ and $\frac{1}{2}mv^2$ respectively. It is worth noting from (2.6), that the time evolution of $n\langle \phi \rangle$ depends on the higher order velocity moment through $\langle v_i \phi \rangle$, such that no closed set of equations can be formed from (2.6) without further approximation. This generally indicates that the fluid description is somewhat too reductionistic to express the dynamics of fluid systems such as liquids, gases, and plasmas, in accordance with the Boltzmann equation.

Moments of velocity

We shall now derive the transport equations for the relevant moments of velocity, corresponding to the summational invariants of elastic collisions. For clarity the species subscript, s shall be introduced, and the meaning of the collisional contributions shall be specified through

$$E_s^{(\phi)} = \sum_{s'} E_{ss'}^{(\phi)} \quad \text{and} \quad I_s^{(\phi)} = \sum_{s'} I_{ss'}^{(\phi)} \tag{2.7}$$

The Continuity Equation

Setting $\phi = 1$ in (2.6) yields

$$\frac{\partial n_s}{\partial t} + \frac{\partial n_s u_{i,s}}{\partial r_i} = \frac{\partial n_s}{\partial t} + u_{i,s} \frac{\partial n_s}{\partial r_i} + n \frac{\partial u_{i,s}}{\partial r_i} = I_s^{(1)}. \tag{2.8}$$

where it has been utilized that elastic collisions do not contribute to the continuity equation due to particle conservation. (2.8) can be written equivalently

in vector form as

$$\frac{\partial n_s}{\partial t} + \nabla \cdot (n_s \mathbf{u}_s) = \left(\frac{\partial}{\partial t} + \mathbf{u}_s \cdot \nabla \right) n_s + n_s \nabla \cdot \mathbf{u}_s = \frac{d_s n}{dt} + n_s \nabla \cdot \mathbf{u}_s = I_s^{(1)}, \quad (2.9)$$

where the advective derivative $\frac{d_s}{dt} = \left(\frac{\partial}{\partial t} + \mathbf{u}_s \cdot \nabla \right)$ has been introduced. Index notation and vector notation shall be used interchangeably depending on the context.

The Momentum Equation

Inserting $\phi = m\mathbf{v}$ in (2.6) and considering only the i'th component of the resulting equation yields

$$m_s \frac{\partial n u_{i,s}}{\partial t} + m_s \frac{\partial n_s \langle v_j v_i \rangle_s}{\partial r_j} - n \langle F_j \frac{\partial v_i}{\partial v_j} \rangle_s = E_{i,s}^{(mv)} + I_{i,s}^{(mv)}. \quad (2.10)$$

Now impose

$$\langle v_j v_i \rangle_s = u_{i,s} u_{j,s} + \langle w_i w_j \rangle_s = u_{i,s} u_{j,s} + \frac{\bar{\bar{\mathbf{p}}}_{ij,s}}{m_s n_s} \quad \text{and} \quad \frac{\partial v_i}{\partial v_j} = \delta_{ij}, \quad (2.11)$$

where $\bar{\bar{\mathbf{p}}}$ denotes the pressure tensor and it was used that $\langle w_i \rangle = 0$ per definition, to obtain

$$\begin{aligned} & m_s n_s \frac{\partial u_{i,s}}{\partial t} + m_s u_{i,s} \frac{\partial n_s}{\partial t} + m_s u_{j,s} u_{i,s} \frac{\partial n_s}{\partial r_j} + m_s n_s u_{i,s} \frac{\partial u_{j,s}}{\partial r_j} \\ & + m_s n_s u_{j,s} \frac{\partial u_{i,s}}{\partial r_j} + \frac{\partial \bar{\bar{\mathbf{p}}}_{ij,s}}{\partial r_j} - n_s \langle F_i \rangle_s = E_{i,s}^{(mv)} + I_{i,s}^{(mv)}. \end{aligned} \quad (2.12)$$

Multiplying the continuity equation, (2.8) by $u_{i,s} m_s$ and subtracting it from (2.12) gives the i'th component of the momentum equation in its usual form

$$m_s n_s \left(\frac{\partial}{\partial t} + u_{j,s} \frac{\partial}{\partial r_j} \right) u_{i,s} + \frac{\partial \bar{\bar{\mathbf{p}}}_{ij,s}}{\partial r_j} - n_s \langle F_i \rangle_s = E_{i,s}^{(mv_i)} + I_{i,s}^{(mv_i)} - m u_{i,s} I_s^{(1)}. \quad (2.13)$$

Finally inserting the Lorentz force and employing the definition of the pressure tensor given in (A.10) the vector form of the momentum equation can be written

$$m_s n_s \frac{d_s \mathbf{u}_s}{dt} + \nabla p_s + \nabla \cdot \bar{\bar{\mathbf{p}}}_s - n_s q_s (\mathbf{E} + \mathbf{u}_s \times \mathbf{B}) = \mathbf{E}_s^{(mv)} + \mathbf{I}_s^{(mv)} - m_s \mathbf{u}_s I_s^{(1)}. \quad (2.14)$$

E_s^{mv} denotes the friction force exerted on species s by elastic collisions with other species. Note that collisions with species s itself do contribute to this term due to momentum conservation in elastic collisions i.e. $E_{ss}^{mv} = 0$, meaning that single species fluid equations only considering elastic collisions become

particularly simple, due to the fact that the fluid equations are expressed in terms of summational invariants of elastic collisions. I_s^{mv} is the rate of change of momentum density due to inelastic collisions, and $m_s \mathbf{u}_s I_s^{(1)}$, coming from the continuity equation, accounts for the fact that the mean velocity is dependent on the number density through $1/n_s$. To emphasize this point consider the following decomposition of $\frac{d_s \mathbf{u}_s}{dt}$

$$\begin{aligned} m_s n_s \frac{d_s \mathbf{u}_s}{dt} &= m_s n_s \frac{d_s}{dt} \frac{1}{n_s} \int \mathbf{v} f_s d\mathbf{v} \\ &= m_s \frac{d_s}{dt} \left(\int \mathbf{v} f_s d\mathbf{v} \right) + m_s n_s \frac{-1}{n_s^2} \frac{d_s n_s}{dt} \int \mathbf{v} f_s d\mathbf{v} \quad (2.15) \\ &= \frac{d_s n_s m_s \mathbf{u}_s}{dt} - m_s \mathbf{u}_s \frac{d_s n_s}{dt} \end{aligned}$$

The change in momentum density due to inelastic collisions is given by $I_s^{(mv)}$ while the change in particle density due to inelastic collision is given by $I_s^{(1)}$. Inserting these into the far right hand side of (2.15) for $\frac{d_s n_s m_s \mathbf{u}_s}{dt}$ and $\frac{d_s n_s}{dt}$ respectively, reproduces the last two terms of (2.14). From these terms, one might also notice that, as expected, adding particles moving with fluid velocity does not change the fluid velocity.

The Energy Equation

Setting $\phi = \frac{1}{2} m_s v^2$ in (2.6) one finds

$$\frac{1}{2} m_s \frac{\partial n_s \langle v^2 \rangle_s}{\partial t} + \frac{1}{2} m_s \frac{\partial n_s \langle v_i v^2 \rangle_s}{\partial r_i} - \frac{n_s}{2} \langle F_i \frac{\partial v^2}{\partial v_i} \rangle_s = E^{(\frac{1}{2} m v^2)} + I^{(\frac{1}{2} m v^2)}. \quad (2.16)$$

The relevant expectation values are readily evaluated using that $\langle w_i \rangle = 0$, and the definitions (A.9) and (A.5):

$$\begin{aligned} \langle v^2 \rangle_s &= u_s^2 + \frac{3p_s}{m_s n_s} \\ \langle v_i v^2 \rangle_s &= \langle (u_{i,s} + w_i)(u_s^2 + w^2 + 2u_{j,s}w_j) \rangle_s \quad (2.17) \\ &= u_{i,s} u_s^2 + u_{i,s} \frac{3p_s}{m_s n_s} + \frac{2q_{i,s}}{m_s n_s} + 2u_{j,s} \frac{\bar{\mathbf{p}}_{ij,s}}{m_s n_s} \end{aligned}$$

where the heat flux vector \mathbf{q} is given by

$$\mathbf{q} = \frac{1}{2} m n \langle w_i w^2 \rangle, \quad (2.18)$$

such that the rate of flow of thermal energy across a unit area of a surface which moves with fluid velocity $\mathbf{u} = \mathbf{v} - \mathbf{w}$, and has normal unit vector $\hat{\mathbf{n}}$ is

given as $\hat{\mathbf{n}} \cdot \mathbf{q}$. Inserting the expression of (2.17) and (2.18) in (2.16) yields the energy equation of species s

$$\begin{aligned} \frac{\partial}{\partial t} \left(\frac{1}{2} m_s n_s u_s^2 + \frac{3}{2} p_s \right) + \frac{\partial}{\partial r_i} \left(\frac{1}{2} m_s n_s u_{i,s} u_s^2 + \frac{3}{2} u_{i,s} p_s + q_{i,s} + u_{j,s} \bar{\mathbf{p}}_{ij,s} \right) \\ = n_s \langle F_i v_i \rangle_s + E_s^{(\frac{1}{2}mv^2)} + I_s^{(\frac{1}{2}mv^2)}. \end{aligned} \quad (2.19)$$

It is practical to write an equation expressing only the change of thermal energy, rather than the change of total energy. Furthermore, we will express this change through the advective derivative as is the case for the other fluid equations. This is achieved by multiplying the continuity equation (2.8) by $\frac{1}{2} m_s u_s^2$, taking the dot product of the momentum equation (2.14) with \mathbf{u}_s , which amounts to multiplying (2.13) by u_i , and subtracting the two resulting equations from the energy equation, (2.19). Moreover, the Lorentz force is inserted, such that the force term simplifies to $n_s \langle v_i F_i \rangle_s = q_s n_s u_{i,s} E_i$. After a bit of tensor algebra one finds

$$\begin{aligned} \left(\frac{\partial}{\partial t} + u_{i,s} \frac{\partial}{\partial r_i} \right) \frac{3}{2} p_s + \frac{5}{2} p_s \frac{\partial u_{i,s}}{\partial r_i} + \bar{\pi}_{ij,s} \frac{\partial u_{j,s}}{\partial r_i} + \frac{\partial q_{i,s}}{\partial r_i} \\ = E_s^{(\frac{1}{2}mv^2)} + I_s^{(\frac{1}{2}mv^2)} - u_{i,s} E_{i,s}^{(mv)} - u_{i,s} I_{i,s}^{(mv)} + \frac{1}{2} m_s u_s^2 I_s^{(1)}, \end{aligned} \quad (2.20)$$

which is equivalently written in vector notation as

$$\begin{aligned} \frac{3}{2} \frac{d_s p_s}{dt} + \frac{5}{2} p_s \nabla \cdot \mathbf{u}_s + \bar{\pi}_s : \nabla \mathbf{u}_s + \nabla \cdot \mathbf{q}_s \\ = E_s^{(\frac{1}{2}mv^2)} - \mathbf{u}_s \cdot \mathbf{E}_s^{(mv)} + I_s^{(\frac{1}{2}mv^2)} - \mathbf{u}_s \cdot \mathbf{I}_s^{(mv)} + \frac{1}{2} m_s u_s^2 I_s^{(1)}. \end{aligned} \quad (2.21)$$

Note how energy conservation is ensured through subtraction of the energy change due to the change in fluid velocity, \mathbf{u}_s . The implication is, that adding a particle with velocity \mathbf{v} to a species, s such that \mathbf{v} has an anti-parallel component to \mathbf{u}_s will result in a transfer from macroscopic translational energy to heat. It is also worth noting from the last three terms of (2.21), that adding particles moving with fluid velocity does not alter the pressure. This is expected since pressure depends on the random velocity, which is per definition zero for a particle moving with the fluid velocity. So far the collision operators have only been introduced as abstract mathematical entities. The following chapter quantifies these operators.

3 Collision Theory

To advance from the transport equations derived in the previous chapter to a self-consistent fluid model applicable in the description of edge turbulence in toroidal magnetized plasmas, an understanding of the effect of binary collisions in fluids is needed. Furthermore, the PISAM model relies heavily on collision theory to calculate the rate of plasma-neutral reactions. This chapter is devoted to first principle derivations presenting formulas, geometries, and assumptions specific to PISAM as well as the presentation of the Boltzmann collision operator and its effect on fluid equilibria. The latter is a vital part of the fluid closure presented in the following chapter. T

This chapter is structured such that the mathematically simplest collisions between neutral particles and electrons are presented first, after which the assumptions are gradually relaxed, toward the description of collisions between particles of species modeled as fluids.

3.1 Collision Rate of a Single Particle Interacting with a Fluid

Let p be a particle of species 1 moving towards a target with relative velocity \mathbf{g} . The target occupies an area, A , in the plane normal to \mathbf{g} and has thickness dx . The Target consists of particles of species 2 with density n . Let the cross section σ_{12} be defined such that the probability, P , for particle p to undergo a collision as it moves through the target, is given as the ratio of the sum of the cross sections in the target with the total size of the target, such that

$$P = \frac{An\sigma_{12}(g)dx}{A} = n\sigma_{12}(g)dx. \quad (3.1)$$

We now proceed to derive the expression for the reaction rate of a particle moving through space occupied by species 2, distributed with respect to the phase space distribution function $f_2(\mathbf{r}, \mathbf{v}, t)$.

Consider the particle p moving with velocity \mathbf{v}_1 with respect to some inertial frame S . Let the phase space distribution function of species 2 be defined with

respect to the same frame S . Consider collisions of p with particles of species 2 moving with velocity \mathbf{v}_2 , such that $\mathbf{g}_{12} = \mathbf{v}_1 - \mathbf{v}_2$. Let a cylinder, C, be defined by the cross sectional area $\sigma_{12}(g)$ and height $|\mathbf{g}_{12}dt| = gdt$, such that it has volume $V_C = \sigma_{12}gdt$. Following Chapman and Cowling [64] a collision between the particle p and a particle of species 2 of the specific type where the former has velocity \mathbf{v}_1 and the latter has a velocity within the range $d\mathbf{v}_2$ of \mathbf{v}_2 ¹¹ will occur within the short time span t, dt if the cylinder, C, is occupied by a particle of species 2 with $\mathbf{v}_2, d\mathbf{v}_2$ at time t. We shall neglect the probability that any such cylinder is occupied by multiple particles of species 2, such that only binary collisions are considered. According to the definition of the phase space given in appendix A the probability of the specified occupation of C is

$$P_C(\mathbf{r}, \mathbf{v}_1, \mathbf{v}_2, t) = V_C f_2(\mathbf{r}, \mathbf{v}_2, t) d\mathbf{v}_2 = \sigma_{12}(g) g f_2(\mathbf{r}, \mathbf{v}_2, t) d\mathbf{v}_2 dt. \quad (3.2)$$

Dividing by dt and integrating over all velocities \mathbf{v}_2 yields

$$\Gamma_{12}(\mathbf{r}, \mathbf{v}_1, t) = \int \sigma_{12}(g) g f_2(\mathbf{r}, \mathbf{v}_2, t) d\mathbf{v}_2 = n_2 \langle \sigma_{12} g \rangle_2, \quad (3.3)$$

which is the number of collisions per unit time, for a collision with cross section σ_{12} , between a particle p with velocity \mathbf{v}_1 and a species 2 distributed by f_2 at position \mathbf{r} at time t . Γ shall be referred to as the collision frequency while $\langle \sigma g \rangle$ shall be referred to as the collision rate or reaction rate. In consistency with the drift ordering presented in chapter 4 it shall be assumed that the thermal velocity of the plasma particles is significantly larger than the fluid velocity such that $\mathbf{v}_2 = \mathbf{u}_2 + \mathbf{w}_2 \approx \mathbf{w}_2$. In accordance with the Chapman Enskog closure scheme, it is further assumed that the phase space distribution function of the plasma species is approximately Maxwellian. The justification of this assumption is rigorously accounted for in the current and the following chapter.

Electron-Neutral Collisions

In PISAM a certain set of plasma-neutral interactions are considered. This set is presented in chapter 5. The collisions of this set can be divided into two subcategories of electron-neutral and ion-neutral collisions. At the relevant conditions, neutral energies are less than or similar to electron energies making the velocity ratio in electron-neutral collisions $r_v \gtrsim \sqrt{m_i/m_e} \gtrsim 60$. In these collisions, it is thus assumed that the relative velocity is equal to the electron

¹¹For brevity particles of species s that has a velocity within the range $d\mathbf{v}_s$ of \mathbf{v}_s , will simply be termed "A particle of species s with $\mathbf{v}_s, d\mathbf{v}_s$ ".

velocity, i.e. $v_{rel} \approx w_e$. With these assumptions, the collision frequency of (3.3) can be written

$$\Gamma_{ne}(\mathbf{r}, t) = n_e \langle \sigma w_e \rangle = n_e \sqrt{\frac{2}{\pi}} \left(\frac{m_e}{T_e} \right)^{3/2} \int \exp\left(-\frac{m_e w_e^2}{2T_e}\right) \sigma(w_e) w_e^3 dw_e, \quad (3.4)$$

where the Maxwell Boltzmann distribution has been inserted, and the symmetry of the integrand, provided by the assumption $g \approx w_e$, has been utilized in the integration over the solid angle. The spherical symmetry of (3.4) means that no net transfer of momentum between electrons and neutrals occurs when averaging over many electron-neutral collisions, meaning that all energy exchanged between electrons and neutrals is in the form of heat. This symmetry vastly simplifies the task of making a momentum- and energy-conserving coupling of PISAM with a plasma fluid model.

Ion-Neutral Collisions

In ion-neutral collisions, the particles going into the collisions have comparable mass. Furthermore, if a neutral particle is a product of a charge exchange reaction it will have an energy similar to the ion energies, and thus ions and neutrals will have similar velocities. In addition, the fluid velocity of ions can be within an order of magnitude from that of the neutral velocity and cannot be neglected as done in the former section. In conclusion, the spherical symmetry leading to (3.4) is broken, and further mathematical analysis must be applied.

To see the consequences of this symmetry break, consider a neutral particle n moving with velocity \mathbf{v}_n in a space occupied by ions. Assume that the distribution of ions is a Maxwellian described by the characteristic quantities n_i , \mathbf{u}_i , and T_i . Inserting these quantities into (3.3) and applying the substitution $\mathbf{w} = \mathbf{v} - \mathbf{u}$ to integrate in the rest frame of the ions yields

$$\langle \sigma g \rangle_{ni} = \left(\frac{m}{2\pi T} \right)^{3/2} \int \sigma(g) g \exp\left(-\frac{m_i w_i^2}{2T_i}\right) d\mathbf{v}_i, \quad (3.5)$$

where $g = |\mathbf{w}_i + \mathbf{u}_i - \mathbf{v}_n|$. Let the velocity of the neutral particle and the ion fluid velocity be defined by the components v_x , v_y , v_z and u_x , u_y , u_z in the lab frame, respectively, and define the velocity $\mathbf{d} = \mathbf{v}_n - \mathbf{u}_i$ as the difference between these. The orientation of \mathbf{d} in the lab frame is given by $\phi = \tan^{-1} \frac{d_y}{d_x}$ and $\theta = \cos^{-1} \frac{d_z}{d}$. A sketch of the situation is shown in figure 3.1. Define the *d-frame*, which shall be denoted with primes, through rotations of the lab frame according to the angles ϕ and θ , such that \mathbf{d} in the d-frame is $d'_x = 0$, $d'_y = 0$, $d'_z = d$. Specifically, the neutral frame is obtained from

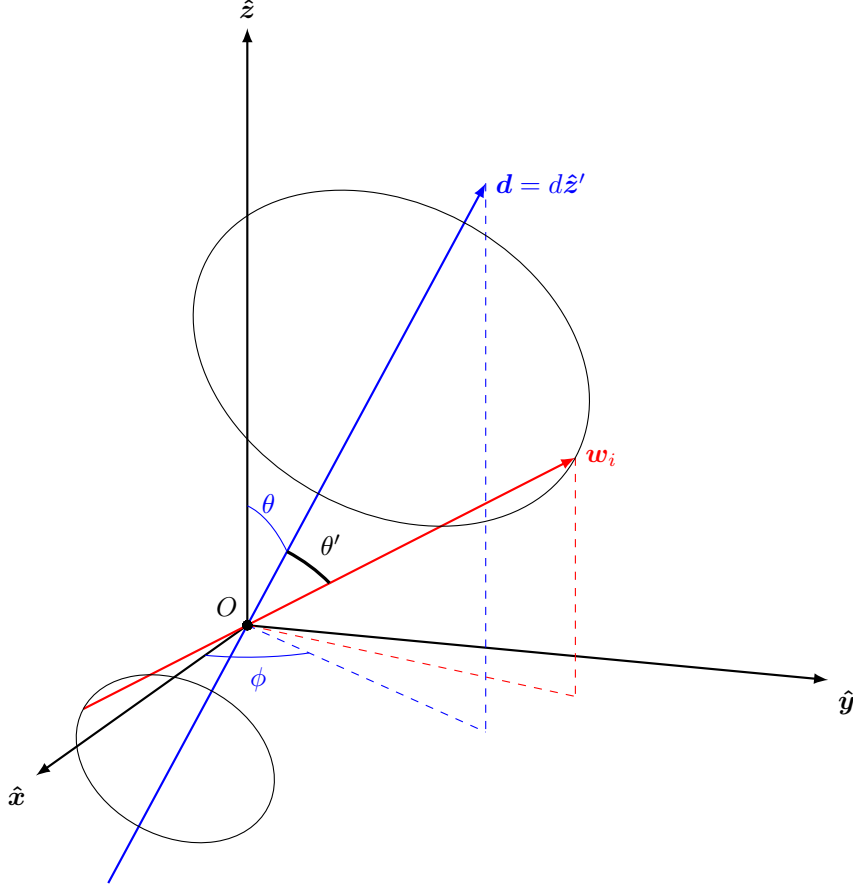


Figure 3.1: The lab frame is shown as the unprimed coordinate axes, while the neutral frame is denoted by primes. The angle θ' , is the polar angle of \mathbf{w}_i in the neutral frame. As the cross section only depends on the relative speed, and the ion velocity distribution is assumed spherically symmetric all random ion velocities connecting a point on each of the black circles through Origo will contribute equally to the reaction rate.

rotating the lab frame by the angle ϕ around the z -axis followed by a rotation of angle θ around the y -axis. The rotation of the coordinate axes around the y -axis and z -axis are defined by the linear transformations

$$\mathbf{R}_y(\alpha) = \begin{pmatrix} \cos \alpha & 0 & -\sin \alpha \\ 0 & 1 & 0 \\ \sin \alpha & 0 & \cos \alpha \end{pmatrix} \quad \text{and} \quad \mathbf{R}_z(\alpha) = \begin{pmatrix} \cos \alpha & \sin \alpha & 0 \\ -\sin \alpha & \cos \alpha & 0 \\ 0 & 0 & 1 \end{pmatrix} \quad (3.6)$$

respectively, where α is an angle. The transformation between the basis vectors of the lab frame and the neutral frame is written

$$\mathbf{r}' = \mathbf{R}_y(\theta)\mathbf{R}_z(\phi)\mathbf{r} \quad \text{and} \quad \mathbf{r} = \mathbf{R}_z(-\phi)\mathbf{R}_y(-\theta)\mathbf{r}', \quad (3.7)$$

where \mathbf{r} is an arbitrary vector expressed in the basis of the lab frame and \mathbf{r}' is the same vector expressed in the basis of the neutral frame.

By the definition of the d-frame

$$\mathbf{d}' = d\hat{\mathbf{z}}' \quad \text{and} \quad \mathbf{w}'_i = [\sin(\theta') \cos(\phi') \hat{\mathbf{x}}' + \sin(\theta') \sin(\phi') \hat{\mathbf{y}}' + \cos(\theta') \hat{\mathbf{z}}'] w_i. \quad (3.8)$$

In this frame the relative velocity is

$$\mathbf{g}' = \mathbf{d}' - \mathbf{w}'_i = \begin{pmatrix} -\sin(\theta') \cos(\phi') w_i \\ -\sin(\theta') \sin(\phi') w_i \\ d - \cos(\theta') w_i \end{pmatrix}, \quad (3.9)$$

yielding an expression for the relative speed

$$g(w_i, \theta')^2 = d^2 + w_i^2 - 2dw_i \cos(\theta'). \quad (3.10)$$

The independence of ϕ' in (3.10) indicates that in the d-frame, neutral-ion collisions are axially symmetric, as illustrated by the black circles of figure 3.1. Inserting the Maxwell-Boltzmann distribution in (3.3) and integrating over ϕ' which is trivial due to axis symmetry, yields

$$\langle \sigma g \rangle_{ni} = \frac{1}{\sqrt{2\pi}} \left(\frac{m_i}{T_i} \right)^{3/2} \int_0^\pi \int_0^\infty \exp\left(-\frac{m_i w_i^2}{2T_i}\right) \sigma(g) g w_i^2 \sin(\theta') dw_i d\theta'. \quad (3.11)$$

This expression shall be applied to sample the random velocities of ions going into charge exchange reactions. The sampled velocities are expressed in the d-frame but can be transformed to the lab frame by use of (3.6) and (3.7). Finally, the fluid velocity in the lab frame is added to get the total velocity of the reacting ion in the lab frame. By this method, PISAM ensures momentum and energy conservation in each and every vertex of ion-neutral collisions. The implementational details of this approach are covered in chapter 5.

Since reaction rates are historically provided for ${}^2\text{H}$ it is advantageous to be able to scale a given rate accordingly when modeling heavier isotopes. This scaling can be obtained by applying the substitutions

$$d = \sqrt{\frac{2E_d}{m_n}} \quad \text{and} \quad w_i = \sqrt{\frac{2E_i}{m_i}}, \quad (3.12)$$

where E_d is the neutral velocity in the rest frame of the ions, in (3.11). For a simple plasma with only one ion species, we can further assume $m_n = m_i = m$, and the rate of (3.11) can thus be written as

$$\langle \sigma g \rangle = \sqrt{\frac{2}{\pi m}} \left(\frac{1}{T_i} \right)^{3/2} \int \exp\left(-\frac{E_i}{T_i}\right) \sigma(g) G(E_i, E_d) \sin(\theta') dE_i d\theta'. \quad (3.13)$$

Where

$$G(E_i, E_d) = \sqrt{E_i(E_d + E_i - 2\sqrt{E_d E_i} \cos \theta')}. \quad (3.14)$$

It thus becomes clear that for simple plasmas the mass dependency of the rates of ion-neutral collisions scales as $m^{-1/2}$, and they are thus easily adjusted.

3.2 Elastic Binary Collisions in Fluids

To account for elastic binary collisions in fluids the considerations leading to (3.3) must be generalized. This generalization leads to the Boltzmann collision operator

$$\mathcal{E}_{12}(\mathbf{r}, \mathbf{v}_1, t) = \int d\mathbf{v}_2 \int_0^\pi \sin \chi d\chi \int_0^{2\pi} d\epsilon \left(\frac{d\sigma}{d\Omega} \right)_{12} g(f'_1 f'_2 - f_1 f_2), \quad (3.15)$$

describing the rate of change of the phase space density of species 1 per unit phase space volume per unit time at $\mathbf{r}, \mathbf{v}_1, t$, due to elastic collisions. In (3.15) χ is the scattering angle, ϵ is the azimuthal angle defining the plane in which the motion of the colliding particles is confined, g is the magnitude of the relative velocity, and $\left(\frac{d\sigma}{d\Omega} \right)_{12}$ is the differential cross section. The un-primed phase space distribution functions are evaluated at \mathbf{v}_1 and \mathbf{v}_2 respectively while the primed phase space distribution functions are evaluated at the velocities of the corresponding inverse encounter. For an exact introduction to these terms and quantities, and a derivation of the Boltzmann Collision operator presented with rare clarity, see appendix B.

The current section shall apply the Boltzmann collision operator to investigate the steady state of a mixture of fluids dominated by elastic collisions. This analysis reveals how elastic collisions relax the phase space density functions towards a common Maxwellian. This result has already been applied repeatedly and will serve as the very foundation of the fluid closure used in the next chapter. Understanding the conditions of applicability of this closure is necessary to substantiate the assertion that a fluid description of neutrals in the SOL is inadequate. Furthermore, the rate of relaxation towards the Maxwellian state will be used at the end of this chapter to estimate the effect of neglecting neutral-neutral collisions in PISAM. With this motivation, a generalized proof, including multiple fluid species, of the relaxation of the phase space density functions of collisional fluids towards a common Maxwellian is presented in the following section.

Steady State of a Fluid

The derivation presented in this section has found inspiration from several authors [64], [65], [66], but has been generalized from only treating one species to include an arbitrary number of species.

Consider a fluid system consisting of the species $s \in \{1, 2, \dots, n\}$ subject to no external forces. Assume that the state of the system is uniform such that

f_i is independent of \mathbf{r} . The Boltzmann equation for species i becomes

$$\frac{\partial f_i}{\partial t} = \sum_j \mathcal{E}_{ij}. \quad (3.16)$$

Where i and j are species indices. Boltzmann, and many others after him [64], [66], have introduced the function

$$H = \sum_i \int f_i \ln f_i d\mathbf{v}_i. \quad (3.17)$$

The time derivative of H is

$$\frac{\partial H}{\partial t} = \sum_i \int (1 + \ln f_i) \frac{\partial f_i}{\partial t} d\mathbf{v}_i = \sum_i \int (1 + \ln f_i) \sum_j \mathcal{E}_{ij} d\mathbf{v}_i. \quad (3.18)$$

Inserting the Boltzmann collision operator yields

$$\frac{\partial H}{\partial t} = \sum_i \sum_j \left(\frac{\partial H}{\partial t} \right)_{ij} = \quad (3.19)$$

$$\sum_i \sum_j \int d\mathbf{v}_i \int d\mathbf{v}_j \int_0^\pi \sin \chi d\chi \int_0^{2\pi} d\epsilon \left(\frac{d\sigma}{d\Omega} \right)_{ij} \int (1 + \ln f_i) g(f'_i f'_j - f_i f_j). \quad (3.20)$$

The strategy is to rewrite (3.21), to prove that H is a monotonic decreasing function. At first, a simplification of the terms where $i = j$ shall be sought using various index transformations. In this case, a notation distinguishing the two particles of species i , going into a collision must be introduced. Following the convention of [64] this shall be accomplished by writing one of the velocities without a species subscript, such that $\left(\frac{\partial H}{\partial t} \right)_{ii}$ reads

$$\left(\frac{\partial H}{\partial t} \right)_{ii} = \int d\mathbf{v} \int d\mathbf{v}_i \int_0^\pi \sin \chi d\chi \int_0^{2\pi} d\epsilon \left(\frac{d\sigma}{d\Omega} \right)_{ii} \int (1 + \ln f_i) g(f'_i f' - f_i f). \quad (3.21)$$

The terms of (3.21) representing collisions of particles both belonging to species i can be rewritten utilizing that v and v_i can be interchanged since they are both "dummy" variables with the same integration bounds and are thus treated symmetrically in the integral. After performing this swapping $\left(\frac{\partial H}{\partial t} \right)_{ii}$ can be written

$$\left(\frac{\partial H}{\partial t} \right)_{ii} = \int d\mathbf{v} \int d\mathbf{v}_i \int_0^\pi \sin \chi d\chi \int_0^{2\pi} d\epsilon \left(\frac{d\sigma}{d\Omega} \right)_{ii} \int (1 + \ln f) g(f' f'_i - f f_i). \quad (3.22)$$

Another way of rewriting (3.21) is obtained utilizing the symmetry of direct and inverse collisions. By arguments similar to those leading to (B.7) it can

be shown that v_i and v_j can be replaced by v'_i and v'_j and vice versa such that $(\frac{\partial H}{\partial t})_{ii}$ reads

$$\left(\frac{\partial H}{\partial t}\right)_{ii} = \int d\mathbf{v} \int d\mathbf{v}_i \int_0^\pi \sin \chi d\chi \int_0^{2\pi} d\epsilon \left(\frac{d\sigma}{d\Omega}\right)_{ii} \int (1 + \ln f'_i) g(f_i f - f'_i f'). \quad (3.23)$$

Swapping the dummy indices of (3.23) yields

$$\left(\frac{\partial H}{\partial t}\right)_{ii} = \int d\mathbf{v} \int d\mathbf{v}_i \int_0^\pi \sin \chi d\chi \int_0^{2\pi} d\epsilon \left(\frac{d\sigma}{d\Omega}\right)_{ii} \int (1 + \ln f') g(f f_i - f' f'_i). \quad (3.24)$$

Adding (3.21), (3.22), (3.23) and (3.24), $(\frac{\partial H}{\partial t})_{ii}$ can be put in the form

$$2 \left(\frac{\partial H}{\partial t}\right)_{ii} = \frac{1}{2} \int d\mathbf{v} \int d\mathbf{v}_i \int_0^\pi \sin \chi d\chi \int_0^{2\pi} d\epsilon \left(\frac{d\sigma}{d\Omega}\right)_{ii} \int \ln \left(\frac{f f_i}{f' f'_i}\right) g(f' f'_i - f f_i). \quad (3.25)$$

The "cross terms" of (3.21), i.e. the terms where $i \neq j$, can be combined in the pairs (i, j) and (j, i) to yield

$$\begin{aligned} \left(\frac{\partial H}{\partial t}\right)_{ij} + \left(\frac{\partial H}{\partial t}\right)_{ji} &= \\ \int d\mathbf{v}_i \int d\mathbf{v}_j \int_0^\pi \sin \chi d\chi \int_0^{2\pi} d\epsilon \left(\frac{d\sigma}{d\Omega}\right)_{ij} \int (2 + \ln(f_i f_j)) g(f'_i f'_j - f_i f_j), \end{aligned} \quad (3.26)$$

were the symmetry of binary collisions was used to impose $(\frac{d\sigma}{d\Omega})_{ij} = (\frac{d\sigma}{d\Omega})_{ji}$. Switching primed and unprimed velocities of this expression yields

$$\begin{aligned} \left(\frac{\partial H}{\partial t}\right)_{ij} + \left(\frac{\partial H}{\partial t}\right)_{ji} &= \\ \int d\mathbf{v}_i \int d\mathbf{v}_j \int_0^\pi \sin \chi d\chi \int_0^{2\pi} d\epsilon \left(\frac{d\sigma}{d\Omega}\right)_{ij} \int (2 + \ln(f'_i f'_j)) g(f_i f_j - f'_i f'_j). \end{aligned} \quad (3.27)$$

Adding (3.26) and (3.27) yields

$$\begin{aligned} \left(\frac{\partial H}{\partial t}\right)_{ij} + \left(\frac{\partial H}{\partial t}\right)_{ji} &= \\ \frac{1}{2} \int d\mathbf{v}_i \int d\mathbf{v}_j \int_0^\pi \sin \chi d\chi \int_0^{2\pi} d\epsilon \left(\frac{d\sigma}{d\Omega}\right)_{ij} \int \ln \left(\frac{f_i f_j}{f'_i f'_j}\right) g(f'_i f'_j - f_i f_j). \end{aligned} \quad (3.28)$$

To directly apply this result rewrite the sum of (3.20)

$$\sum_i \sum_j \left(\frac{\partial H}{\partial t}\right)_{ij} = \sum_i \sum_{j \geq i} \left[\left(\frac{\partial H}{\partial t}\right)_{ij} + \left(\frac{\partial H}{\partial t}\right)_{ji} \right] (1 - \frac{1}{2} \delta_{ij}) \quad (3.29)$$

Combining (3.25), (3.28), and (3.29), $\frac{\partial H}{\partial t}$ can finally be written as

$$\begin{aligned} \frac{\partial H}{\partial t} = & \frac{1}{2} \sum_i \sum_{j \geq i} \left(1 - \frac{1}{2} \delta_{ij}\right) \int d\mathbf{v}_i \int d\mathbf{v}_j \int_0^\pi \sin \chi d\chi \\ & \int_0^{2\pi} d\epsilon \left(\frac{d\sigma}{d\Omega}\right)_{ij} \int \ln \left(\frac{f_i f_j}{f'_i f'_j}\right) g(f'_i f'_j - f_i f_j). \end{aligned} \quad (3.30)$$

This is a neat way of formulating $\frac{\partial H}{\partial t}$, but once again caution must be shown when interpreting the terms where $i = j$. In this case, the instances of $f_i f_i$ and $f'_i f'_i$ should be read $f_i(\mathbf{r}, \mathbf{v}_i, t) f_i(\mathbf{r}, \mathbf{v}, t)$ and $f_i(\mathbf{r}, \mathbf{v}'_i, t) f_i(\mathbf{r}, \mathbf{v}', t)$ respectively i.e. distinguishing the two particles coming into and the particles going out of the collision.

The reward of all this work is that (3.30) reveals that regardless of the sign of $(f'_i f'_j - f_i f_j)$ the integrand of (3.30) will always be negative, indicating that H is a monotonic decreasing function. Moreover, it can be shown that H is bounded from below [64], meaning that the system must tend to some equilibrium of $\frac{\partial H}{\partial t} = 0$ if affected only by elastic collisions. $\frac{\partial H}{\partial t} = 0$ is obviously satisfied exactly when

$$f_i f_j = f'_i f'_j \Rightarrow \ln(f_i) + \ln(f_j) - \ln(f'_i) - \ln(f'_j) = 0. \quad (3.31)$$

Before moving on to determine f_i notice what this equation actually states; In equilibrium, each pair of direct and inverse collisions of any two species of particles are exactly balanced. This absolutely breathtaking result is an example of *detailed balancing* recognized as a general principle of statistical mechanics. (3.31) shows that for two particles of any two species, the quantity $\ln(f_i(v_i)) + \ln(f_j(v_j))$ is conserved during binary collisions for a system in equilibrium i.e. $\frac{\partial H}{\partial t} = 0$. Such summational invariants must be linear combinations of the fundamental invariants of particle number, momentum and energy [64], [66], such that $\ln(f_i)$ is of the form

$$(\ln f_i)(\mathbf{v}) = \alpha_i^{(0)} + \boldsymbol{\alpha}_i^{(1)} \cdot m_i \mathbf{v} + \alpha_i^{(2)} \frac{1}{2} m_i v^2, \quad (3.32)$$

where $\alpha_i^{(k)}$ for $k = 0, 1, 2$ are constants. Inserting the form of $\ln f$ from (3.32) in (3.31) it is easily shown that for energy and momentum to be conserved $\boldsymbol{\alpha}_i^{(1)}$ and $\alpha_i^{(2)}$, must be equal for all species i.e. $\boldsymbol{\alpha}_i^{(1)} = \boldsymbol{\alpha}^{(1)}$ and $\alpha_i^{(2)} = \alpha^{(2)}$. Rewriting (3.32) and solving for f_i yields

$$f_i = \ln a_i^{(0)} \exp \left(-\alpha^{(2)} \frac{1}{2} m_i w'^2 \right) \quad (3.33)$$

Where $\ln a_i^{(0)}$ is a new constant, and $\mathbf{w}' = \mathbf{v} - \frac{\boldsymbol{\alpha}^{(1)}}{\alpha^{(2)}}$ is a convenient abbreviation. The constants $a_i^{(0)}$, $\boldsymbol{\alpha}^{(1)}$ and $\alpha^{(2)}$, are determined by demanding that

f_i corresponds with the definitions of density, fluid velocity, and temperature, given by (A.2) and (A.4) and repeated here for convenience,

$$n_i = \int f_i d\mathbf{v}_i, \quad \mathbf{u}_i = \frac{1}{n_i} \int v_i f_i d\mathbf{v}_i, \quad T_i = \frac{m}{3n} \int (\mathbf{v} - \mathbf{u})^2 f d\mathbf{v}. \quad (3.34)$$

This system of five scalar equations is solved to determine $\alpha_i^{(0)}$, $\alpha^{(2)}$, and \mathbf{w}' in terms of the macroscopic variables. Inserting these expressions in (3.33) and demanding that $\int f_i d\mathbf{v}_i = n_i$ yields

$$f_i(\mathbf{v}) = n_i \left(\frac{m_i}{2\pi T} \right)^{3/2} \exp \left(-\frac{m_i(\mathbf{v} - \mathbf{u})^2}{2T} \right) \quad (3.35)$$

Which is recognized as the Maxwellian velocity distribution. Notice that in equilibrium all species move with the same fluid velocity and have the same temperature.

Relaxation time

Plasma species:

As shown above, all species in a composite fluid tend to a Maxwellian of common temperature and fluid velocity. The time for a distribution function to reach a near Maxwellian state is termed the relaxation time. For a single gas of species s the relaxation time is of the order of the collision time, [17]. The collision time can be approximated by the expression

$$\tau_{ss} = \frac{1}{\sqrt{2} n_s \sigma_{ss} \bar{v}_s}, \quad (3.36)$$

provided by [66]. Here \bar{v} is the average particle speed which can be approximated by the thermal velocity $v_{t,s} \propto (\frac{T}{m})^{1/2}$. Assuming that T_e and T_i are similar, the ratio of relaxation times for ions and electrons can be approximated by

$$\frac{\tau_{ii}}{\tau_{ee}} \approx \left(\frac{m_i}{m_e} \right)^{1/2}, \quad (3.37)$$

showing that the electrons are driven significantly faster towards a Maxwellian due to self-collisions than is the case for the ions. The relaxation time for convergence towards a common equilibrium can be approximated by considering the energy exchange rate in binary collisions of particles with a large mass ratio. The energy transfer rate is suppressed by approximately m_e/m_i as compared to the transfer of energy in collisions between particles of equal mass [17]. Since the collision time τ_{ie} is of the order of τ_{ee} , (due to the relative velocity being of the same order) we find the relations

$$\tau_{ee} \approx \tau_{ii} \left(\frac{m_e}{m_i} \right)^{1/2} \approx \tau_{ie} \frac{m_e}{m_i}. \quad (3.38)$$

Ions and electrons thus reach species-internal equilibrium a lot faster than they reach a common equilibrium. It is thus not uncommon to have electrons and ions at different temperatures, both well approximated by Maxwellian velocity distributions. This is one of the main reasons for modeling plasma as two individual interacting fluids as it is done in HESEL and countless other plasma models.

Relaxation of Neutrals

PISAM injects neutrals into the chamber of a Tokamak which, close to the wall, is under vacuum-like conditions. Currently, PISAM does not include neutral-neutral collisions meaning that as the particles enter the reaction chamber they move along straight lines until plasma density becomes large enough for interactions to be plausible. The neutrals enter the system with a Maxwellian velocity distribution, but the fast particles quickly escape the injection zone, while the slow particles build up around the injection point, resulting in skewed Maxwellian distributions. To assess whether this deviation from a Maxwellian represents physical reality or is a shortcoming of the model, consider the collision time of neutral-neutral collisions between hydrogen molecules. The cross section of elastic collisions between hydrogen molecules is approximately $5 \cdot 10^{-18} \text{ m}^2$ at relevant temperatures, [67]. Little is currently known about the plasma density close to the wall of toroidal containment devices. Previous theoretical, [68] and experimental, [69], findings suggests that it can be as high as 10^{19} m^{-3} , depending on the puffing rate. Using (3.36) with an injection temperature of 0.3 eV ¹² yields a collisions time of $\sim 1 \text{ ms}$. Assuming that the injected molecules travel approximately 5 cm in the radial direction before being dissociated by electron impact, around 99%¹³ of molecules will be dissociated within a millisecond. In conclusion, neglecting neutral-neutral collisions is an acceptable approximation.

¹²This is the temperature used in current simulations.

¹³This number is obtained by integration of the marginal Maxwellian velocity distribution with respect to the radial direction.

4 The nHESEL Equations

This chapter presents the nHESEL (neutral augmented **H**ot **E**dge **S**O**L** **E**lectrostatic) equations. HESEL is a 2D¹⁴ fluid model developed to describe plasma edge turbulence at the outboard midplane of a Tokamak. In the nHESEL model, the equations of HESEL are modified to account for source terms originating from inelastic plasma neutral collisions. The nHESEL equations were first presented in [70]. In this chapter, it is shown that the nHESEL equations of [70] have several flaws, regarding higher-order terms, and the corrected set of equations is presented. The following chapter thus outlines the path from the transport equations of chapter 2 all the way to the nHESEL equations. This includes the method of fluid closure, the application of drift ordering, and an account of the assumptions leading from the drift-reduced Braginskii equations to the final nHESEL equations. Terming HESEL as a 2D model can be somewhat misleading. A precise understanding of the dimensionality of HESEL is necessary when coupling it with PISAM, and shall thus be detailed at the end of this chapter.

4.1 Fluid Closure

It is apparent from (2.6) that no set of closed equations can be obtained from moments of the Boltzmann equation. A closure thus has to be applied to establish the relation between the macroscopic variables and $\bar{\pi}_s$, $E_s^{(\frac{1}{2}mv^2)}$, $\mathbf{E}_s^{(mv)}$ and \mathbf{q}_s for a fluid theory to be complete. Note that the fluid closure presented in this chapter does not include the inelastic source terms. A closure can be stated phenomenologically e.g. by assuming a constant temperature or local thermodynamic equilibrium, *or* it can be an asymptotic closure. The latter aims to approximate solutions of the Boltzmann equation as a function of macroscopic variables. This solution can then be inserted in (A.11), (2.5) and (2.18) to approximate $\bar{\pi}_s$, $E_s^{(\frac{1}{2}mv^2)}$, $\mathbf{E}_s^{(mv)}$ and \mathbf{q}_s thus closing the continuity,

¹⁴The meaning of 2D is detailed at the end of the chapter.

momentum and energy equations.

As derived in the former chapter on collision theory, any fluid affected only by binary collisions will tend to a Maxwellian velocity distribution. This is the foundation of the Chapman Enskog closure scheme presented in [64] and applied to the case of a two-fluid magnetic plasma by Braginskii in [17]. The general idea is to expand the phase space distribution function f_s of species s as

$$f_s(\mathbf{r}, \mathbf{v}) = f_s^0 + f_s^1 + f_s^2 + \dots \quad (4.1)$$

where $f_s^0(\mathbf{r}, \mathbf{v})$ is a Maxwellian distribution specified by the macroscopic variables, n_s , \mathbf{u}_s and T_s . f_s^n , for $n \in \mathbb{N}$, give perturbations to this Maxwellian. The magnitude of these perturbations is found to decrease rapidly with increasing n under certain conditions of applicability, which shall be outlined later in this chapter, as well as assumptions on the ordering of the terms in the Boltzmann equation. Due to the rapid decrease of f_s^n and the mathematical complexity involved in determining f_s^n for $n > 1$ the series of (4.1) is truncated after f_s^1 in almost any practical application.

To simplify the Boltzmann equation, the coulomb collision operator can be rewritten utilizing the effect of Debye shielding. By these means Braginskii shows that the collision operator of coulomb collisions in plasma is approximately bilinear, thus resembling the form of the Boltzmann collision operator of (3.15). Given that $f_s^n \ll f_s^{(n+1)}$ and assuming that the magnetic term and the collision term of the Boltzmann equation are large compared to the remaining terms (i.e. time and space derivatives of f_s and the electric part of the Lorentz force), the Boltzmann equation can, in principle, be solved by an iterative procedure successively determining higher order approximations to f_s . In the following, the collisional term and the magnetic term shall be referred to as "large terms", while the remaining terms in the Boltzmann equation are referred to as "small". Let the ordering be such that the small terms of f_s^n are of the order of the large terms of $f_s^{(n+1)}$. Notice that the magnetic term $\frac{e}{m_s} \mathbf{v} \times \mathbf{B} \cdot \nabla_v f_s$ vanishes for a spherically symmetric velocity distribution function i.e. the proof provided in the last chapter for the equilibrium state of collisional fluids apply also to magnetic plasma, and so the equilibrium distribution of a magnetic plasma is indeed Maxwellian. Having determined $f_s^{(n)} = \sum_{i=0}^n f_s^i$, the next approximation, f_s^{n+1} , is determined, by the following series of steps (The following describes the case of a two-fluid system of species 1 and 2):

- For $s \in \{1, 2\}$ insert $f_s^{(n+1)} = f_s^{(n)} + f_s^{n+1}$ into the Boltzmann equation of species s . Remember that all the terms of $f_s^{(n)}$ are already approximated

in terms of the macroscopic variables.

- Do only account for f_s^{n+1} in the large terms of the Boltzmann equation. In the Collision operator only terms linear in f_s^{n+1} are kept while the quadratic terms are discarded. This applies in self-collision terms as well as cross-collision terms. As a consequence of the ordering, only small terms include derivatives of f_s . Since the small terms only account for $f_s^{(n)}$, the spatial derivatives of f_s in the small terms are already expressed in terms of the macroscopic variables.
- Use the transport equations (the continuity, momentum, and energy equations), to eliminate the time derivative of $f_s^{(n)}$. Denote that the approximate expressions $\bar{\boldsymbol{\pi}}_s^n$, $(E_s^{(\frac{1}{2}mv^2)})^n$, $(\mathbf{E}_s^{(mv)})^n$ and \mathbf{q}_s^n thus comes into the time derivative of f_s .
- At this point a set of two linear integro-differential equations is obtained. By advanced mathematical techniques, these equations are solved for f_s^{n+1} ¹⁵.
- The obtained approximations for f_s^{n+1} are then added to $f_s^{(n)}$ and used to determine $\bar{\boldsymbol{\pi}}_s^{(n+1)}$, $(E_s^{(\frac{1}{2}mv^2)})^{(n+1)}$, $(\mathbf{E}_s^{(mv)})^{(n+1)}$ and $\mathbf{q}_s^{(n+1)}$.
- $f_s^{(n+1)}$, $\bar{\boldsymbol{\pi}}_s^{(n+1)}$, $(E_s^{(\frac{1}{2}mv^2)})^{(n+1)}$, $(\mathbf{E}_s^{(mv)})^{(n+1)}$ and $\mathbf{q}_s^{(n+1)}$ is then used to evaluate $f_s^{(n+2)}$.

For a two-fluid magnetic plasma with the assumption of quasi neutrality and truncating (4.1) after f_s^1 one arrives at the Braginskii equations (Here slightly modified to include inelastic collisions):

$$\frac{d_e n}{dt} + n \boldsymbol{\nabla} \cdot \mathbf{u}_e = I_e^{(1)}, \quad (4.2)$$

$$m_e n \frac{d_e \mathbf{u}_e}{dt} + \boldsymbol{\nabla} p_e + \boldsymbol{\nabla} \cdot \bar{\boldsymbol{\pi}}_e + n e (\mathbf{E} + \mathbf{u}_e \times \mathbf{B}) \quad (4.3)$$

$$= \mathbf{R} + \mathbf{I}_e^{(mv)} - m_e \mathbf{u}_e I_e^{(1)}$$

$$\frac{3}{2} \frac{d_e p_e}{dt} + \frac{5}{2} p_e \boldsymbol{\nabla} \cdot \mathbf{u}_e + \bar{\boldsymbol{\pi}}_e : \boldsymbol{\nabla} \mathbf{u}_e + \boldsymbol{\nabla} \cdot \mathbf{q}_e \quad (4.4)$$

$$= -\Delta Q + \mathbf{R} \cdot (\mathbf{u}_i - \mathbf{u}_e) + I_e^{(\frac{1}{2}mv^2)} - \mathbf{u}_e \cdot \mathbf{I}_e^{(mv)} + \frac{1}{2} m_e u_e^2 I_e^{(1)},$$

¹⁵In a magnetized plasma governed by coulomb collisions, further approximations to the collision operator are needed to solve these equations. Braginskii accomplishes this by utilizing the large mass ratio of ions and electrons to justify certain lower-order expansions.

for electrons and

$$\frac{d_i n}{dt} + n \nabla \cdot \mathbf{u}_i = I_i^{(1)}, \quad (4.5)$$

$$m_i n \frac{d_i \mathbf{u}_i}{dt} + \nabla p_i + \nabla \cdot \bar{\pi}_i - ne (\mathbf{E} + \mathbf{u}_i \times \mathbf{B}) \\ = -\mathbf{R} + \mathbf{I}_i^{(mv)} - m_i \mathbf{u}_i I_i^{(1)} \quad (4.6)$$

$$\frac{3}{2} \frac{d_i p_i}{dt} + \frac{5}{2} p_i \nabla \cdot \mathbf{u}_i + \bar{\pi}_i : \nabla \mathbf{u}_i + \nabla \cdot \mathbf{q}_i \quad (4.7)$$

$$= \Delta Q + I_i^{(\frac{1}{2}mv^2)} - \mathbf{u}_i \cdot \mathbf{I}_i^{(mv)} + \frac{1}{2} m_i u_i^2 I_i^{(1)}, \quad (4.8)$$

for ions. Note that the source terms due to elastic collisions have been rewritten in accordance with Braginskii's notation. \mathbf{R} denotes the friction force arising from electron-ion collisions. ΔQ is the heat transfer from electrons to ions resulting from these collisions while $\mathbf{R} \cdot (\mathbf{u}_i - \mathbf{u}_e)$ is the rate of heat transfer from kinetic to thermal energy of the electrons due to collisions with ions. The latter term is negligible for the ions do the large mass difference between ions and electrons. The value of Braginskii's work lies expressing $\bar{\pi}_s$, ΔQ , \mathbf{R} and \mathbf{q}_s in terms of macroscopic variables. These are given in [17] and shall not be repeated here.

Conditions of Applicability

If a fluid is to be described as approximately Maxwellian, which is the very foundation of the closure scheme discussed above, the mean free path of particles constituting the fluid must be small compared to the characteristic length scale of changes of the macroscopic variables. The intuition behind this statement is the following: If the mean free path \tilde{l} is larger than or comparable to the characteristic length scale, L , of changes of the macroscopic variables, the particles contained at the volume $d\mathbf{r}$ at point \mathbf{r} had their last collision, at positions in space \mathbf{r}' , such that $|\mathbf{r}' - \mathbf{r}| \sim L$. Consequently, these particles represent the conditions of completely different macroscopic properties, and thus cannot form a Maxwellian formulated by the local macroscopic properties. A further condition is, that the collision time τ must be small compared to the characteristic rate of change of the macroscopic variables. Assume on the other hand, that the collision frequency ν is larger than or comparable to the characteristic rate of change ω_{char} . In that case, particles contained in the volume $d\mathbf{r}$ at point \mathbf{r} at time t had their last collision in plasma conditions representing different macroscopic properties, as they happened at times

separated by a time difference that is larger than or comparable to $1/\omega_{char}$. That is to say, only when $\omega_{char} \ll \nu$ the range of times at which these collisions happened will be so small that all the particles represent the same fluid conditions.

Magnetized Plasma

In a magnetized plasma the condition $\tilde{l} \ll L$ is relaxed to the condition $\tilde{l}_{\parallel} \ll L_{\parallel}$ and $\rho \ll L_{\perp}$. In the presence of a magnetic field, the motion perpendicular to the field lines is bounded by the Larmor radius ρ . The mean free path in the field-perpendicular plane is given as $\tilde{l} = v_{t,\perp}\tau = \rho\Omega_c\tau$, where $v_{t,\perp} = \sqrt{\frac{T}{m}}$ is the most probable velocity obtained from projecting a velocity sampled from a 3D Maxwellian onto an arbitrary 2D plane, and Ω_c is the cyclotron frequency. The mean free path is thus effectively reduced by a factor $\Omega_c\tau$ by the introduction of a magnetic field.

In most fusion plasmas the condition $\tilde{l}_{\parallel} \ll L_{\parallel}$ is not satisfied meaning that the classical transport theory obtained from Braginskii's closure is not adequate in describing parallel dynamics [63]. Instead, Neo-classical transport theory might be employed to correct the transport equations, at the cost of a significantly increased mathematical complexity. Neo-classical effects are inherently three-dimensional, but as we shall see, HESEL tries to adjust for neo-classical effects by a synthetic adjustment of the perpendicular diffusion coefficients.

One further assumption is required for the Braginskii equations to be applicable. The gyration motion of the charged particles constituting the plasma is not taken into account in the simplification of the coulomb collision operator used to derive the Braginskii equations. The underlying assumption is that the spatial dimension of collisions is small compared to the Larmor radius. The largest distance for coulomb collisions in plasma is the Debye length, as fields are shielded outside this range. The assumption is thus that the Larmor radius is significantly larger than the Debye radius, $\delta_D = \sqrt{\frac{T}{4\pi e^2 n}}$. The conditions of applicability of the Braginskii equations can thus be summarized as

$$\frac{\tilde{l}_{\parallel}}{L_{\parallel}} \ll 1, \quad \frac{\rho}{L_{\perp}} \ll 1, \quad \frac{\omega_{char}}{\nu} \ll 1, \quad \frac{\delta_D}{\rho} \ll 1 \quad (4.9)$$

4.2 Drift Ordering

As mentioned above, the conditions of applicability of the Braginskii equations are not necessarily satisfied along the direction of the magnetic field. HESEL,

however, only self-consistently includes perpendicular dynamics, for which the Braginskii closure is valid. To obtain the perpendicular part of the momentum equation the cross product of (2.14) is taken with $\hat{\mathbf{b}}$, which is the unit vector along the magnetic field. Dividing by qnB and rearranging yields

$$\begin{aligned} \mathbf{u}_\perp = & -\frac{\nabla\phi \times \hat{\mathbf{b}}}{B} + \frac{\hat{\mathbf{b}} \times \nabla p}{qnB} + \frac{1}{\Omega_c} \hat{\mathbf{b}} \times \frac{d\mathbf{u}}{dt} + \frac{\hat{\mathbf{b}} \times \nabla \cdot \bar{\pi}}{qnB} \\ & - \frac{\hat{\mathbf{b}} \times \mathbf{E}^{(mv)}}{qnB} - \frac{\hat{\mathbf{b}} \times \mathbf{I}^{(mv)}}{qnB} + \frac{\hat{\mathbf{b}} \times m\mathbf{u}I^{(1)}}{qnB} \quad (4.10) \\ = & \mathbf{u}_E + \mathbf{u}_D + \mathbf{u}_p + \mathbf{u}_\pi + \mathbf{u}_R + \mathbf{u}_{IR} + \mathbf{u}_{In}, \end{aligned}$$

where it has been assumed that the field is electrostatic and species subscripts have been omitted to ease notation. The last line of (4.10) simply serves to name the terms for future reference. In order to simplify the Braginskii equations in a manner that focuses attention on the turbulence phenomena of interest, drift ordering is imposed. In drift ordering, it is assumed that the characteristic spatial and temporal scales of change of the macroscopic variables are slow compared to those set by the gyro motion. Furthermore, it is assumed that the fluid speeds, u_\perp , are small compared to thermal speeds, $v_{t,\perp}$. Following Fitzpatrick, [63], this amounts to the following restriction on the conditions of (4.9):

$$\frac{\rho_i}{L_\perp} \ll 1, \quad \frac{\rho_i}{l_\perp} \ll 1, \quad \frac{u}{v_t} \ll 1, \quad \frac{\delta_D}{\rho} \ll 1 \quad (4.11)$$

The reason for letting the ions set the scales is that they gyrate slower and with a larger radius than electrons, and they thus set the most strict conditions on the system. Under this ordering it can be shown [71], [63], that to lowest order (4.10) reduces to

$$\mathbf{u}_{\perp,0} = -\frac{\nabla\phi \times \hat{\mathbf{b}}}{B} + \frac{\hat{\mathbf{b}} \times \nabla p}{qnB} = \mathbf{u}_E + \mathbf{u}_D, \quad (4.12)$$

with \mathbf{u}_E and \mathbf{u}_D denoting the $\mathbf{E} \times \mathbf{B}$ -drift and diamagnetic drift respectively. At this point, it is instructive to consider the contribution to the continuity equation from diamagnetic drift in a uniform and homogeneous magnetic field

$$\nabla \cdot (n\mathbf{u}_D) = \nabla \cdot \frac{\hat{\mathbf{b}} \times \nabla p}{qB} = \frac{1}{qB} (\nabla p \cdot \nabla \times \hat{\mathbf{b}} - \hat{\mathbf{b}} \cdot \nabla \times \nabla p) = 0 \quad (4.13)$$

Reflecting the fact that the diamagnetic drift is not a guiding center drift. Under the same conditions, the advective contribution from the diamagnetic drift to the pressure equation is

$$\mathbf{u}_D \cdot \nabla p = \frac{\hat{\mathbf{b}} \times \nabla p}{qnB} \cdot \nabla p = 0. \quad (4.14)$$

This reflects the fact that the diamagnetic drift moves fluid along isobaric surfaces and thus cannot advect pressure. In conclusion, the advection of density and energy-density is dominated by the $\mathbf{E} \times \mathbf{B}$ -drift in drift ordering. The diamagnetic drift does however play an important role when the magnetic field is non-uniform, as it includes the $\nabla \mathbf{B}$ - and curvature drifts. Terms like $\nabla \cdot (n\mathbf{u}_D)$ and $\nabla \cdot (p\mathbf{u}_D)$ are thus retained in the following.

The first order correction to (4.12) is obtained by inserting (4.12) iteratively into the remaining drifts of (4.10). So as an example: To obtain the first order contribution to \mathbf{u}_\perp from $\frac{\hat{\mathbf{b}} \times \nabla \bar{\pi}}{enB}$, one should evaluate $\bar{\pi}_\perp$, as given by Braginskii in [17], with $\mathbf{u}_\perp = \mathbf{u}_{\perp,0}$. The resulting approximation of $\bar{\pi}$ is then inserted in the expression for the drift i.e. $\frac{\hat{\mathbf{b}} \times \nabla \cdot \bar{\pi}}{enB}$. This procedure can be used to write approximate expressions for all the drifts of (4.10), the results are presented in [70] and shall not be repeated here. Such analysis reveals that the viscous stress tensor is mass dependent with the proportionality $m^{3/2}$ [30]. Furthermore, we have already seen that \mathbf{u}_p is proportional to m . Due to the small electron mass, these drifts are neglected for electrons. Similarly the drifts \mathbf{u}_{IR} and \mathbf{u}_{In} , arising due to inelastic collisions are proportional to the electron mass, and are also neglected for consistency.

With these assumptions, the Braginskii equations can be reduced as follows. The electron continuity equation becomes

$$\frac{\partial n}{\partial t} + \nabla \cdot (n\mathbf{u}_E + n\mathbf{u}_{D,e} + n\mathbf{u}_R + n\hat{\mathbf{b}}\mathbf{u}_{\parallel,e}) = I^{(1)}, \quad (4.15)$$

Here the material derivatives, $\frac{d}{dt}$ have been written explicitly for clarity. Denote that the resistive drift due to elastic electron-ion collisions is identical for electrons and ions due to momentum conservation. Also, the particle source term is identical for ions and electrons due to particle conservation. The species subscript on these terms is hence omitted. Subtracting the electron continuity equation from the ion continuity equation yields the vorticity equation

$$\nabla \cdot (n\mathbf{u}_{p,i} + n\mathbf{u}_{D,i} - n\mathbf{u}_{D,e} + \hat{\mathbf{b}}J_\parallel/e + n\mathbf{u}_{\pi,i} + n\mathbf{u}_{IR,i} + n\mathbf{u}_{In,i}) = 0 \quad (4.16)$$

Where $J_\parallel = en(u_{\parallel i} - u_{\parallel e})$ and e is the elementary charge. The pressure equation for electrons is written

$$\begin{aligned} & \frac{3}{2} \frac{\partial p_e}{\partial t} + \frac{3}{2} \nabla \cdot (p_e [\mathbf{u}_E + \mathbf{u}_{D,e} + \mathbf{u}_R + \hat{\mathbf{b}}\mathbf{u}_{\parallel e}]) \\ & + p_e \nabla \cdot [\mathbf{u}_E + \mathbf{u}_{D,e} + \mathbf{u}_R + \hat{\mathbf{b}}\mathbf{u}_{\parallel e}] + \nabla \cdot \mathbf{q}_e \\ & = -\Delta Q + \mathbf{E}_e^{(mv)} \cdot (\mathbf{u}_i - \mathbf{u}_e) + I_e^{(\frac{1}{2}mv^2)}, \end{aligned} \quad (4.17)$$

where the terms including the momentum and particle sources due to inelastic collisions are neglected in consistency with the electron momentum equation where the corresponding terms were also neglected. The particle source dependent term, $\frac{1}{2}m_e u_e^2 I^{(1)}$ is also neglected due to the ratio $u_e/v_{t,e}$ being very small for the light electrons. For the ions, the pressure equation becomes

$$\begin{aligned} & \frac{3}{2} \frac{\partial p_i}{\partial t} + \frac{3}{2} \nabla \cdot (p_i [\mathbf{u}_E + \mathbf{u}_{Di} + \mathbf{u}_{pi} + \mathbf{u}_{\pi i} + \mathbf{u}_R + \mathbf{u}_{IR,i} + \mathbf{u}_{In,i} + \hat{\mathbf{b}}u_{||i}]) \\ & + p_i \nabla \cdot [\mathbf{u}_E + \mathbf{u}_{Di} + \mathbf{u}_{pi} + \mathbf{u}_{\pi i} + \mathbf{u}_R + \mathbf{u}_{IR,i} + \mathbf{u}_{In,i} + \hat{\mathbf{b}}u_{||i}] + \nabla \cdot \mathbf{q}_i \\ & + \bar{\boldsymbol{\pi}}_{i\perp}^c : \nabla \mathbf{u}_{i\perp,0} = \Delta Q + I_i^{(\frac{1}{2}mv^2)} - \mathbf{u}_{i\perp,0} \cdot \mathbf{I}_i^{(mv)} + \frac{1}{2} m_i u_{i\perp,0}^2 I^{(1)}, \end{aligned} \quad (4.18)$$

In the case of the ions, the pressure sources arising from momentum and particle source terms, brought into the ion pressure equation through substitution with the momentum and continuity equations are retained. Only the lowest order drifts contribute to these terms as they should be considered small due to drift ordering. Also, derivatives of the drifts arising from inelastic momentum and particle sources are retained in consistency with (4.16). The perpendicular part of the ion viscous stress tensor $\bar{\boldsymbol{\pi}}_{\perp,i} = \bar{\boldsymbol{\pi}}_{\perp,i}^c + \bar{\boldsymbol{\pi}}_{\perp,i}^*$ has been divided into a collisional and a gyro viscous part. It has been applied in (4.18) that $\bar{\boldsymbol{\pi}}_{\perp,i}^* : \nabla \mathbf{u}_{i\perp,0} = 0$ when $\bar{\boldsymbol{\pi}}_{\perp,i}$ is evaluated using the lowest order drifts of (4.12), [72]. This concludes the analysis of the influence of plasma neutral collisions on the drift-reduced fluid equations. To arrive at the HESEL equations a series of assumptions and arithmetic simplifications are applied. These are covered in the next section.

4.3 Specifications for the HESEL Model

In contradiction to what is claimed by [70], the steps leading from the drift fluid equations (4.15), (4.16), (4.17) and (4.18) to the nHESEL equations do influence the terms arising from plasma neutral interactions. To be able to account for this influence the approximations and manipulations applied to (4.15), (4.16), (4.17) and (4.18) is reviewed in some detail. For detailed calculations of these steps the reader should however refer to some of the original ESEL/HESEL papers, [73], [30].

Domain and Field Geometry

The domain of HESEL is the outboard midplane of a Tokamak. This allows for the use of slab coordinates i.e. rather than toroidal coordinates the problem is expressed in a cartesian coordinate system with x pointing in the radial direction, y pointing in the poloidal direction, and z pointing in the toroidal direction. The Origo is placed such that the axis defined by $x = 0$ corresponds to the LCFS and the axis defined by $y = 0$ intersects the geometrical and magnetic axes¹⁶. The magnetic field is directed along the z -axis with a magnitude given by

$$B(x) = \frac{RB_t}{R + a + x}, \quad B(0) = B_0 = \frac{RB_t}{R + a}, \quad (4.19)$$

where B_t is the toroidal magnetic field at the magnetic axis and R and a are the major and minor torus radii. B_0 is the magnetic field at the LCFS and is hence subscripted with 0. This amounts to assuming a vacuum magnetic field where the partial cancellation of the magnetic field from the diamagnetic current is neglected.

Thin Layer Approximation and Similar Approximations

The thin layer approximation neglects particle density variations in the polarization flux entering the vorticity equation. Utilizing gyro viscous cancellation and neglecting magnetic field inhomogeneity this assumption amounts to:

$$\nabla \cdot (n[\mathbf{u}_{p,i} + \mathbf{u}_{\pi*,i}]) \approx -\frac{n_0}{\Omega_{i0}} \nabla \cdot (d_0^t \nabla_{\perp} \phi^*) \quad (4.20)$$

where n_0 is the reference density, $\mathbf{u}_{\pi*,i}$ is the gyro viscous drift and Ω_{i0} is the ion gyro frequency evaluated at reference temperature, T_{i0} , and reference magnetic field, B_0 . Furthermore, we have introduced

$$\phi^* = \frac{\phi}{B_0} + \frac{p_i}{q_i n_0 B_0} \quad \text{and} \quad d_0^t = \frac{\partial}{\partial t} + \mathbf{u}_{E0} \cdot \nabla, \quad (4.21)$$

where ϕ^* is referred to as generalized potential and d_0^t is the advective derivative with the $\mathbf{E} \times \mathbf{B}$ -drift evaluated at B_0 . Effectively the lowest order drift going into the polarization drift has thus been approximated as

$$\mathbf{u}_{\perp,0} \approx \hat{\mathbf{b}} \times \nabla_{\perp} \phi^*. \quad (4.22)$$

Do note that the thin layer approximation is debatable when modeling edge plasma primarily, due to the large density variations over the simulation domain.

¹⁶See figure 1.1

The approximation of the lowest order perpendicular drift given in (4.22), is also used when evaluating the collisional part of the viscous stress tensor in the vorticity equation and the ion pressure equation. Similar to the approximation of (4.20), the density is taken to be equal to n_0 when evaluating the divergence of the collisional viscous drift flux in the vorticity equation. With these approximations, it becomes clear that the term $\nabla \cdot (n\mathbf{u}_{\pi,i})$ in the ion continuity equation gives rise to diffusion of the generalized vorticity, $\nabla_{\perp}^2 \phi^*$. This diffusion results in a heating term exactly accounted for by the viscous work term $p_i \nabla \cdot \mathbf{u}_{\pi^c}$ - an elegant feature of the HESEL model. Finally it is shown in [30] that the viscous pressure flux $\nabla \cdot (p_i \mathbf{u}_{\pi,i})$ can be neglected.

In the ion and electron pressure equations the diamagnetic drift contribution to $\nabla \cdot \mathbf{q}$ is canceled by the terms depending on diamagnetic advection, entering through the polarization drift, such that diamagnetic advection is not present in the pressure equations. This arithmetic feature is formally known as **diamagnetic cancellation**. Finally, (4.22) is used in the evaluation of the divergence of the polarization drift in the ion pressure equation.

Approximations to Perpendicular Diffusion

The perpendicular diffusion is due to a random walk-like process mediated by electron-ion collisions and has a diffusion coefficient $D_e \propto n/\sqrt{T_e}$. This diffusion coefficient is assumed to be constant in the HESEL model i.e.

$$D_e \approx \nu_{ei0} \rho_{e0}^2, \quad (4.23)$$

where ν_{ei0} is the ion electron collision frequency at reference density, n_0 and temperature T_{e0} . ρ_{e0} is the electron gyro radius at reference temperature T_{e0} and field B_0 . When neglecting thermal force contributions, which partly cancel, the divergence of resistive flux, $\nabla \cdot (nv\mathbf{u}_R)$ in the electron continuity equation is approximated as

$$\nabla \cdot (n\mathbf{u}_R) \approx -D_e(1 + \tau) \nabla_{\perp}^2 n \quad (4.24)$$

where $\tau = T_{i0}/T_{e0}$. Similarly, the resistive drift going into the electron and ion pressure equations is approximated as

$$\mathbf{u}_R \approx -D_e(1 + \tau) \nabla_{\perp} \ln n. \quad (4.25)$$

giving rise to a large number of simplifications similar to that of (4.24).

Approximations to Heat Transport Terms

The heat transport is simplified in a manner similar to that outlined above on the simplification of diffusion from electron-ion collisions. The perpendicular heat conduction coefficient is evaluated at reference temperatures and thus assumed constant. Likewise, the ion collision frequency is assumed constant when evaluating the heat transfer term, ΔQ .

The diffusion coefficients are assumed to be enhanced by neoclassical effects. Neoclassical transport theory accounts for the long distance that charged particles can travel along the magnetic field lines of a toroidal containment device. Remember that this long mean free path is exactly the point on which the conditions of applicability of the Braginskii equations are violated in most fusion plasmas. In a toroidal containment device, the magnetic field has toroidal as well as poloidal components, the ratio of which determines the so-called safety factor usually denoted q . This means that particles traveling along the field lines exhibit a spiral motion. The combination of this spiral motion with guiding center drifts, such as ∇B and curvature drifts can be shown to give rise to an enhanced transport across the field lines [74], [75]. To account for this enhanced transport the diffusion coefficients are multiplied by a common factor

$$D_{e,i} \rightarrow \left(1 + \frac{R}{a} q^2\right) D_{e,i} \quad (4.26)$$

where q is the safety factor. This concludes the approximations made to account for the relation between the perpendicular parts of the drift-reduced Braginskii equations and the HESEL equations.

Parameterization of Parallel Dynamics

In HESEL, parallel dynamics are accounted for by parameterization i.e. the parallel dynamics are not solved in a self-consistent way, as is shown for the perpendicular dynamics above. Instead, the various phenomena giving rise to parallel transport are approximated using other theoretical or empirical results to express them through the macroscopic variables. Due to ballooning the turbulent plasma source mainly resides on the high field side of the LCFS at the outboard midplane [30]. It is thus assumed that all parameterized parallel terms act as sinks. As blobs move into the SOL they expand along the open field lines at velocities comparable to the ion sound speed $c_s = \sqrt{(T_e + T_i)/m_i}$, giving rise to a particle density damping rate approximated by

$$\frac{1}{\tau_n} = \frac{2v_b}{L_b} \quad (4.27)$$

where v_b is the expansion velocity of each end of the blob, and L_b is the typical field-parallel blob length. As vorticity is mainly transported by blobs in the SOL region the damping rate of vorticity is assumed to be equal to that of density,

$$\frac{1}{\tau_w} = \frac{1}{\tau_n}. \quad (4.28)$$

The divergence of the parallel current present in the vorticity equation is approximated by sheath damping, [30, 76],

$$\nabla \cdot (\hat{\mathbf{b}} J_{\parallel}/e) \approx \frac{en_0 c_s}{L_c} \left[1 - \exp \left(\log \sqrt{\frac{m_i}{2\pi m_e}} - \frac{e\phi}{T_e} \right) \right] = \mathcal{S}, \quad (4.29)$$

where L_c is the outer divertor length. Electron heat conduction is assumed to be given solely by Spitzer-Härm conduction, [77], which shall be approximated as

$$\nabla_{\parallel} \cdot \mathbf{q}_{e,T\parallel} \approx -\frac{T_e^{7/2}}{\tau_{SH}}, \quad \text{with} \quad \frac{1}{\tau_{SH}} = 3.16 \frac{n_0}{m_e \nu_{ei0} T_{e0}^{3/2} L_c^2}. \quad (4.30)$$

Parallel heat conduction is neglected for ions as advection is dominant in the SOL [30]. The parallel advection of ion and electron pressure is parameterized through

$$\frac{1}{\tau_{pe}} = \frac{1}{\tau_{pi}} = \frac{9}{2} \frac{1}{\tau_n}. \quad (4.31)$$

These damping rates are derived from the physical conditions of the SOL and should not be applied equally over the full simulation domain. The extent to which these damping rates are applied over the various parts of the domain is determined by a smoothed step function

$$\sigma(x) = \frac{\sigma_s}{2} \left[1 + \tanh \left(\frac{x - x_s}{\delta_s} \right) \right] + \frac{\sigma_w}{2} \left[1 + \tanh \left(\frac{x - x_w}{\delta_s} \right) \right] \quad (4.32)$$

Where σ_i , $i \in \{s, w\}$, are magnitude terms, x_s is the x-position of the LCFS, while x_w indicate the onset of a wall region¹⁷ with increased damping, and δ_s is a smoothness parameter. This concludes the parameterization of parallel dynamics.

4.4 Model equations

In this section, the final manipulations to obtain the HESEL equations are presented. In order to highlight characteristic quantities the transport equa-

¹⁷See figure 5.20

tions are gyro-Bohm normalized through

$$\Omega_{i0}t \rightarrow t, \quad \frac{x}{\rho_{s0}} \rightarrow x, \quad \frac{T_{e,i}}{T_{e0}} \rightarrow T_{e,i}, \quad \frac{e\phi}{T_{e0}} \rightarrow \phi, \quad \frac{n}{n_0} \rightarrow n, \quad \frac{\mathbf{u}}{\rho_{s0}\Omega_{i0}} \rightarrow \mathbf{u}, \quad (4.33)$$

where $\Omega_{i0} = eB_0/m_i$ is the characteristic ion gyro frequency and $\rho_{s0} = \sqrt{\frac{T_{e0}}{m_i\Omega_{i0}^2}}$ is the hybrid ion thermal gyro radius¹⁸. To reduce the equations we explicitly apply slab coordinates which combined with (4.19) can be used to obtain

$$-\left(\nabla f \times \hat{\mathbf{b}}\right) \cdot \nabla \left(\frac{1}{B}\right) = -\frac{1}{B_0(R+a)} \frac{\partial}{\partial y} f \quad (4.34)$$

where f is an arbitrary scalar field. (4.34) makes it natural to introduce the curvature operator, \mathcal{K} given in normalized form as

$$\mathcal{K}(f) = -\frac{\rho_{s0}}{R+a} \frac{\partial}{\partial y} f. \quad (4.35)$$

In this form, the curvature operator only accounts for the radial variation in magnetic field strength and not for the curl of $\hat{\mathbf{b}}$. It can be debated whether a more adequate physical description of edge turbulence would be achieved by including a finite $\nabla \times \hat{\mathbf{b}}$ when calculating (4.34) and (4.35). This is discussed at the end of this chapter. In order for my results to be comparable with other HESEL simulations the current expressions of (4.34) and (4.35) are used in my simulations. To express the positive change in generalized vorticity, $\nabla_{\perp}^2 \phi^*$, a global sign is applied in the vorticity equation of (4.16). One must be aware that this sign also applies to the inelastic drift term entering the vorticity equation when neutrals are included. Furthermore, the vorticity equation is substituted into the ion pressure equation to eliminate the divergences of the polarization and viscous drifts. Once again this influences the way neutral sources are expressed in the model. With these manipulations accounted for the full system of equations revised nHESEL equations, can be presented:

$$\frac{d}{dt}n + n\mathcal{K}(\phi) - \mathcal{K}(p_e) = \Lambda_n + \Sigma_n \quad (4.36)$$

$$\nabla \cdot \left(\frac{d^0}{dt} \nabla_{\perp} \phi^* \right) - \mathcal{K}(p_e + p_i) = \Lambda_w + \Sigma_w \quad (4.37)$$

$$\frac{3}{2} \frac{d}{dt} p_e + \frac{5}{2} p_e \mathcal{K}(\phi) - \frac{5}{2} \mathcal{K} \left(\frac{p_e^2}{n} \right) = \Lambda_{p_e} + \Sigma_{p_e} \quad (4.38)$$

$$\frac{3}{2} \frac{d}{dt} p_i + \frac{5}{2} p_i \mathcal{K}(\phi) + \frac{5}{2} \mathcal{K} \left(\frac{p_i^2}{n} \right) - p_i \mathcal{K}(p_e + p_i) = \Lambda_{p_i} + \Sigma_{p_i} \quad (4.39)$$

¹⁸The use of ρ_{s0} rather than ρ_{i0} is a historical remnant from earlier fusion research where it was typical to assume that ions were cold.

Where the advective derivatives are defined solely through $\mathbf{E} \times \mathbf{B}$ -advection

$$\frac{d}{dt} = \frac{\partial}{\partial t} + B^{-1}\{\phi, \cdot\}, \quad \frac{d^0}{dt} = \frac{\partial}{\partial t} + \{\phi, \cdot\}, \quad (4.40)$$

which has been written using the anti-symmetric bracket

$$\{f, g\} = \frac{\partial f}{\partial x} \frac{\partial g}{\partial y} - \frac{\partial f}{\partial y} \frac{\partial g}{\partial x}. \quad (4.41)$$

Terms related to diffusion and parallel damping are denoted Λ_i , $i \in \{n, w, pe, pi\}$, and are given by

$$\Lambda_n = D_e(1 + \tau)\nabla_{\perp}^2 n - \sigma(x)\frac{n}{\tau_n} \quad (4.42)$$

$$\Lambda_w = \frac{3}{10}D_i\nabla_{\perp}^2 \nabla_{\perp}^2 \phi^* - \sigma(x)\frac{\nabla_{\perp}^2 \phi^*}{\tau_n} + \sigma(x)\mathcal{S}, \quad (4.43)$$

$$\Lambda_{pe} = D_e(1 + \tau)\nabla \cdot (T_e \nabla_{\perp} n) + D_e \frac{11}{12} \nabla \cdot (n \nabla_{\perp} T_e)$$

$$+ D_e(1 + \tau)\nabla_{\perp} \ln n \cdot \nabla_{\perp} p_i \\ - \frac{3m_e}{m_i} \nu_{ei0} (p_e - p_i) - \sigma(x) \left[\frac{9}{2} \frac{p_e}{\tau_n} + \frac{T_e^{7/2}}{\tau_{SH}} \right], \quad (4.44)$$

$$\Lambda_{pi} = \frac{5}{2}D_e(1 + \tau)\nabla \cdot (T_i \nabla_{\perp} n) - D_e(1 + \tau)\nabla_{\perp} \ln n \cdot \nabla_{\perp} p_i \\ + 2D_i \nabla \cdot (n \nabla_{\perp} T_i) \frac{3}{10}D_i \left[(\partial_{xx}^2 \phi^* - \partial_{yy}^2 \phi^*)^2 + 4(\partial_{xy}^2 \phi^*)^2 \right] \\ + \frac{3m_e}{m_i} \nu_{ei0} (p_e - p_i) + \sigma(x) \left(p_i \mathcal{S} - \frac{9}{2} \frac{p_i}{\tau_n} \right). \quad (4.45)$$

The terms entering the equations due to plasma-neutral interactions are given by

$$\Sigma_n = I^{(1)} \quad (4.46)$$

$$\Sigma_w = \nabla \cdot (n \mathbf{u}_{I,i}) \quad (4.47)$$

$$\Sigma_{pe} = I_e^{(\frac{1}{2}mv^2)} \quad (4.48)$$

$$\Sigma_{pi} = I_i^{(\frac{1}{2}mv^2)} - \mathbf{u}_{i\perp,0} \cdot \mathbf{I}_i^{(mv)} + \frac{1}{2} u_{i\perp,0}^2 I^{(1)} \\ + p_i \nabla \cdot (n \mathbf{u}_{I,i}) - p_i \nabla \cdot (\mathbf{u}_{I,i}) - \frac{3}{2} \nabla \cdot (p_i \mathbf{u}_{I,i}), \quad (4.49)$$

where $\mathbf{u}_{I,i} = \mathbf{u}_{IR,i} + \mathbf{u}_{In,i}$. Be aware that (4.46)-(4.49) are written in normalized units. Similar expressions were provided by [70] but with errors in the expressions for Σ_w and Σ_{pi} . In that sense (4.46)-(4.49) is a new contribution to the literature. In the next chapter the PISAM model is presented. PISAM serves to calculate $I^{(1)}$, $\mathbf{I}_i^{(mv)}$, $I_i^{(\frac{1}{2}mv^2)}$ and $I_e^{(\frac{1}{2}mv^2)}$ and thus provides the final closure of the nHESEL equations. The combined model, where PISAM is used to close the nHESEL equations, shall be called PISAM-HESEL.

4.5 Dimensionality of HESEL

The primary reason that HESEL is referred to as a 2D model is that the toroidal axis is truncated due to an assumption of symmetry. The result is not, as the term 2D might imply, that the parallel velocity is not accounted for, but rather, that the field-aligned velocity is not self-consistently incorporated. Instead, it is parameterized and enters the equations as damping terms. Furthermore one may point out that the fluid closure on which HESEL is based is conducted using full 3D approximations for the phase space distribution function i.e. the particles of which the plasma consists shall certainly be thought of as moving in three-dimensional space. In consistency with this observation, PISAM has to be implemented as a full 3D model.

As mentioned, the foundation of the interchange dynamics is a vertical current created by the charge dependent $\nabla\mathbf{B}$ - and curvature drifts. These are both derived consequences of the 3D toroidal geometry. As given by (1.17) these drifts contribute equally to the vertical current in a vacuum field. In HESEL however, only the contribution from one of these drifts is included. In this light, it seems that the turbulence predicted by HESEL is underestimated. On the other hand, the fact that HESEL is 2D permits cancellation of the vertical current produced by $\nabla\mathbf{B}$ - and curvature drifts. This means that no stable equilibrium solutions to the HESEL equations exist, as nothing can prevent interchange instability. In conclusion, the HESEL equations might not resemble physical reality any closer if the seemingly correct factor of 2 is added to (4.34) and (4.35).

5 PISAM

This chapter introduces all the possible types of inelastic collisions between plasma and neutral particles included in PISAM. Great effort has been put into the detailed argumentation regarding the choice of included reaction channels, given in this chapter. As part of presenting the chemical reactions, the momentum and energy exchange of each single reaction channel is evaluated, when necessary. Furthermore, the velocities of neutral fragments resulting from the relevant inelastic collisions are provided. The development of PISAM is somewhat iterative as simulation data from early PISAM versions have been used to develop the current model. This method is especially helpful in the determination of the exact source terms produced in each reaction. The simulation referred to in the rest of this chapter uses non-interacting neutrals with dynamic plasma frames from a simulation of nHESEL performed by Thrysøe, [70]. The reference quantities at the LCFS of this simulation are

$$n_0 = 3 \cdot 10^{19} \text{ m}^{-3} \quad T_{e,0} = T_{i,0} = 40 \text{ eV} \quad B_0 = 2 \text{ T}, \quad (5.1)$$

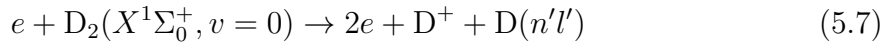
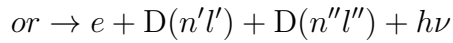
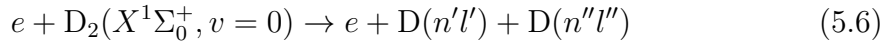
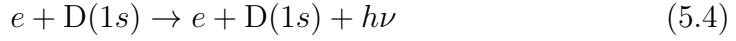
such that the time and length scales are set by

$$\Omega_{i0} = 9.59 \cdot 10^7 \text{ s}^{-1}, \quad \rho_{s0} = 6.5 \cdot 10^{-4} \text{ m}. \quad (5.2)$$

These values are chosen such as to be in correspondence with typical values of medium-sized Tokamaks, [78, 79], and not for the specific PISAM-HESEL simulations of this report, which are conducted at lower density and magnetic field, as will be presented in chapter 8. As discussed in chapter 7 the time step used for PISAM is Ω_{i0}^{-1} . In this simulation, $2.5 \cdot 10^{10}$ super-particles are injected in the domain each second yielding approximately $4 \cdot 10^5$ and $1 \cdot 10^5$ super-molecules and -atoms in the domain at saturation, which is sufficient for the statistics of the current chapter, but a very low resolution compared to that used in PISAM-HESEL simulations.

5.1 Overview of Reaction Channels

Five types of reactions are included in this model, three for atoms and two for molecules. These are summarized schematically as



Where the first three are reactions for the ground state of the deuterium atom and the last two are reactions for the electronic and vibrational ground state of the deuterium molecule. The primes in (5.7) should be read for the individual reactions, and not across reactions. The following sections are concerned with the physical details of each of these reactions as well as the decisions made to implement them numerically. As most data is available for 1H atoms and 1H_2 molecules, it is in many situations necessary to apply data from experiments on hydrogen rather than deuterium. Whenever this is the case it is explicitly stated in the following by use of the word hydrogen. All reactions shall, however, be written for deuterium reflecting the physical situation described.

5.2 Atoms

Figure 5.1 gives an overview of the reactions between plasma particles and deuterium atoms included in PISAM. This section is concerned with the details of each of these reactions, and the reasons for including them.

Excitation and Ionization of the Deuterium Atom

A plot of various excitation rates as well as the single-step ionization rate for the ground state (1s) of the hydrogen atom is shown in figure 5.2. Since the electronic states are practically identical for hydrogen and deuterium [80], only minor deviations from the true reaction rates of the deuterium atom are

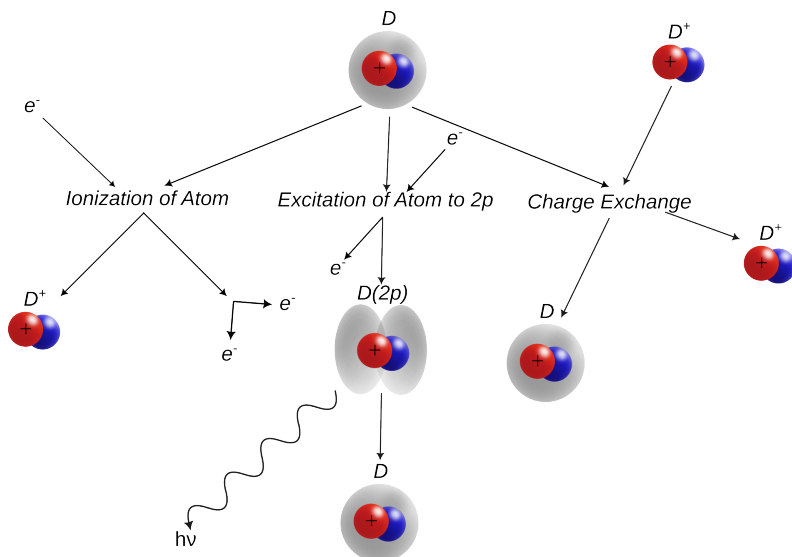
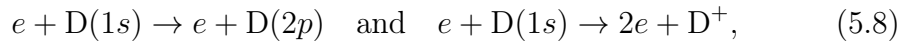


Figure 5.1: An overview of the reactions of deuterium atoms with plasma particles included in PISAM. The orbitals are merely added to illustrate the difference in electronic states and do not necessarily match the physical orbitals.

expected. As evident from figure 5.2 the two reactions most frequently caused by electron impact on deuterium atoms in the ground state are



where the first is an excitation to the (2p) state and the second is a one-step ionization.

Excitation to D(2p)

It is clear from the high reaction rate of the (2p) excitation channel that the (2p) state is strongly coupled to the ground state. This strong coupling also results in the (2p) state having a lifetime of only 1.6ns [81], which, as we shall see, is shorter than or comparable to the time step of PISAM. Due to this short lifetime, it shall be assumed that the (2p) state decays instantaneously, such that this excitation merely results in a sink of electron energy.

Ionization of D(1s)

Even though the excitation rates to the (2s) state and (3n) states shown in figure 5.2 are low in comparison to the reactions of (5.8), they do affect the ionization rate slightly, due to multi-step ionization processes. Furthermore, D(2s) atoms are created by certain dissociative processes of the deuterium molecule, and a short account of its behavior at relevant conditions is thus presented here. Unlike the (2p) state, the (2s) state is weakly coupled to the

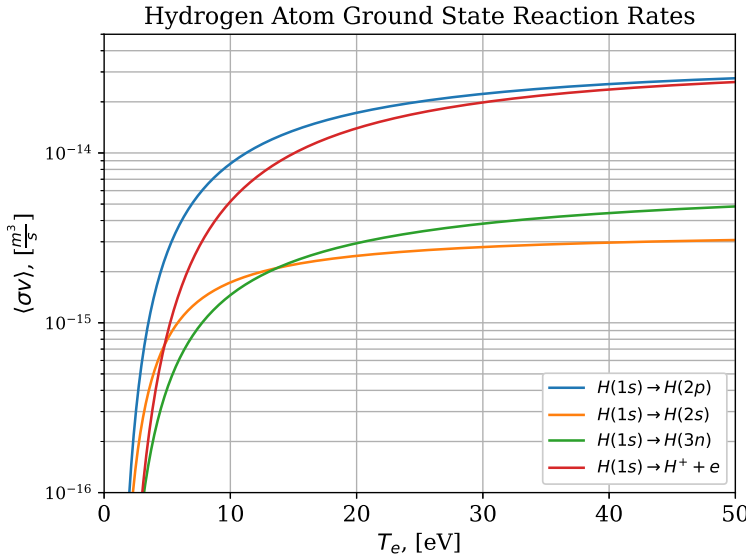


Figure 5.2: Excitation and ionization rates for the ground state ($1s$) of the hydrogen atom. The ionization rates plotted here represent the rate of single-step ionization. This plot is based on analytical fits provided by [82] and [83].

ground state making it metastable with a lifetime of $\approx 2\text{ms}$, [84]. However, due to the very low fine structure energy difference between the ($2s$) and ($2p$) states, the reaction rate for excitation of D($2s$) to D($2p$) by electron impact is relatively high, especially at low temperatures. The rates of the dominant reaction channels of D($2s$) by electron impact are shown in figure 5.3. At SOL relevant temperatures the reaction rate of $e + D(2s) \rightarrow e + D(2p)$ is around $3 \cdot 10^{-12} \frac{\text{m}^3}{\text{s}}$. At a typical density of $n_e = 10^{19} \text{1/m}^3$ this gives a lifetime of $\sim 30\text{ns}$. Due to this short lifetime, transport of the ($2s$) state shall not be included in the model. When deuterium atoms in the $2s$ state are created by molecular dissociation¹⁹ it is assumed that they decay to the ground state instantaneously, thus neglecting the fact that such a D($2s$) atom might be further excited rather than decay, see figure 5.3.

Excitation into the ($2s$) state or higher excited states may result in ionization rather than decay back into the ground state. As the most common intermediate states have relatively short lifetimes in the approximate range ($10 - 500$)ns [85], the rate of such multi-step ionization processes depends strongly on the plasma density. A double polynomial fit parameterized in electron temperature and density is provided in [82], and plotted in figure 5.4. At SOL relevant temperature and density the effective ionization rate differs from the single-step ionization rate by around 25 %, which is a considerable

¹⁹The process of molecular dissociation is described later in this chapter.

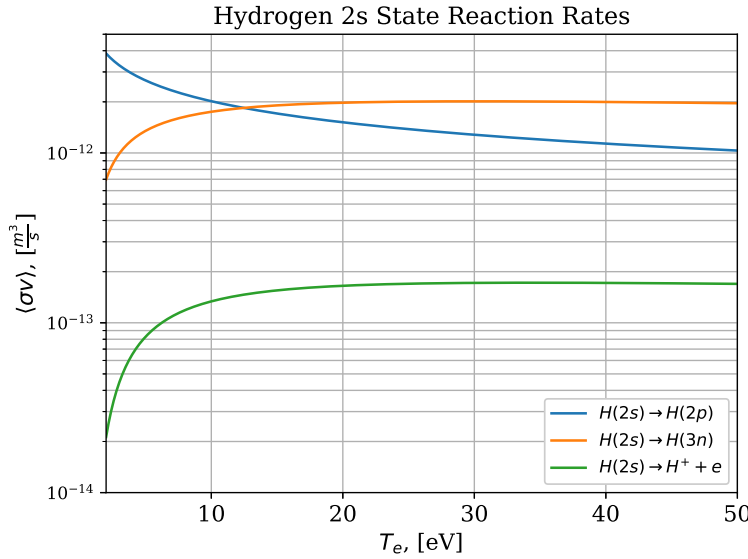


Figure 5.3: Excitation and ionization rates for the metastable (2s) state of the hydrogen atom. The ionization rate plotted here represents the rate of single-step ionizations. This plot is based on analytical fits provided by [82] and [83].

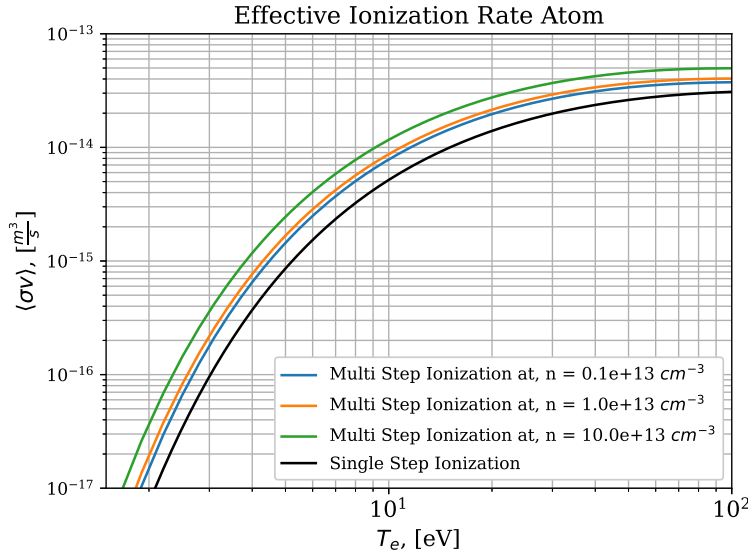


Figure 5.4: Effective reaction rates for ionization of the hydrogen atom in the ground state as a function of electron density and temperature. The black line gives the rate of single-step ionization, solely as a function of electron temperature. This plot is based on analytical fits provided by [82], based on [86].

amount. The rates of figure 5.4 are used as the ionization rates for atoms in PISAM. For simplicity and to minimize computations, the energy loss from electrons due to excitation to an excited state followed by radiative decay back to the ground state is only included for D(2p) as the intermediate state. The energy of the produced photons is assumed to be lost from the system.

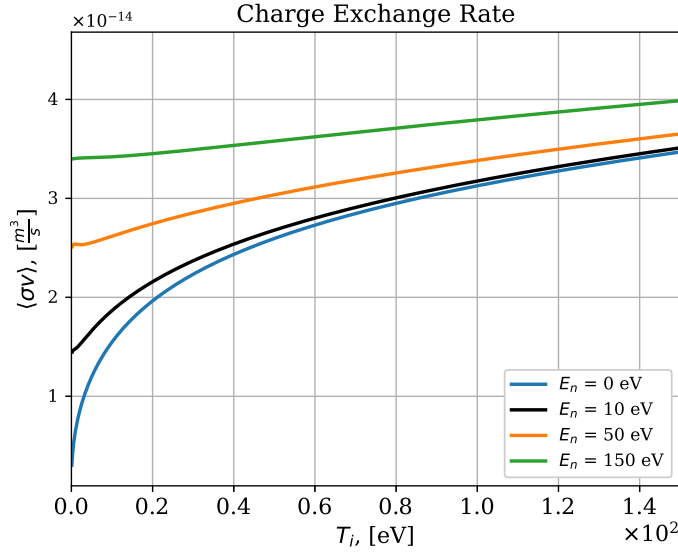
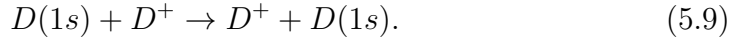


Figure 5.5: Charge exchange rate for the ground state of a deuterium atom with various energies E_n . This plot is based on an analytical fit provided by the database HYDHEL, [83], scaled for the mass of deuterium ions using the scaling of (3.13).

Charge Exchange of Deuterium Atoms and Deuterium Ions

The charge exchange (CX) reaction between a deuterium atom in its ground state and a deuterium ion can be expressed as



It shall be assumed that the velocities of the ion and neutral particle going into CX are simply switched, which is also the assumption used in highly detailed neutral codes such as EIRENE [87]. This implies that the velocity distribution of ions going into the reaction is also the velocity distribution of neutrals going out of the reaction and vice versa. It should be noted that this treatment is not strictly momentum- and energy-conserving due to the mass difference of the reactants of one electron mass. The approximation is however good due to the large mass ratio, $m_i/m_e \approx 3.7 \cdot 10^3$, for deuterium atoms. CX is the only collision between two heavy particles included in the model. Since the particles going into the reaction have similar masses and energies one cannot assume that the neutral particle is at rest, as has been done for electron-neutral collisions. The reaction rate is thus a function of ion temperature as well as the energy of the relevant deuterium atom. Figure 5.5 shows the reaction rate for CX at SOL relevant temperatures and various deuterium atom energies.

Implementation

To get the correct distribution of the neutral atoms created in CX reactions, and to supply the correct source terms to the plasma fluid equations, the break of spherical symmetry in CX reactions, due to the comparable velocities of ions and atoms must be accounted for. This demands an evaluation of the integrand in (3.11). The relative magnitude of the integrand gives the distribution of the speed and the angle, θ' ²⁰, of ions going into CX reactions. This distribution is a function of ion temperature and the energy of the neutral in the rest frame of the ions. The new neutral speed and angle θ' resulting from a specific CX reaction are obtained by sampling from the distribution specific to the temperature and neutral energy relevant to the reaction. The azimuthal angle, ϕ' , in the neutral frame, is obtained from uniform sampling over the range $[0, 2\pi]$. Knowing the random speed of the ion going into the CX reactions the angles θ' and ϕ' fully define the random velocity of the new neutral particle in the d-frame of figure 3.1. This velocity is finally transformed into the coordinates of the lab frame using (3.6) and (3.7), and added to the fluid velocity of the ions. The velocity of the deuterium ion created in the CX reaction is simply the velocity of the incoming deuterium atom which is known to PISAM prior to the collision. With the incoming and outgoing velocities completely determined the momentum- and energy exchange is easily evaluated.

As calculating the contributions from a velocity range $\mathbf{w}_i, d\mathbf{w}_i$ to $\langle \sigma_{cx} g \rangle$ for a certain relative neutral energy E_d and at a certain ion temperature T_i in each individual CX reaction would add a large computational overhead, a table where the contributions are already calculated is loaded into PISAM at initialization. The procedure for creating this 4D table is as follows:

- Make appropriate ranges and resolutions of the ion temperature T_i and relative neutral energy E_d . In the implementation of PISAM these are sampled logarithmically since the contributions vary the most for low relative velocities. Furthermore, decide on a resolution of the angle θ' that runs from 0 to π .
- Calculate the range of relative neutral velocities, d , corresponding to the range of E_d .
- For each temperature make an appropriate range of random velocities w_i . I have chosen this velocity range to run from zero up to 3 times the

²⁰See figure 3.1.

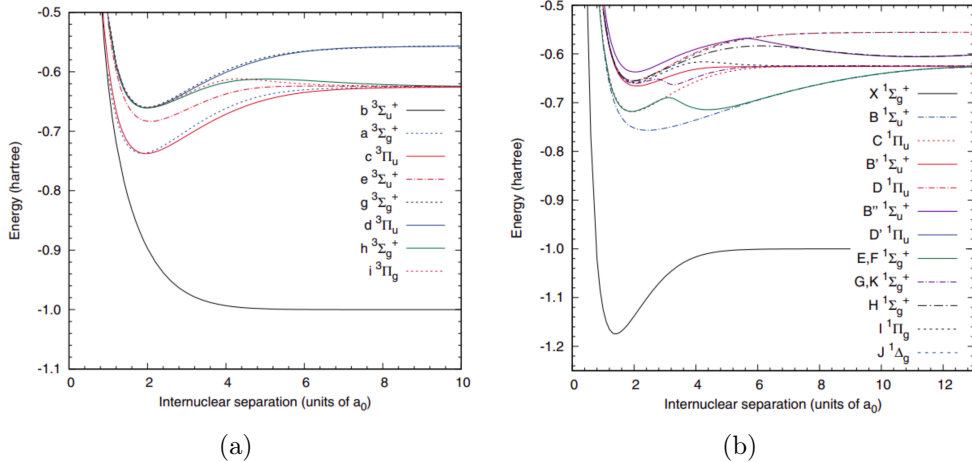


Figure 5.6: Energy potentials of low lying electronic states of molecular hydrogen in atomic units. (a) The first eight triplet states of H_2 calculated by Staszewska and Wolniewicz [88] (b) The ground state and eleven of the low-lying excited singlet states of H_2 , based on [89–94]. These figures were published in [95].

thermal velocity $v_{t,i} = \sqrt{2T_i/m_i}$. The velocity range thus depends on T_i , such that "wasting" resolution on calculating the contribution from velocities that are completely suppressed by the $\exp\left(-\frac{mw^2}{2T}\right)$ dependency in the Maxwell-Boltzmann distribution is avoided.

- With the ranges of θ' , w_i and d at hand make 3D meshgrids corresponding to any possible combination of θ' , w_i and d within the given ranges. Use these to make a similar grid of the relative speeds according to (3.10).
- Using the polynomial fit for the CX cross section given in [82], evaluate the cross section at the relevant speeds. Finally, the integrand of (3.11) can be evaluated, such that for each temperature T_i a 3D grid holding the contributions from all possible combinations of the values in the ranges E_d , w_i , θ is produced.

Validation of the results leading to the 4D CX reaction rate distribution table is given in appendix 5.2. This appendix includes plots quantifying the spatial asymmetry in CX reactions, as well as the discrepancy between the Maxwell-Boltzmann speed distribution, and the speed distribution of ions going into charge exchange reactions. To sample from the 2D distributions defined for each combination of T_i and E_d , the following procedure is applied:

- Let the 2D distribution be denoted by D , where the velocities vary over the 0'th axis and the θ 's over the 1'st axis. Sum all the values of D along

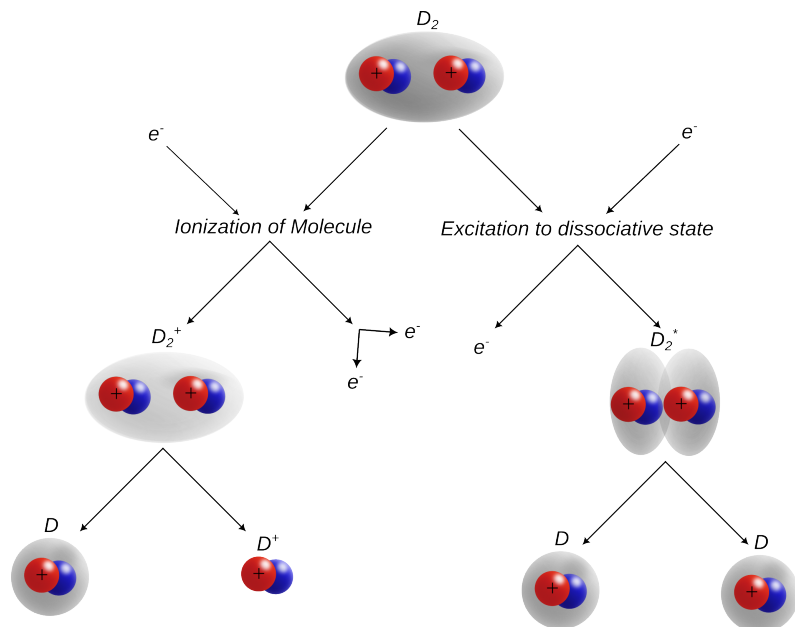


Figure 5.7: An overview of the reactions of deuterium molecules with plasma particles included in PISAM. The orbitals are merely added to illustrate the difference in electronic states and do not necessarily match the physical orbitals.

the velocity axis, to get the 1D marginal distribution with respect to θ' .

- Calculate the cumulative sum of the marginal distribution with respect to θ' and denote this 1D-array by A .
- Create a uniformly distributed random number r between zero and the last (and largest) element in A and calculate the index, i , of A holding the largest value smaller than r .
- To get the sampled value for θ' a linear interpolation is made by setting $\theta' = d\theta' \cdot i + d\theta' \cdot (A[i + 1] - A[i]) / (r - A[i])$, where $d\theta'$ is the resolution with which the table is sampled along the θ' -axis.
- Now retrieve the conditional distribution given the θ' you just calculated i.e. $D[:, i]$.
- Use the same technique for sampling a single variable distribution as the one just applied to sample θ , to get the sampled value of w'_i .

5.3 Molecules

An overview of the potentials of the electronic states of molecular hydrogen relevant to the following discussion is presented in figure 5.6. Figure 5.7 illustrates the reactions between plasma particles and deuterium molecules

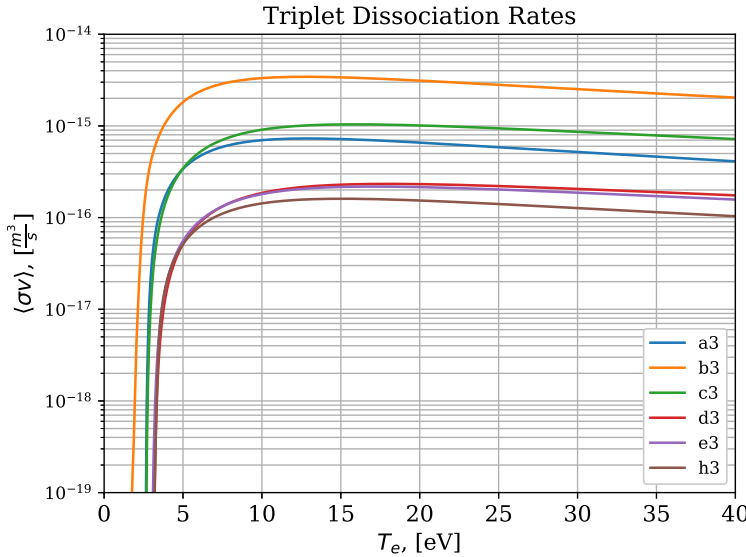


Figure 5.8: Reaction rates for dissociation through triplet channels, due to excitation by electron impact on the ground state $D_2(X^1\Sigma_g^+, v = 0)$ of the neutral deuterium molecule. The x-axis shows electron temperature. The excitation cross sections are collected from the database [98]. All excited triplet states eventually dissociate through $b^3\Sigma_u^+$, due to fast decay rates to this repulsive state.

included in PISAM. This section is concerned with the chemical rates and kinematic details of each of these reactions.

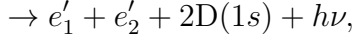
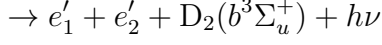
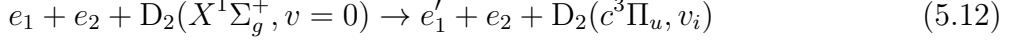
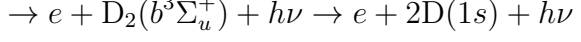
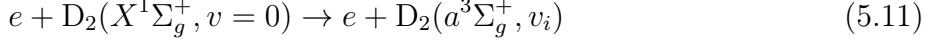
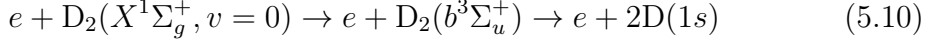
Molecular Dissociation Into Neutral Fragments (MD)

Dissociation of D_2 can proceed through a large number of channels, all of which are dependent on electronic excitation processes. These channels can be separated into the categories of excitation to triplet and singlet states of the deuterium molecule. These two categories dissociate by fundamentally different processes. The excited triplet states dissociate through the repulsive $D_2(b^3\Sigma_u^+)$ state, whereas the dissociation through singlet states is caused by excitation or decay into the vibrational continuum of an electronic state possessing bound vibrational states. The former generally give rise to neutral fragments with energy in the order of a few eV [96, 97], while the latter yields cold fragments with typical energies of $0.15 - 0.3$ eV as argued below.

Dissociation Through Triplet States

Figure 5.8 shows the rate of dissociation through the most frequent triplet channels. Based on the reaction rates and the fact that the electron energy loss is similar in magnitude for all relevant triplet excitations, only the three most frequent channels are included in the model, for simplicity. The channels

of dissociation through triplet states included in the present kinetic neutral model can be schematically represented as:



where the subscripts and primes in the last reaction are added to indicate that two different electrons are responsible for the two excitations happening at two different times.

Direct Excitation to $b^3\Sigma_u^+$

(5.10) shows the excitation into the repulsive $b^3\Sigma_u^+$ state, leading to immediate dissociation. The excitation energy from the ground state at its most probable inter-nuclear separation of $R_0 = 1.40a_0$ is 10.62eV [99], which shall be used as the electron energy loss for reactions through this channel. The average temperature of dissociation through triplet channels found in the current simulation is 13.2eV. According to the calculations presented in [96] the most probable value of the kinetic fragment energy at around 13eV is approximately 2.75eV, which is applied in PISAM.

Dissociation Through $a^3\Sigma_g^+$ and $c^3\Pi_u$

The $a^3\Sigma_g^+$ state is radiatively coupled to the $b^3\Sigma_u^+$ state with a transition frequency of a lifetime of $\sim 10\text{ns}$, [80]. Due to this short lifetime, the decay shall be assumed to be instantaneous. (5.12) shows the more complicated channel of dissociation proceeding through the $c^3\Pi_u$ state. $c^3\Pi_u$ is coupled to the ground $X^1\Sigma_g^+$ state by weak magnetic dipole and electric quadrupole interactions making it metastable with a lifetime of $\sim 1\text{ ms}$, [80]. However, due to the small energy difference of $\Delta E_{00} = 0.017\text{ eV}$ between $(c^3\Pi_u, v = 0)$ and $(a^3\Sigma_g^+, v = 0)$, electron impact excitation of $(a^3\Sigma_g^+, v = 0)$ from $(c^3\Pi_u, v = 0)$ is expected to be large, [80]. The results of a theoretical calculation of the

cross section for this transition were presented in [100] based on the distorted wave approximation, and later fitted to the analytical expression, [80],

$$\sigma_{exc}(c^3\Pi_u, v = 0 \rightarrow a^3\Sigma_g^+, v' = 0) = \frac{2.08}{x^{1.20}} \left(1 - \frac{1}{x}\right)^{3.80} \cdot 10^{-15} \text{m}^2 \quad (5.13)$$

The rate as a function of electron temperature is obtained by integration over a Maxwellian distribution as given by (3.4). [80] gives an approximate method for calculating the cross section of transitions with $v = 0$ and $v' > 0$. As these fall off rapidly with increasing v' they shall be omitted in the following estimate. To properly apply (5.13) to provide an estimate for the lifetime of $c^3\Pi_u$ at the relevant plasma conditions further assumptions are needed since [80] only reports the cross section for transitions from the vibrational ground state of $c^3\Pi_u$ i.e. $v = 0$. As can be seen from figure 5.9, giving the cross section of excitation to $(c^3\Pi_u, v)$ from $(X^1\Sigma_g^+, v = 0)$, only a relatively small portion of molecules will inhabit the $v = 0$ vibrational state of $c^3\Pi_u$ relative to other excited states. I shall assume here that the cross section of excitations of the type $(c^3\Pi_u, v) \rightarrow (a^3\Sigma_g^+, v' = v)$ will be similar in magnitude to that obtained from (5.13) as the energy difference between these states is similar. It is thus assumed that the reaction rate of decay from any vibrational state of $c^3\Pi_u$ into $a^3\Sigma_g^+$ is the same as that found from integration of (5.13) over the electron velocity distribution. This is expected to be a conservative estimate for a number of reasons:

- Only transitions for which $v = v'$ are considered.
- Besides electron impact excitation of $a^3\Sigma_g^+$ from $c^3\Pi_u$, vibrational states of $c^3\Pi_u$ with $v > 0$ are expected to have a finite probability of predissociation into lower lying vibrational states of $a^3\Sigma_g^+$. As I have not been able to find any estimates of this cross section it is omitted when estimating the reaction rate of $c^3\Pi_u$.
- From the two theoretical methods applied for calculating $\sigma_{exc}(c^3\Pi_u, v = 0 \rightarrow a^3\Sigma_g^+, v' = 0)$, the distorted wave approximation gives the lower cross section of the two.

The excitations to $c^3\Pi_u$ from $(X^1\Sigma_g^+, v = 0)$ have been monitored in the simulation at the beginning of this chapter. The average temperature and density of excitations from $D_2(X^1\Sigma_g^+, v = 0)$ to $c^3\Pi_u$ was found to be 24.4eV and $2.1 \cdot 10^{19} \text{m}^3$ respectively. After integration (5.13) yields a reaction rate of approximately $1.2 \cdot 10^{-12} \frac{\text{m}^3}{\text{s}}$ at 24.4eV, giving a lifetime of the $c^3\Pi_u$ -state of around 40ns at relevant densities. Due to this relatively short lifetime,

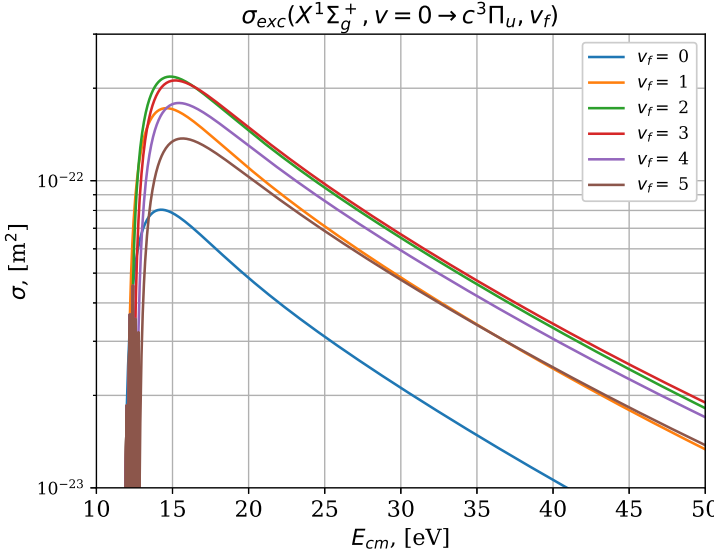


Figure 5.9: Cross sections for the transition $(X^1\Sigma_g^+, v = 0) \rightarrow (c^3\Pi_u, v_f)$ provided by [98], for the 5 lowest vibrational states.

the decay of $c^3\Pi_u$ to $a^3\Sigma_g^+$ and thus to $b^3\Sigma_u^+$ shall be assumed instantaneous. Furthermore, due to the very small energy difference between $a^3\Sigma_g^+$ and $c^3\Pi_u$ their rates are simply added in PISAM, treating them as one reaction to reduce the number of rates computed in each time step.

The excitation energy of these two triplet states is set to the average excitation energy of the $a^3\Sigma_g^+$ state and $c^3\Pi_u$ state as their excitation cross sections are very similar. Based on [101] and [102] this energy is determined to be 12.64eV, thus giving the electron energy loss.

The inter-nuclear separation of the $a^3\Sigma_g^+$ state corresponding to the lowest potential energy of this state is around $2.2a_0$, [95]. At this separation, the potential energy of the $b^3\Sigma_u^+$ state is significantly lower than for typical ground state nuclei separation distances. The kinetic energy of the neutral fragments is thus also expected to be lower, which is indeed the case as shown in [97], giving the distribution of fragment energies for decays from $(a^3\Sigma_g^+, v)$ to $(b^3\Sigma_u^+)$. Figure 5.10 gives the probability distribution of the electron impact energy of electrons giving rise to excitation to $a^3\Sigma_g^+$ and $c^3\Pi_u$. Weighing these energies by their probability gives an average of around 20eV. The cross sections of excitation to the different vibrational states of $a^3\Sigma_g^+$ and $c^3\Pi_u$ from $D_2(X^1\Sigma_g^+)$ are provided by [98]. These cross sections are evaluated at 20eV to get an estimate of how the vibrational states of these excited electronic states are distributed. As accounted for above, I shall assume that the transition from $c^3\Pi_u$ to $a^3\Sigma_g^+$ conserves the vibrational quantum number. The effective distribution of vibrational states in $a^3\Sigma_g^+$ is thus given as the average

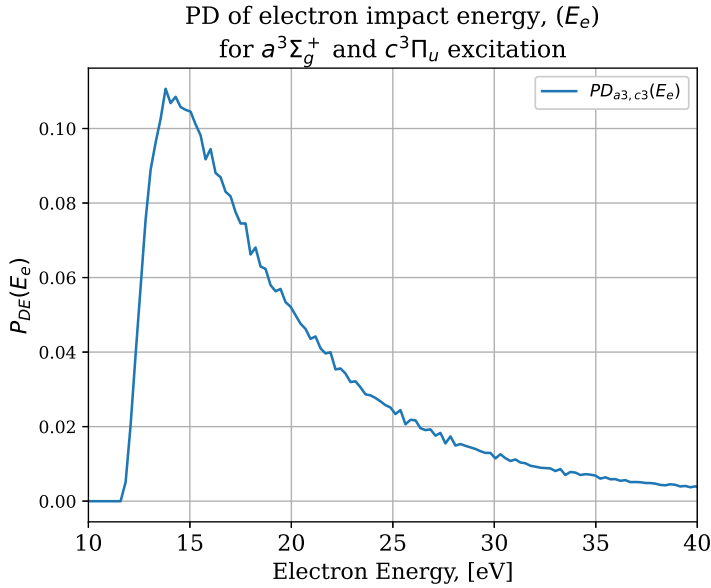


Figure 5.10: The probability distribution of the electron impact energy of electrons giving rise to excitation of $a^3\Sigma_g^+$ and $c^3\Pi_u$. The data shown in this plot results from a simulation of PISAM on dynamic fields representative of plasma edge conditions.

of the distributions of the vibrational states in the excited electronic states $c^3\Pi_u$ and $a^3\Sigma_g^+$, when excited from the ground state ($X^1\Sigma_g^+, v = 0$). This effective distribution is used to weigh the fragment energy distributions of [97]. Averaging this final distribution yields an estimate of the fragment energy of 0.75eV, which shall is applied in PISAM.

Dissociation Through Singlet States

The rates of the most frequent singlet channels are shown in figure 5.11. Due to its low reaction rate the *EF1* channel is not included in the model. The rate of the *C1* channel is also very low and could be omitted. The energy transfer characteristics of this channel are however so close to that of the *B1* channel that they can be considered as one reaction. It is thus computationally "free" to include it. Channels for dissociation through singlet states included PISAM

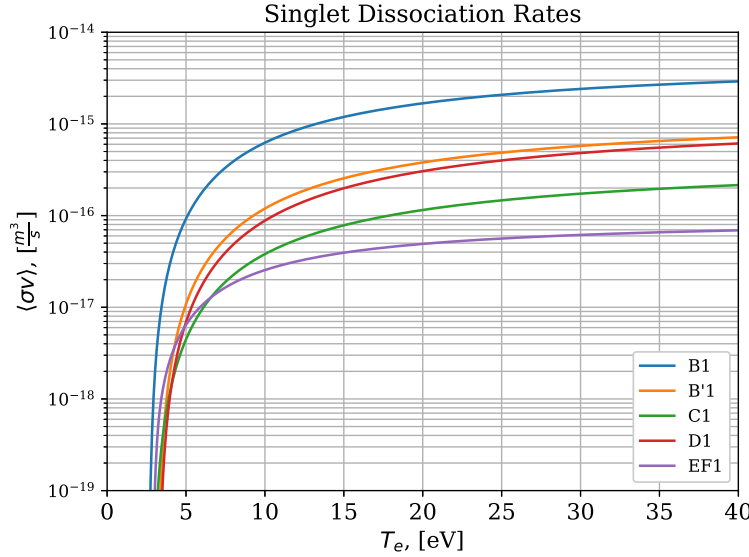
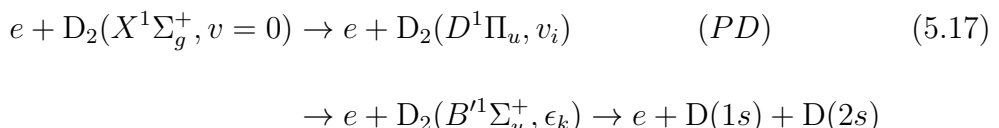
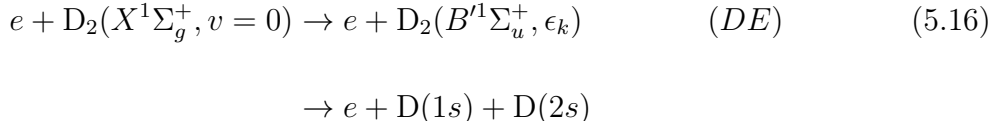
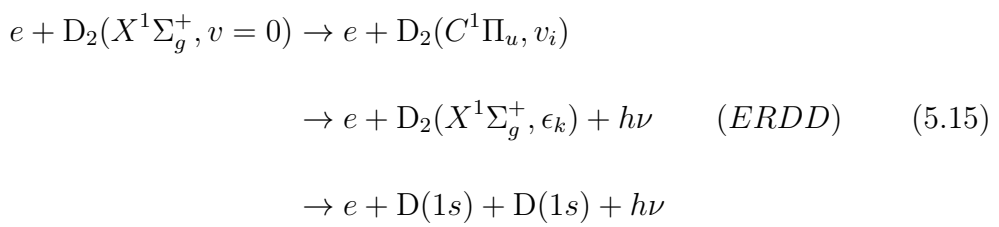
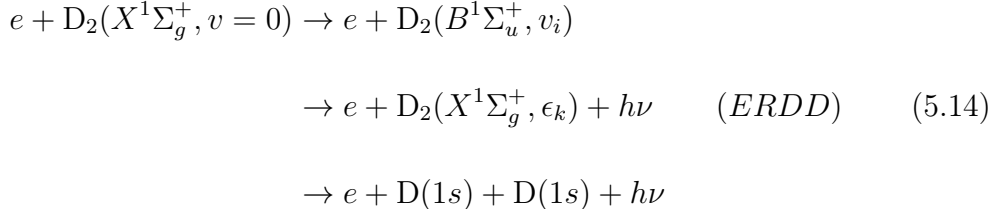


Figure 5.11: Reaction rates for dissociation through singlet channels, due to excitation by electron impact on the ground state $D_2(X^1\Sigma_g^+, v = 0)$ of the neutral deuterium molecule. The x-axis shows electron temperature. The excitation cross sections are collected from the database [98], and the dissociation fractions of each excitation are obtained from [95].

can be summarized schematically as:



Where ϵ_k is the continuum energy of unbound vibrational states. The energy of the fragments of a dissociation resulting from such an unbound continuum

state is $\epsilon_k/2$, for homonuclear diatomic molecules. The important singlet dissociation channels, at SOL relevant conditions, can be split into two sub-categories: Dissociative excitation (DE) where the ground state is directly excited into the vibrational continuum of an excited electronic state, or excitation to a bound vibrational state of an excited electronic state, that decays to the vibrational continuum of a lower lying state. The latter can be further subdivided into two subclasses: Excitation radiative decay dissociation (ERDD) where the decay into the continuum of a lower-lying state causes photon emission, and predissociation (PD) where this decay happens without emission of radiation. Common for the dissociation channels through singlet states is that not all excitations lead to dissociation. The fractions of excitations to various singlet states caused by electron impact on ($X^1\Sigma_g^+, v = 0$), that eventually lead to dissociation are given in [95]. These fractions were used alongside the accurate excitation cross sections of [98] to produce figure 5.11 by integration over the Maxwellian electron velocity distribution.

Dissociation Through $B'^1\Sigma_u^+$ and $D^1\Pi_u$

As we are only considering the vibrational ground state of the electronic ground state of D₂ the only relevant channel for DE is (5.16) through $B'^1\Sigma_u^+$ [80, 103, 104]. As indicated in (5.17) the PD channel is initialized by excitation of the $D^1\Pi_u$ state that dissociates due to non-radiative decay to the $B'^1\Sigma_u^+$ state, and thus produces the same neutral fragments i.e. D(1s) and D(2s). As argued by [105] the main contributors to the production of the metastable D(2s) by electron impact on ($X^1\Sigma_g^+, v = 0$) are exactly the channels (5.16) and (5.17). Experimental measurements of these metastable atoms are presented in [105] and report an energy of approximately 0.3eV. PISAM thus assumes that in the CM-frame of electron molecule collisions the channels for dissociation (5.16) and (5.17) give rise to isotropically distributed deuterium atoms of 0.3eV. Based on the results regarding the reaction probabilities of the D(2s) state of the deuterium atom presented above, these deuterium atoms are assumed to decay to the ground state immediately after creation. To calculate the electron energy loss, it is further assumed that all the lost electron energy goes to the excitation of the molecule. The dissociation threshold of $B'^1\Sigma_u^+$ is 16.65eV above the ground state energy [103]. As the typical kinetic energy of the fragments from this channel is 0.3eV per fragment, the electron loss is assumed to be 17.25eV

Dissociation Through $B^1\Sigma_u^+$ and $C^1\Pi_u$

Excitation to the states C1 and B1 might lead to bound vibrational states or

directly to dissociative states of the vibrational continuum. The latter however is very improbable for electron impact on the ground state ($X^1\Sigma_g^+, v = 0$), whereas the cross section for (DE) through $B^1\Sigma_u^+$ and $C_1\Pi_u$ rise very quickly with increasing vibrational quantum number electron for scattering on ($X^1\Sigma_g^+, v_i$), [103]. However, as this model is restricted to treating the vibrational ground state of deuterium, only excitation into bound vibrational levels of the excited states are relevant. The states $B^1\Sigma_u^+$ and $C_1\Pi_u$ decay to the ground state $X^1\Sigma_g^+$ by emission of radiation with short lifetimes of approximately 1ns [106], [107]. A fraction of these decays are into the vibrational continuum of the ground state and thus lead to dissociation of the ground state into 2D(1s) atoms [80]. The energy of the neutral fragments resulting from these dissociation channels can be estimated by use of the spectra presented in [108] and [97]. These authors report composite spectra of emission from decays to the vibrational continuum of $X^1\Sigma_g^+$ from the singlet states $B^1\Sigma_u^+$, $C^1\Pi_u$, $D^1\Pi_u$ and $B'^1\Sigma_u^+$, where $B^1\Sigma_u^+$ is stated as the main contributor. These spectra are peaked around a significant resonance at approximately 1580 Å corresponding to a photon energy of 7.85eV. The energies of the states $B^1\Sigma_u^+$ and $C^1\Pi_u$, which are the channels included for this mechanism, lie close at 12.75eV and 13.22eV, relative to the ground state at its most probable internuclear separation of $R_0 = 1.40a_0$, respectively, [89], [90]. As $B^1\Sigma_u^+$ is dominant I shall simply use 12.75eV for the electron energy loss. The dissociation energy of the deuterium molecule is 4.56eV [109]. The most probable value of the continuum energy ϵ_k is thus estimated as $12.75\text{eV} - 7.85\text{eV} - 4.56\text{eV} = 0.34\text{eV}$ giving a fragment energy of 0.17eV, which shall be used in PISAM. This should however be considered a rough estimate.

PISAM implementation of Molecular Dissociation

- As described above, the channels of dissociation are split into four groups:
 - (1) Dissociation through $b^3\Sigma_u^+$
 - (2) Dissociation through $a^3\Sigma_g^+$ and $c^3\Pi_u$
 - (3) Dissociation through $B^1\Sigma_u^+$ and $C^1\Pi_u$
 - (4) Dissociation through $B'^1\Sigma_u^+$ and $D^1\Pi_u$

Together these shall be referred to as MD (Molecular Dissociation).

In the implementation of PISAM these channels only differ in electron

energy loss and fragment kinetic energy. Given these energies they all proceed through the following steps:

- Save the incoming velocity of D_2 relative to the lab frame.
- Determine the fragment speed from the fragment kinetic energy of the relevant channel.
- Sample random spherical polar angles, by the proper uniform sampling of the unit sphere i.e the azimuthal angle is sampled uniformly over the range $[0, 2\pi]$ and the polar angle is given by $\theta = \cos^{-1}(1 - 2r)$ where r is a uniformly sampled random number in the range $[0, 1]$.
- Use the sampled angles to calculate the velocity of one of the created neutral atoms in the CM frame. Assign the other neutral atom the exact opposite velocity. Add these to the velocity of the incoming molecule in the lab frame, to get the velocities of the fragments in the lab frame.
- Breed the new neutral atoms in the position of the molecular excitation with the calculated fragment velocities.
- Subtract the electron loss for the relevant channel from the electron energy source term at the grid cell of the plasma simulation where the molecular excitation leading to dissociation takes place.

Ionization of Molecular Deuterium

Molecular dissociation as described in the former section is the dominant process for breeding atoms in the low energy region ($T \lesssim 10$). Above this temperature, ionization of molecular deuterium becomes the dominating process for removing molecules and breeding new ions and atoms. At SOL-relevant temperatures and densities, ionization of the deuterium molecule is usually a single-step process. A few ionizations will, however, happen through multiple excitations. The database AMJUEL [82] provides an analytical fit for the effective molecular ionization rate including multi-step processes, based on the works of [110]. This fit is aimed at the hydrogen molecule H_2 , but since the electronic states are practically identical for H_2 and D_2 [80], only minor deviations from the true D_2 ionization rate are expected. The effective ionization rate is plotted in figure 5.12. The small deviation from single-step ionization, when allowing for multi-step processes suggests that at SOL relevant temperatures and densities the vast majority of ionizations happen as single-step processes, but the effective rate shall be used for precision as the added

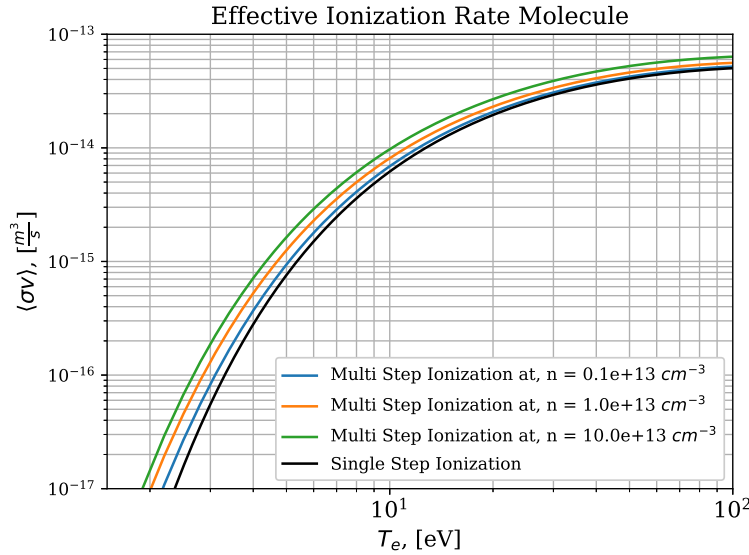


Figure 5.12: Effective reaction rates for ionization of molecular hydrogen as a function of electron density and temperature. The black line gives the rate of single-step ionizations, solely as a function of electron temperature. This plot is based on analytical fits provided by [82, 110]

overhead is minimal. Any multi-step ionization processes are assumed to be instantaneous, such that the transport of exited molecules is not taken into account. The ionization energy of D₂ is 15.48 eV, [111], which is the electron energy loss applied for molecular ionizations in PISAM. When the ground state D₂(1s σ_g , $v = 0$) is ionized by electron impact the created D₂⁺-ion will most likely *not* be in its vibrational ground state. The distribution of the vibrational states of the created molecular deuterium ions can be approximated by the Franck Condon factors of the reaction $e + D_2(X^1\Sigma_g^+, v = 0) \rightarrow 2e + D_2^+(1s\sigma_g, v')$ given by [112, 113]. For any cross sections used for transitions from the ground state, D₂⁺(1s σ_g , v), of the molecular deuterium ion, it shall be assumed that molecular deuterium ions are distributed in accordance with the Franck Condon factors of figure 5.13. The cross sections presented for reactions of electrons with D₂⁺ is thus a Franck Condon weighted average over the cross sections of the relevant process for each initial bound vibrational level of D₂⁺(1s σ_g). The potential curves of the relevant electronic states of D₂⁺ are shown in figure 5.14.

Molecular Ion Dissociation (MID)

The deuterium molecular ion can dissociate by electron impact through a number of processes, [113]:

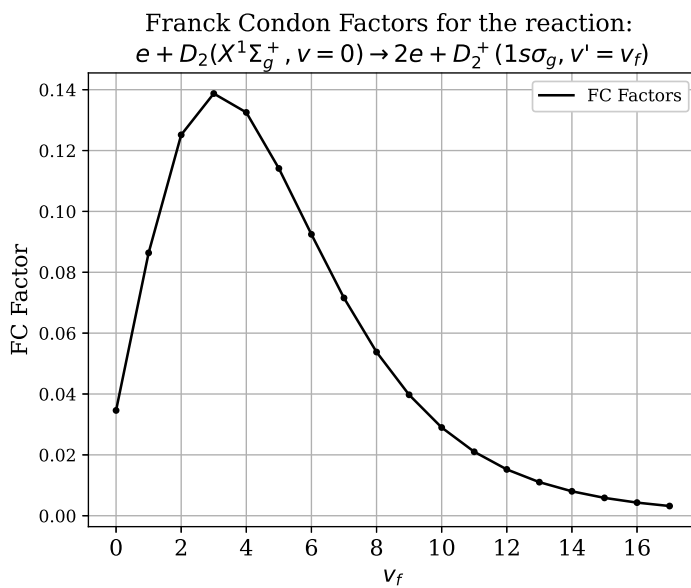


Figure 5.13: Normalized Franck Condon factors of the ionization of the ground state of the deuterium molecule into various vibrational levels of the electronic ground state of the deuterium molecular ion, given by [112]. These are assumed to give the distribution of vibrational states of the deuterium molecular ions at creation.

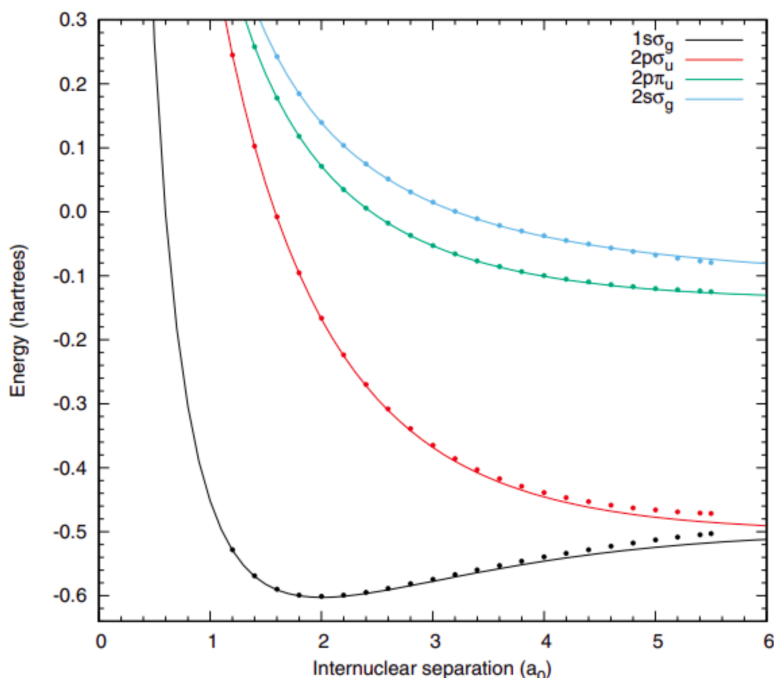
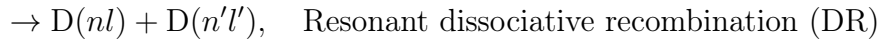
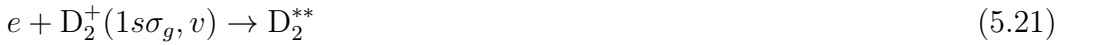
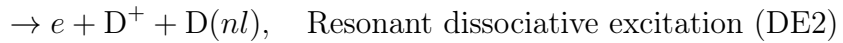


Figure 5.14: Potential curves of the electronic states of H_2^+ determined by spherical (points) and spheroidal (lines) electronic structure calculations. The potential curves are assumed to be identical to the potentials of D_2^+ , for the practical purposes of this thesis. This figure was published in [114].



Where D_2^{+*} denotes an electronically excited state of the deuterium molecular ion and D_2^{**} denotes a doubly excited state of the deuterium molecule. I shall use DE to describe the combined processes of DE1 and DE2. The rates of the different channels are plotted in figure 5.15. Please note that the rate of DE in figure 5.15 is a compilation of theoretical, [98], and experimental, [115, 116], data. The theoretical data used for DE at electron impact energies $E_e > 10\text{eV}$ resembles only the rate of DE1-dissociation as DE2-dissociation is completely neglectable at these high energies [117]. The only reliable data in the low energy region is given by the experimental results of [115, 116], and includes both DE1 and DE2 as these are not separable in present experiments. The composite DE-rate of figure 5.15 is used in PISAM. It shall be argued below why considering DE1 and DE2 as one reaction is reasonable.

Dissociative Ionization (DI)

(5.18) describes an ionization of the Deuterium molecular ion. As both electrons are knocked off the nuclei, the remaining system of two positively charged nuclei is obviously repulsive. Due to its low reaction rate in comparison to the competing processes, see figure 5.15, it is not included in PISAM.

Non resonant Dissociative Excitation (DE1)

In the process of (5.19) the molecular ion is excited to an electronic state above the ground state. All of these states are repulsive, as seen in figure 5.14, and the molecule dissociates. The vast majority of the D_2^+ -ions dissociated through DE1, is excited to either the $(2p\sigma_u)$ state or the $2p\pi_u$ state, [80]. The rates of these channels are plotted in figure 5.16. Since reliable

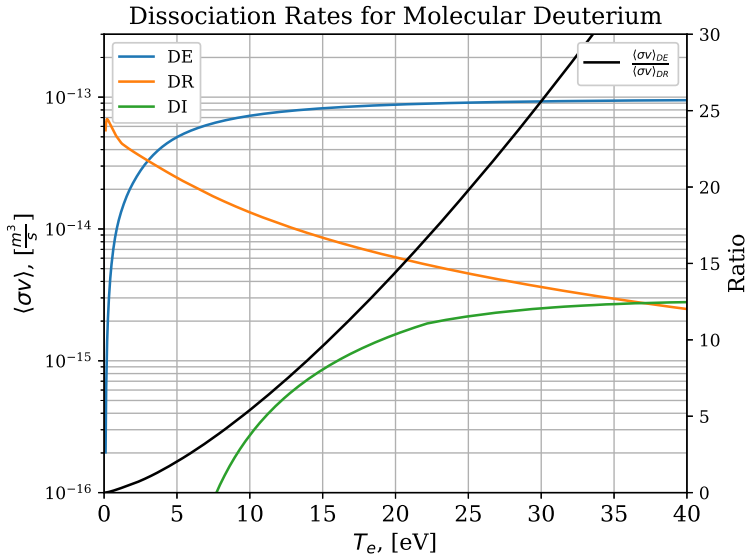


Figure 5.15: Frack Condon weighted reaction rates of dissociative processes in the Deuterium Molecule. The DE cross sections used for calculating the DE rate are based on theoretical data [98] for electron energies $E > 10\text{eV}$, and on experimental data [115], [116] for electron energies $E < 10\text{eV}$. The DR and DI cross sections are obtained from analytical fits provided in [80]. The black line shows the ratio $\frac{\langle \sigma v \rangle_{DE}}{\langle \sigma v \rangle_{DR}}$.

theoretical values are only available for electron impact energies of $E_e > 10\text{eV}$ the values plotted in figure 5.16 are using cross sections of zero for $E_e < 10\text{eV}$, and should thus merely be used in means of comparison of the two dominant DE1 processes. Weighing the ratio $\frac{\langle \sigma v \rangle_{2p\sigma_u}}{\langle \sigma v \rangle_{2p\pi_u}}$ by the temperatures plotted in figure 5.17 gives an average ratio of ~ 8 . Based on this relatively large difference, and the relatively small energy difference between the two electronic states $2p\sigma_u$ and $2p\pi_u$ of approximately 2eV , it shall be assumed that all DE1 dissociations happen by excitation to $2p\sigma_u$.

Resonant Dissociative Excitation (DE2)

(5.20) describes resonant electron capture giving rise to doubly excited states of the deuterium ion. In DE2 the doubly excited state decays by autoionization into the vibrational continuum of the ground state ($1s\sigma_g$) of D_2^+ , by emission of an electron, producing a deuterium ion and a deuterium atom in the ground state, [118]. This process is possible as soon as the electron impact energy exceeds the dissociation energy of the ground electronic state of D_2^+ , [117]. The dissociation energy depends on the vibrational state of the deuterium molecular ion and ranges from $0 - 2.7\text{eV}$, [113]. According to [117] the ratio $\frac{\sigma_{DE2}}{\sigma_{DE1}}$ decreases abruptly to near zero when the electron impact energy exceeds the DE1-threshold for excitation to the lowest excited electronic state of D_2 i.e. $D_2(2p\sigma_u)$. The DE1-threshold for the lowest vibrational states of

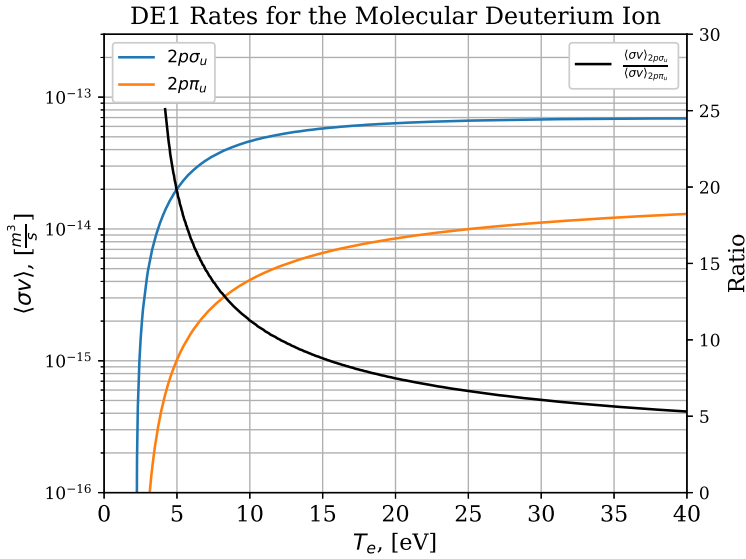


Figure 5.16: Frack Condon weighted reaction rates of the most frequent DE-processes in the deuterium molecular ion. These rates are calculated for electrons impact by electrons with $E > 10\text{eV}$. The black line shows the ratio $\frac{\langle\sigma v\rangle_{2p\sigma_u}}{\langle\sigma v\rangle_{2p\pi_u}}$.

$D_2^+(1s\sigma_g, v)$ is given in table 1. Considering the results for the ratio $\frac{\sigma_{DE2}}{\sigma_{DE1}}$ of [117] along with the values in table 1 and the Frack Condon factors of figure 5.13 it can be assumed that at electron impact energies $E_e \gtrsim 6\text{eV}$ a negligible fraction of dissociation processes go through doubly excited states i.e. DE2 dissociation. The probability distribution of electron impact energy of electrons going into DE-processes in D_2^+ is shown in figure 5.18. The black line is drawn at 6eV , and it is found that around 6% of the DE-processes happen due to electron impacts with energies below this threshold. Based on these considerations, it shall be assumed when calculating the electron energy loss, that the vibrational states of $D_2^+(1s\sigma_g)$ from which (DE) processes originate are distributed with respect to the cross sections of the dominant DE1 channel i.e. $(2p\sigma_u)$.

Resonant Dissociative Recombination (DR)

Rather than decaying by autoionization, the D_2^{**} might be exited to its vibrational continuum at creation, or it can decay to the vibrational continuum of one of the singlet states of D_2 , similar to the predissociation process described in the previous section. These channels constitute the processes termed DR. As seen from figure 5.15 DR dominates at low temperatures ($T_e \lesssim 3\text{eV}$). The ratio $\frac{\langle\sigma v\rangle_{DE}}{\langle\sigma v\rangle_{DR}}$ plotted in figure 5.15 does however decrease rapidly with increasing temperature. Using the temperatures of figure 5.17, the weighted average of the ratio $\frac{\langle\sigma v\rangle_{DE}}{\langle\sigma v\rangle_{DR}}$ is 22.3. This large ratio suggests that DR can safely be

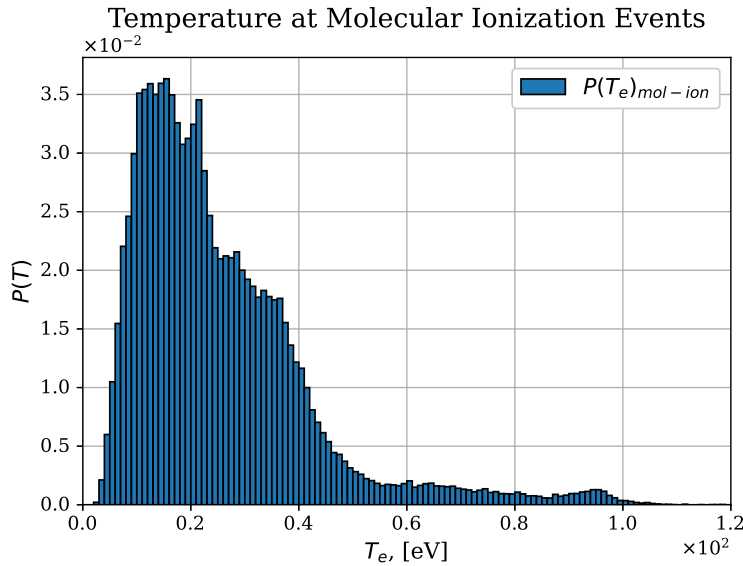


Figure 5.17: Probability distribution of the electron temperature at molecular ionization events. The data shown in this plot results from a simulation of PISAM on dynamic fields representative of plasma edge conditions. The details of the simulation are provided at the beginning of this chapter.

v	0	1	2	3	4	5	6
$\Delta E_{DE}(\text{eV})$	9	7.1	5.8	4.9	4.1	3.3	2.8

Table 1: Electron impact threshold energies for excitation into the $2p\sigma_u$ state of D_2^+ from the electronic ground state $D_2(1s\sigma_g, v)$ [117].

neglected.

Implementation of Molecular Ionization and the Dissociation of D_2^+ in the Model

In the discussion presented above on the dissociation of the molecular deuterium ion, it is argued that one can reasonably assume that all D_2^+ -ions dissociate through DE1 and DE2, where DE1 is dominant. The kinetic energy release (KER) cross section of DE processes in H_2^+ at 15 eV electron impact was measured by [116] and is shown in figure 5.19. Measurements, [116], and theoretical analysis, [114], at higher energies suggest that the probability distribution of fragment energies is very similar for hydrogen and deuterium, justifying the use of the distribution of figure 5.19. The energy distribution of the individual fragments in the CM frame is half of the released kinetic energy due to the similar masses of the fragments. It is assumed that the deuterium molecular ion is at rest in the CM frame as the mass ratio $\frac{m_{D_2}}{m_e} \approx 7.3 \cdot 10^3$. From figure 5.18 it is apparent that 15 eV is a typical velocity for electrons going into DE processes under the relevant conditions, meaning that the KER

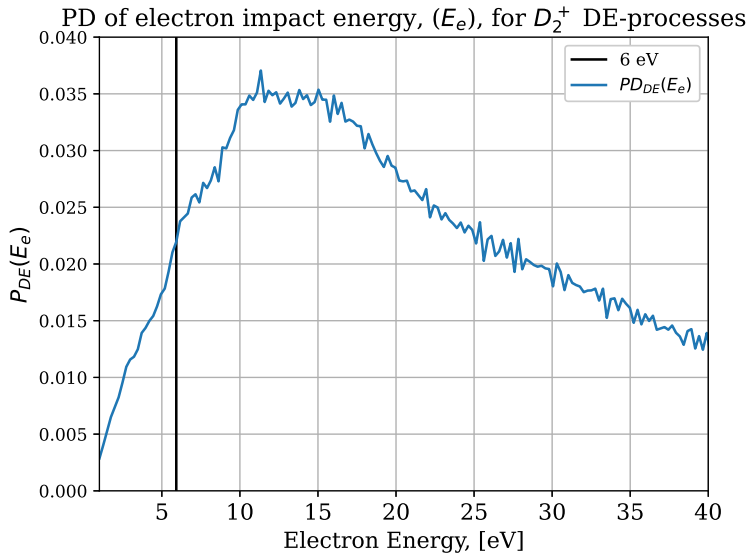


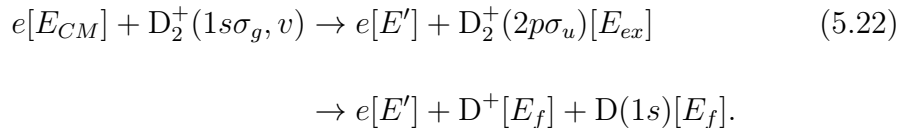
Figure 5.18: The probability distribution of electron impact energy of electrons going into DE-processes in D_2^+ . The data shown in this plot results from a simulation of PISAM on dynamic fields representative of plasma edge conditions.

distribution of figure 5.19 is well suited for use in PISAM. Using the experimental data of figure 5.19 has the advantage that it includes all DE-processes (including resonant and higher excited states), and it thus represents exactly the processes included in PISAM.

Electron Energy Loss and Dissociation Fragment Energy

Knowing the fragment energy, the total electron energy loss of ionization followed by dissociation, is readily evaluated using energy conservation.

At each ionization of a deuterium molecule the ionization energy of 15.48 eV, [111], is lost from the impacting electron. The molecular deuterium ion is then dissociated by electron impact through the reaction



Where the square brackets denote the particle energy in the center of mass (CM) frame of the collision. E_{CM} is the initial electron energy in the CM frame, which is also the total energy in the CM frame due to the assumption that D_2^+ is at rest in this frame. $E' = E_{CM} - E_{loss}$ denotes the energy of the electron in the CM-frame after the collision, where E_{loss} is the potential energy of the excited deuterium molecule relative to its initial state, which must equal the energy lost by the electron, and E_f is the kinetic energy of the

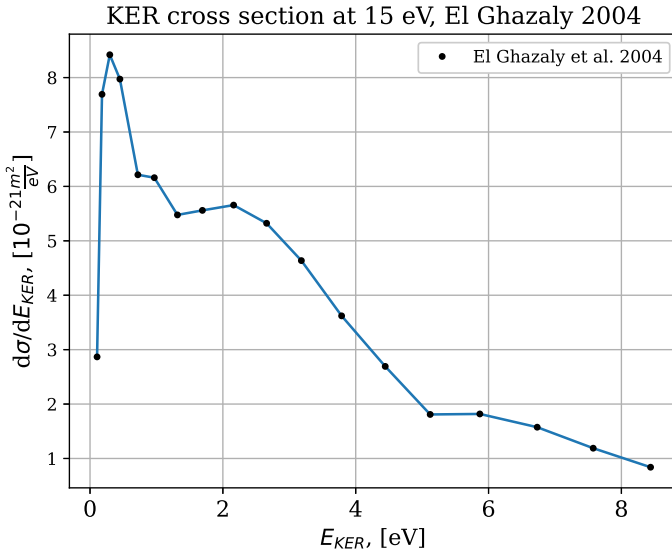


Figure 5.19: Kinetic energy release (KER) cross section of (DE) from 15 eV electron scattering on $H_2^+(1s\sigma_g, v)$. The kinetic energy of each fragment is half of the kinetic energy released.

fragments. Under the current assumptions energy conservation demands:

$$E_{CM} = E_{CM} - E_{loss} + 2E_f + E_{diss}(v) \Rightarrow E_{loss} = 2E_f + E_{diss}(v) \quad (5.23)$$

Where $E_{diss}(v)$ is the dissociation energy of $D_2^+(1s\sigma_g, v)$ into the products D^+ and $D(1s)$. As we are already capable of sampling the fragment energy all we need to determine E_{loss} is the dissociation energy. The dissociation energy of the various vibrational states of $D_2^+(1s\sigma_g)$ are given in [113]. To approximate $\langle E_{diss} \rangle^{21}$, a weighted average of $E_{diss}(v)$ according to the Franck Condon factors of figure 5.13 and the cross sections of the reaction $e + D_2^+(1s\sigma_g, v) \rightarrow e + D_2^+(2p\sigma_u)$ evaluated at 15eV given by [98], has been calculated. This calculation results in an average dissociation energy of 1.61eV. Denote that this implies the assumption that all DE channels have the same dependency of the initial vibrational state on their cross section as the $(2p\sigma_u)$ state. This assumption is justified by the previous argument of $(2p\sigma_u)$ being the dominant channel.

When breeding new particles from molecular ion dissociations PISAM samples fragment energies, from the KER of 15 eV electron impact on $D_2^+(1s\sigma_g, v)$, shown in figure 5.19. On the basis of this sampling, the electron loss is calculated, and a new deuterium atom with the corresponding energy is created. Also, the fragment energy equals the energy gain of the protons.

²¹The brackets denote averaging over the vibrational states.

Transport of D₂⁺

The most probable density and temperature of electrons at the positions where ionization of D₂ occurs is determined by simulation to approximately $2.0 \cdot 10^{19} \frac{1}{\text{m}^3}$ and 16eV respectively. The DE collision frequency of D₂⁺(1s σ_g , v) at this density and temperature is $\sim 1.6 \cdot 10^6 \frac{1}{\text{s}}$, giving a lifetime of $\approx 6.25 \cdot 10^{-7} \text{s}$. This lifetime is equal to 20-60 ion gyration periods depending on the magnetic field of the simulation. The velocity of the molecular deuterium ions at creation is assumed to be equal to the velocity of the deuterium molecule prior to ionization. These are initialized at 0.3eV in the current neutral model, such that their most probable speed is $\approx 3.7 \cdot 10^3 \frac{\text{m}}{\text{s}}$. A typical deuterium ion will thus move $\approx 2\text{mm}$ before dissociating corresponding to 2-5 ion gyration radii depending on the simulation parameters. Due to this relatively short mean free path, it shall be assumed that dissociation follows instantaneously after molecular ionization, even though the molecules are rather long-lived compared to Ω_i^{-1} .

Model Steps for Molecular Ionization

- Save incoming D₂ velocity in the lab frame.
- Sample total fragment energies from the distribution of figure 5.19, and calculate the fragment speed.
- Sample random spherical polar angles, by the proper uniform sampling of the unit sphere i.e the azimuthal angle is sampled uniformly over the range [0, 2π] and the polar angle is given by $\theta = \cos^{-1}(1 - 2r)$ where r is a uniformly sampled random number in the range [0, 1].
- Use the sampled angles to calculate the velocity of the created neutral atom in the CM frame. Assign the proton the exact opposite velocity. Add these to the velocity of the incoming molecule in the lab frame, to get the velocities of the fragments in the lab frame.
- Breed the new neutral atom in the position of the molecular ionization with the calculated fragment velocity.
- Add the contributions to the source terms at the grid cell of the plasma simulation where the molecular ionization took place.

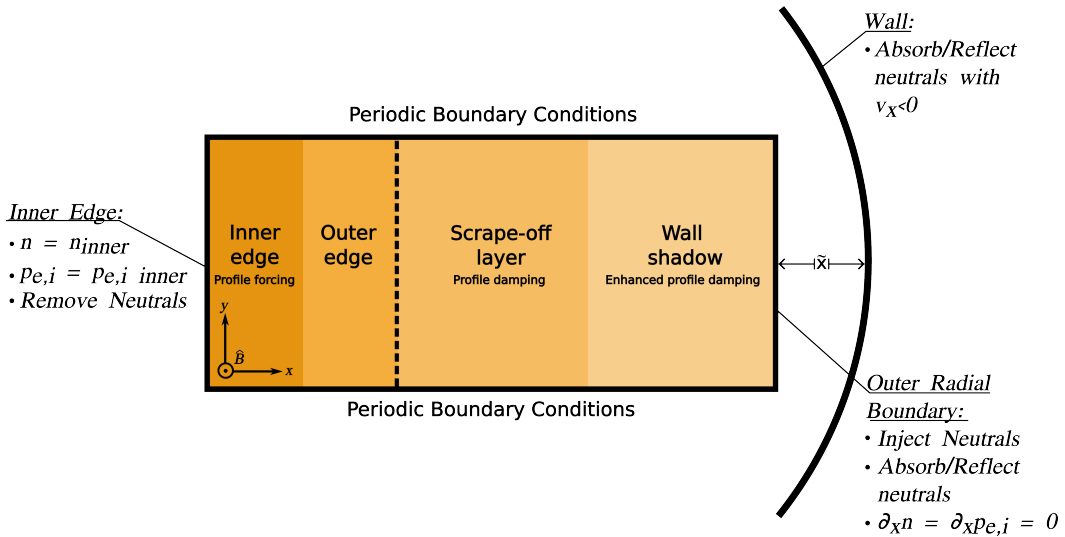


Figure 5.20: Simulation domain of the PISAM-HESEL model, with boundary conditions for plasma and neutrals. In the present slab coordinate system, the x -axis corresponds to the radial axis, and the y -axis corresponds to the poloidal axis. The dashed line indicates the last closed flux surface.

6 Numerical Implementation

This chapter is concerned with concrete details of the numerical implementation of the PISAM-HESEL model. A thorough account of the boundary conditions of the combined model is given, as they are important in the analysis of particle and energy transport mediated by neutrals presented in chapter 8. Moreover, the parallelization of PISAM and the innovative method for coupling Python and C++ with MPI, used to set up efficient communication between PISAM and HESEL, are described. For additional design and implementation details of PISAM and HESEL the reader is referred to appendix D and the articles [76, 119], respectively.

6.1 Implementation of PISAM in Python

Besides presenting the boundary conditions specific to PISAM, this section derives the correct method of calculating the reaction probabilities of a particle with multiple possible reaction channels. Lastly, the choice of using Python for the implementation of PISAM, with its advantages and drawbacks, is discussed.

Neutral Injection and Boundary Conditions

The domain of PISAM-HESEL is shown in figure 5.20. Neutral molecules enter the domain uniformly distributed over the outer radial boundary. The flux of molecules and their initial temperature are user input parameters. The molecules are injected with velocities sampled from the 3D Maxwellian distribution corresponding to the injection temperature. Obviously, only negative radial velocities are allowed. If a particle traveling radially outwards reaches the outer radial boundary it is absorbed by probability γ , and otherwise reflected. If a neutral particle crosses the inner radial boundary, termed the "inner edge", it is removed from the simulation. The boundaries along the y -axis, corresponding to the poloidal direction, are periodic. To avoid an unnatural build-up of radially slow molecules the "wall" boundary condition indicated in figure 5.20 is imposed. Any particle traveling so far in the poloidal or toroidal direction that it collides with the reactor wall is absorbed by probability γ and otherwise reflected. If caused by the wall boundary condition a reflection corresponds to the particle being returned to its birthplace (or place of last interaction) from where it will continue with unchanged velocity. Only particles with a negative radial velocity are subject to the wall boundary condition. In its implementation, it has been assumed that the cross section of a Tokamak is circular²². Basic geometry shows that the condition of being inside the device wall is

$$y < \sqrt{2\tilde{x}a - \tilde{x}^2} \quad \text{and} \quad z < \sqrt{2\tilde{x}R - \tilde{x}^2}, \quad (6.1)$$

where y and z are the slab coordinates in the poloidal and toroidal direction respectively, a and R are the minor and major radii, and \tilde{x} is the distance between the outer radial boundary and the outer wall at $y = 0$ as shown in figure 5.20. \tilde{x} can be set according to the relevant simulation, and how aggressive the dampening of radially slow molecules should be. The smallest sensible choice of \tilde{x} , corresponding to that where the outer radial boundary is only exactly enclosed by the wall is $\min(\tilde{x}_{min}^y, \tilde{x}_{min}^z)$, where

$$\tilde{x}_{min}^y = a - \sqrt{a^2 - \frac{L_y^2}{16}}, \quad \text{and} \quad \tilde{x}_{min}^z = R - \sqrt{R^2 - \frac{L_z^2}{16}} \quad (6.2)$$

where L_y and L_z are the domain sizes along the poloidal and toroidal axes respectively. This minimum has been applied in the current simulations.

²²In reality the cross section is significantly elongated as shown in figure 1.1, so this boundary condition will remove slightly more molecules from the system due to absorption than what is realistic.

Calculating Decay Probabilities from Decay Frequencies

As described in chapter 3 the collision frequency of a single particle due to a reaction with cross section $\sigma(g)$ is $n\langle\sigma(g)g\rangle$, where n is the density of the species with which the particle reacts, and g is the relative speed of the reacting particles. As the numerical model progresses in discrete time steps Δt one needs to be able to calculate the probability of a specific reaction during each time step. To derive the relation between reaction frequency and probability, consider a particle that is capable of reacting with surrounding particles in k different ways, each with reaction frequency Γ_i for $i \in \{1, 2, \dots, k\}$. Let the total reaction frequency, Γ , be defined as $\Gamma = \sum_{i=1}^k \Gamma_i$. Consider an ensemble of such particles all moving with the same velocity and in identical surroundings. Assume that the surroundings are constant during Δt such that Γ_i are constant within each time step. The number of particles, N , that has not yet reacted is then constrained by the differential equation

$$\frac{dN}{dt} = -\Gamma N. \quad (6.3)$$

Let the number of particles that have not reacted at $t = 0$ be denoted N_0 . Then (6.3) is solved by

$$N(t) = N_0 e^{-\Gamma t}. \quad (6.4)$$

During an infinitesimal time step dt , N can be assumed constant, such that the number of reactions of type i during dt is given by $N(t)\Gamma_i dt$. The total number of reactions of type i during a time step Δt is then given by

$$C_i = \int_0^{\Delta t} N(t)\Gamma_i dt = \Gamma_i \int_0^{\Delta t} N_0 e^{-\Gamma t} dt = \frac{\Gamma_i}{\Gamma} N_0 (1 - e^{-\Gamma \Delta t}). \quad (6.5)$$

From the view of a single particle, the probability of undergoing a specific reaction i during Δt is then

$$P_i = \frac{C_i}{N_0} = \frac{\Gamma_i}{\Gamma} (1 - e^{-\Gamma \Delta t}), \quad (6.6)$$

which is the way PISAM calculates reaction probabilities.

Advantages and Drawbacks of using Python

The advantage of implementing sub-modules for BOUT++ in Python rather than in C++ is the ease and speed with which Python code can be written in comparison to C++ code. The ease of writing Python code is due to the dynamic type system and the automatic garbage collection. These features

are however also the very root of the drawbacks of Python - very little memory control and bad performance, especially when using loops.

The first of these issues means that it requires advanced domain knowledge to know exactly when memory is being allocated due to copying of existing variables, and that information about the deallocation of memory is not accessible to the user. The consequence is that memory usage is rarely optimal, with spending more memory than you need and reusing less than you could.

The issue of bad performance when using `for`-loops is obviously critical in the current application where millions of particles are iterated over during each timestep. This issue can be effectively handled by vectorization of the `for`-loops using `numpy`. `numpy` routines are implemented in efficient C and Fortran code, and run usual tasks (e.g. element-wise arithmetic operations), on arrays as small as 1000 elements, 50-100 times faster than the corresponding pure Python implementation [120].

A thorough effort has been made to utilize this major speedup maximally, such that no core functionalities in the implementation of the kinetic neutral model uses Python `for`-loops when executing a time step.

6.2 Implementation of HESEL in BOUT++

HESEL is implemented in the BOUT++ framework, [121], which is a C++ tool developed for solving plasma transport equations in user-defined magnetic field geometries. BOUT++ relies on finite difference schemes to determine gradients. An array of different PDE solvers are available for solving the resulting equations. In the current work, the variable time step solver PVODE has been applied in the simulations. HESEL is parallelized over the radial axis, such that the domain of each partition have dimensions $(N_x/N_C^{C++}, N_y)$, where N_x and N_y are the grid dimension in the radial and poloidal directions respectively and N_C^{C++} is the number of cores running HESEL. In the following, details on the boundary conditions and regional forcing and damping across the domain of HESEL are presented.

The poloidal boundaries of HESEL are periodic. A Dirichlet boundary condition is imposed on the inner edge, IE²³, such that

$$n = n_{IE}, \quad p_e = p_{e,IE} \quad p_i = p_{i,IE}. \quad (6.7)$$

These are realized by the use of forcing profiles in the inner edge region with values at the boundary satisfying those of (6.7). The forcing is imposed on the

²³The left boundary of figure 5.20.

fields by adding artificial source terms to the model equations. These source terms take the form

$$S_{\text{force}}(x) = \frac{1 - \tanh\left[\delta_f\left(x - \frac{x_s + x_{IE}}{2}\right)\right]}{\tau_{\text{force}}} (f - f_{\text{force}}), \quad (6.8)$$

where f denotes the relevant field, δ_f is a smoothness parameter, x_s and x_{IE} are the radial coordinates of the LCFS and inner edge boundary respectively, and $1/\tau_{\text{force}}$ is the damping frequency of the force terms. Usually $1/\tau_{\text{force}} \sim \frac{\Omega_{i0}}{50}$. f_{force} denotes the forcing profile of the specific field. These are usually given by

$$n_{\text{force}} = n_{EI}, \quad p_{e,i,\text{force}} = p_{e,i,EI} + \frac{x - x_{IE}}{x_s - x_{IE}} (p_{e0,i0} - p_{e,i,IE}), \quad (6.9)$$

where p_0 denotes the reference pressure at the LCFS.

The outer radial boundary is subject to a Neumann boundary condition set by

$$\frac{\partial n}{\partial x} = 0, \quad \frac{\partial p_{e,i}}{\partial x} = 0. \quad (6.10)$$

The modified vorticity $\nabla_{\perp}^2 \phi^*$ is not explicitly subject to profile forcing. At the inner edge and the outer radial boundary, it retains Dirichlet values of zero.

6.3 Parallelization and Coupling

This section explains how PISAM is parallelized using MPI and how PISAM and HESEL are coupled through MPI.

Parallelization of PISAM

In the current implementation where neutral-neutral collisions are not considered PISAM is an embarrassingly parallel application. To explain the parallelization, imagine calling PISAM with a physical particle flux F , and a super-particle weight W . The injection rate of super-particles, f , is then given as $f = L_y L_z F / W$, where L_y and L_z are the lengths of the domain along the poloidal and toroidal axes respectively. Instead of initializing *one* instance of PISAM with an injection rate of super-particles equal to f , N_C^{Python} instances are initiated, where N_C^{Python} is the number of cores running PISAM, each with an injection rate of super-particles equal to f/N_C^{Python} i.e. N_C^{Python} instances of `Simulator`, `H_atoms`, `H_molecules` and `Domain` are created. For an introduction to these classes see appendix D. All instances of PISAM cover the full simulation domain, such that all instances of `Domain` hold equal values for the

plasma fields at all times. During a time step Δt , each instance of PISAM is run without communication with other instances. At the end of each time step, the sources from each instance are summed before they are passed to the plasma part of the code. The summation is carried out by collective communication using `MPI.Reduce()`, with the intracommunicator grouping the ranks in the Python part of the program. How these communicators are set up is covered in the following section. Apart from its simplicity, this method of parallelization has the advantages of being potentially indefinitely parallel and securing an even workload on all processors.

Coupling of PISAM with HESEL

Figure 6.1 illustrates how the communication *within* each part of the program, i.e. PISAM and HESEL, is achieved, and how PISAM and HESEL communicate with each other. The C++ and Python parts of PISAM-HESEL are called simultaneously on n_1 and n_2 processors respectively, using a command of the form `mpirun -n n1 cpp_program : -n n2 Python Python_program`. This call initiates a `World Communicator` with $n_1 + n_2$ ranks. The ranks belonging to each program can be identified by using the application number provided by MPI, which is utilized in a call to `MPI.Split()`, splitting the `World Communicator` into two `Sub Communicator`'s. After this procedure, the communicator of `BOUT ++` is set to be the `Sub Communicator` of the C++ part instead of `World Communicator`, which is the default. The `Sub Communicator` of the Python part is used to distribute the plasma fields to each rank of the Python part, before performing each time step. Moreover, it performs the reduction of the sources of each rank to the total sources obtained during each time step. To establish the communication between PISAM and HESEL both `Sub Communicator`'s call `MPI_Intercomm_create` with an identification tag to create an `Inter Communicator` from the two `Sub Communicator`'s. This `Inter Communicator` has two primary jobs; Sending the plasma fields from HESEL to PISAM and sending the sources calculated by PISAM to HESEL. As mentioned in 6.2, HESEL is parallelized along the radial axis, which must be accounted for when communicating between PISAM and HESEL. To accommodate for this subdivision of the spatial domain, the fields of HESEL are passed to PISAM by a call to `MPI_Gather()`, rooted on `rank_0` in the Python part, thus gathering the fields from the full spatial domain in this rank, from which they can be passed to the other ranks running PISAM using `MPI_Broadcast()` with the `Sub Communicator` of the Python part. In a similar manner, the `Sub Communicator` of the Python part

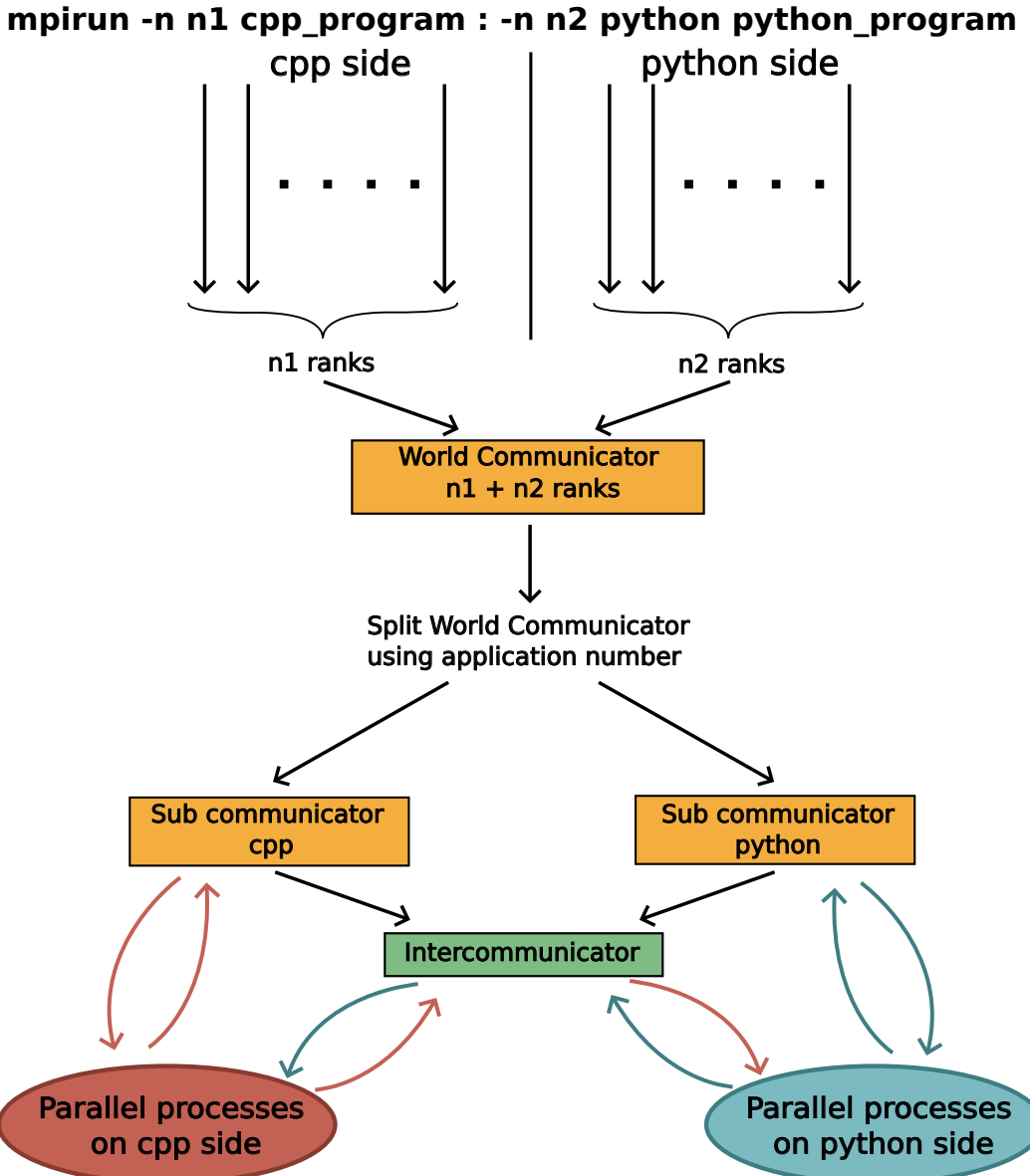


Figure 6.1: An illustration of the method for simultaneously launching parallel Python and C++ programs and setting up the communication between them using MPI.

sums all sources from the instances of PISAM by a call to `MPI_Reduce()` rooted on `rank_0`, from which `MPI_Scatter()` is called to distribute the sources to the spatial domains corresponding to each rank of the HESEL.

The solution presented here for coupling Python and C++ using MPI is pioneering work, that has not been successfully attempted before, to my knowledge. At least I haven't been able to find anybody using this approach on the world wide web. It has been implemented on the HPC cluster Marconi, [122], with the Python part and the C++ part both spanning multiple nodes. The performance is robust and with blazing speed.

7 Timestep Determination and Estimation of Neglected Collisions

This chapter presents the results of a PISAM simulation conducted with static plasma fields. Aside from providing a first verification of PISAM, the results shall be used to substantiate the choice of the simulation time step of PISAM. Similarly, the results will be used to set the super-particle weight for future experiments. Furthermore, the output of the simulation will be the foundation for estimating the source terms of collision processes not currently included in PISAM. The simulation from which the static fields are sampled was conducted with the same simulation parameters as the simulation presented at the beginning of chapter 5. Characteristic quantities are repeated here for convenience

$$n_0 = 3 \cdot 10^{19} \text{ m}^{-3} \quad T_{e,0} = T_{i,0} = 40 \text{ eV} \quad B_0 = 2 \text{ T}, \quad (7.1)$$

such that the time and length scales are set by

$$\Omega_{i0} = 9.59 \cdot 10^7 \text{ s}^{-1}, \quad \rho_{s0} = 6.5 \cdot 10^{-4} \text{ m}. \quad (7.2)$$

The flux of neutral molecules of the current simulation is $5 \cdot 10^{20} \text{ m}^{-2} \text{ s}^{-1}$, and the domain spans roughly 6 cm in the radial as well as the poloidal direction. The domain size along the toroidal dimension is set to unity length i.e. 1 m. The time step used for the neutrals is 5 ns. At the conditions of the static fields, illustrated by figures 7.1 and 7.2, and a super-particle weight of $1.44 \cdot 10^6$, around $224 \cdot 10^6$ super-molecules are present in the simulation domain at saturation. The analog value of atoms is $82.3 \cdot 10^6$.

7.1 Qualitative Verification

Figures 7.3 and 7.4 show snapshots of the densities of neutrals in physical units for molecules and atoms respectively. In these figures, the plasma blobs of figure 7.1 are clearly seen to affect the distribution of neutrals in the corresponding spatial regions. The radial profiles of the neutral densities are

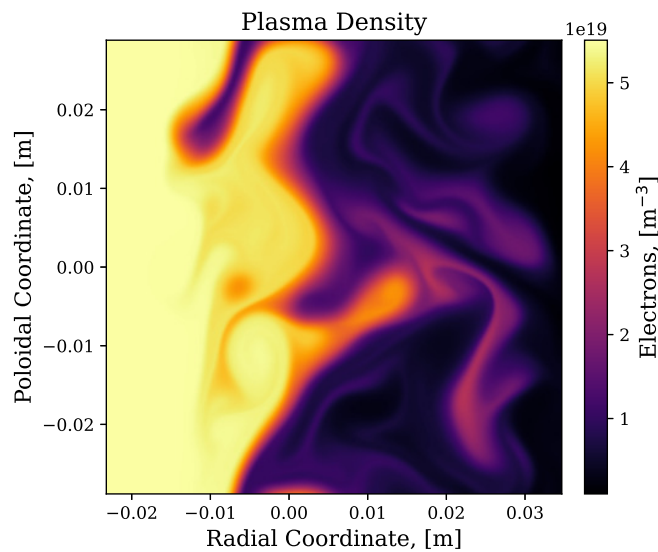


Figure 7.1: Plasma density field used in the simulation that is referred to in this chapter.

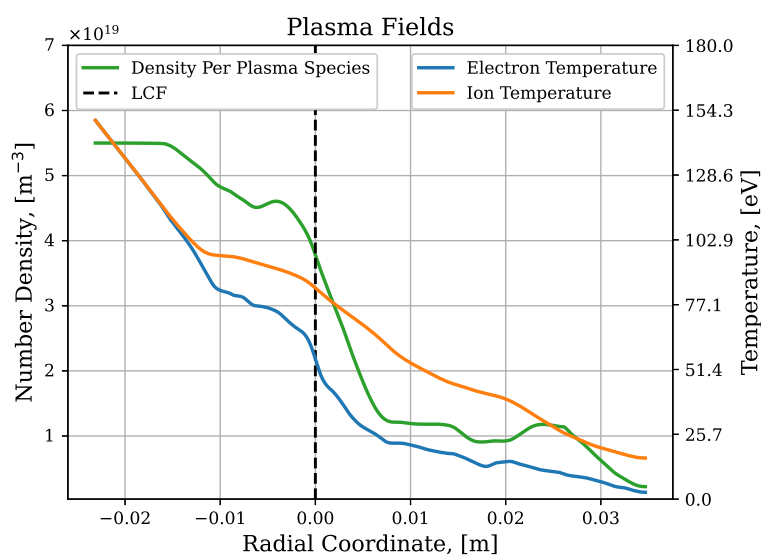


Figure 7.2: Poloidally averaged plasma profiles of the static fields used in the simulation that is referred to in this chapter.

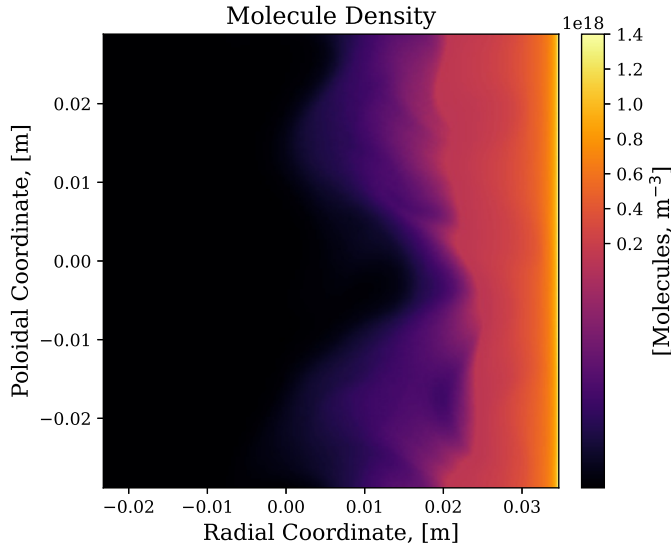


Figure 7.3: A snapshot of the molecule density after saturation on the static fields of figures 7.1 and 7.2, and with the simulation parameters given at the beginning of this chapter.

plotted in figure 7.5. From this figure it is apparent that a large number of molecules accumulate at the radial boundary, creating a density profile that falls off almost exponentially with the distance from the outer radial boundary. Qualitatively similar exponential profiles at the domain boundary are found when using the 2D model of Thrysøe as well as EIRENE in a similar setup [70]. Another feature evident from 7.3, 7.4 and 7.5 is that atoms penetrate deeper into the plasma than the molecules. The main contributor to deep atom penetration is fast atoms that have undergone charge exchange.

7.2 Time Step Determination

In determining the time step used in the neutral simulation multiple considerations are relevant. Most of these considerations shall be thoroughly treated in the discussion section. For now, it will suffice to set the relevant scales for the Courant condition and decide on a reasonable time step based on the speed distribution of neutrals. As described in chapter 4, HESEL, which is based on Braginskii's closure, [17], assumes that the characteristic length-scale of change of the plasma fields, L , is much larger than the ion gyro radius ρ_i i.e. $\rho_i \ll L$. One can thus safely let ρ_i set the Courant condition of the system, meaning that the inequality

$$v_{n,max} \Delta t \leq \rho_i, \quad (7.3)$$

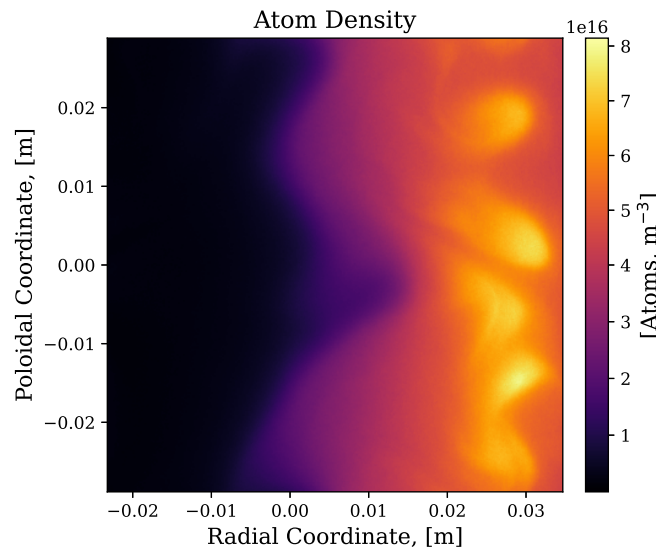


Figure 7.4: A snapshot of the atom density after saturation on the static fields of figures 7.1 and 7.2, and with the simulation parameters given at the beginning of this chapter.

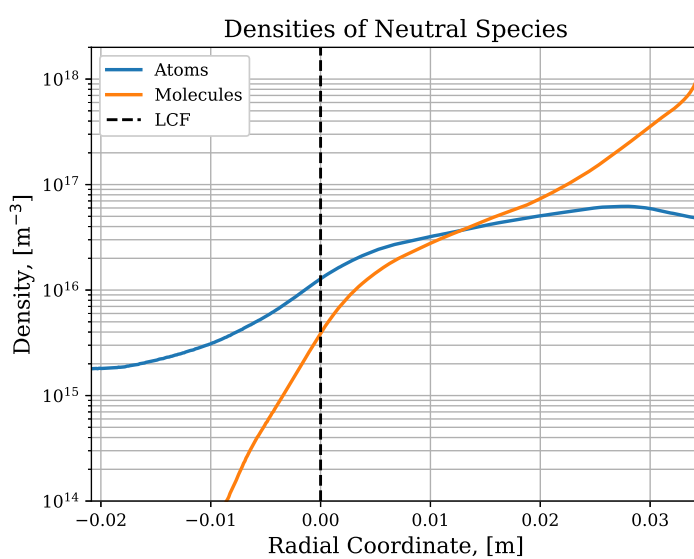


Figure 7.5: A snapshot of the poloidally averaged density profiles after saturation on the static fields of figures 7.1 and 7.2, and with the simulation parameters given at the beginning of this chapter.

should be satisfied, where $v_{n,max}$ is the maximum neutral speed. The CX neutrals will however be distributed with speeds similar to those of a Maxwell-Boltzmann distribution²⁴, with its characteristic long tail. This implies that (7.3) must be relaxed to avoid very short time steps. Instead, the neutral speed for the Courant condition shall be set to the characteristic thermal speed of the Maxwell-Boltzmann distribution best describing the atoms that have undergone CX, see figure 7.6. With the thermal speed of species s given as $v_{t,s} = \sqrt{2T_s/m_s}$ the Courant condition becomes

$$v_{t,n}\Delta t \leq \rho_i \Rightarrow v_{t,n}\Delta t \leq \frac{v_{\perp t,i}}{\Omega_i} \Rightarrow \Delta t \leq \sqrt{\frac{T_i}{2T_n}} \frac{1}{\Omega_i} \Rightarrow \Delta \tilde{t} \leq \sqrt{\frac{T_i}{2T_n}} \quad (7.4)$$

Where \tilde{t} signifies that time has been gyro Bohm normalized, and it was used that $v_{\perp t,s} = \frac{v_{t,s}}{\sqrt{2}}$. A snapshot of the speed distributions of atoms from the current simulation is shown in figure 7.6. The atoms have been divided into two groups; those that have undergone a charge exchange (blue) and those that have not (orange). The individual distributions have been fitted to the Maxwell-Boltzmann distributions giving a measure for the temperature of the atoms. For the simulation at hand, the full domain of the simulation extends from -2.3 cm to 3.5 cm with LCF located at 0. This domain has been divided into 5 equally sized partitions and the speed distribution has been evaluated for each individual partition. It is clear from figure 7.6 that especially the CX atoms are represented by significantly higher temperatures closer to the center of the device. This result was anticipated as the ion temperature follows a similar evolution. By comparison of figure 7.2 and figure 7.6 CX atoms are found to be colder than the ions surrounding them in most of the domain. It is thus assumed that $\sqrt{T_i/2T_n} \lesssim 1$ and in correspondence with (7.4) the time step of PISAM is set to

$$\Delta t = \frac{1}{\Omega_i} = \frac{m_i}{eB}, \quad (7.5)$$

Which shall be evaluated at reference values of the LCFS. The typical magnetic field strength at the LCFS in medium-sized Tokamaks is in the range 1T – 5T, [78, 79], and so the time step of PISAM is in the range

$$\Delta t = \frac{1}{\Omega_{i0}} \approx 4\text{ns} - 20\text{ns}. \quad (7.6)$$

²⁴The exact distribution is given by the integrand of (3.11) and is plotted at various ion temperatures and neutral energies in appendix 5.2.

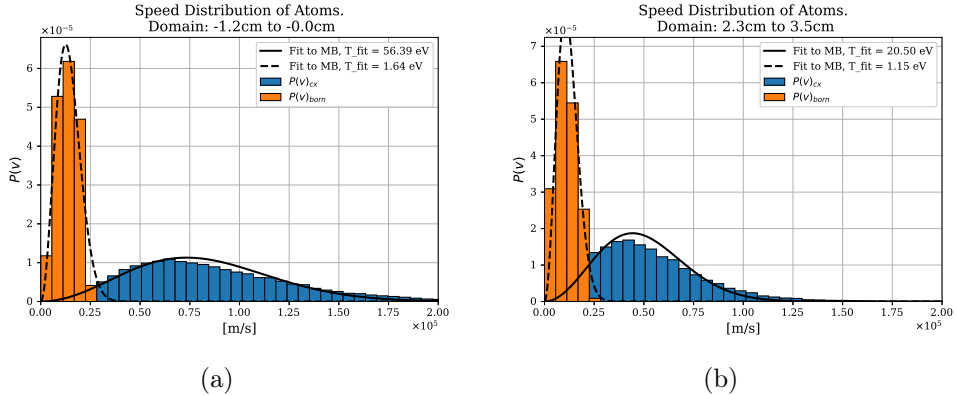


Figure 7.6: Speed distributions of atoms in specific parts of the radial domain. The full domain of the simulation extends from -2.3 cm to 3.5 cm with LCF located at 0. These histograms represent a snapshot of the atom speeds after saturation on the static fields of figures 7.1 and 7.2, and with the simulation parameters given at the beginning of this chapter. The orange bars give the speed distribution of atoms that have not undergone charge exchange, while the blue bars give the speed distribution of atoms that have undergone charge exchange. Both of these distributions are fitted to a Maxwell-Boltzmann distribution to give a measure of the temperature of the neutral atoms.

7.3 Particle Weight and Source Smoothing

Numerous investigations on the relation between grid spacing, particles per cell, and the statistical error in DSMC models have been conducted [123–125]. These are however not applicable to PISAM as its main purpose is to supply a fluid model with the source terms originating from inelastic plasma-neutral collisions, and not just monitor the transport of the neutrals themselves. It is somewhat precarious to couple a fluid model and a discrete particle model like PISAM, as the former is by assumption continuous in its variables and sources, and the latter is by definition discrete. This peculiarity shall be discussed in chapter 9. For now simply note, that if only a few reactions contributing to some source term (like cx reactions contribute to the ion energy source) happen in each time step, this source term will be similar to a sum of Dirac delta functions, sputtered across the simulation domain. Such jagged source terms do not represent the presence of neutrals adequately and are certainly not well fit for a fluid model. As a measure of the adequacy of PISAM in supplying HESEL with source terms, the smoothness of the source terms is used. Smoothness is a vague term, but one approach is to consider a source term smooth if the relative statistical noise, ξ , of each cell is below some threshold ξ_t . The relative statistical noise ξ shall be defined as the ratio of the mean value, μ , of the source term in a given cell, with the standard deviation

due to statistic noise. It is utilized that the binomial distribution becomes a Poisson distribution in the limit where the time step goes to 0 and the number of particles in each cell goes to infinity. The relative statistical error of a Poisson distribution describing a process with a rate λ is $\lambda^{-1/2}$. The condition on ξ can thus be written

$$\xi < \xi_t \Rightarrow \sqrt{\frac{W}{n_n \rho_x \rho_y \rho_z n \langle \sigma v \rangle \Delta t}} < \xi_t, \quad (7.7)$$

where W is the super particle weight, ρ_x , ρ_y , ρ_z are the grid sizes in each of the three dimensions, n_n is the neutral density, n is the plasma density and $\langle \sigma v \rangle$ denotes the total rate of processes contributing to the relevant source. (7.7) is helpful in highlighting the quantities determining the relative statistical error but is inadequate in setting the correct weight for the particles in PISAM as the neutral density of molecules varies so much over the domain that the statistical noise would seem immense when applying (7.7), in the parts of the domain where molecules are sparse. Even if W is approximated using (7.7), in the parts of the domain with the highest inelastic collision frequencies, the calculation leads to very small particle weights, demanding extensive computational resources, for any acceptable ξ_t .

Smoothing

To be able to meet the demand of well-behaved continuous source terms, while keeping the particle weight high enough for the numerical workload to be compatible with the available computational resources, smoothing is applied to the source terms produced by PISAM before passing them to HESEL. Multiple approaches to smoothing are known in the field of Image analysis. Obviously, the current application requires that the smoothing method conserves the total sum of each source term to ensure the conservation of particles, momentum, and energy. One way of achieving this is through 2D convolution of each source with a Gaussian kernel. This approach has an unfavorable scaling, $\mathbf{O}(p^2)$, where p is the number of pixels, making it too slow for the current application. Instead, it is utilized that in the continuum limit (i.e. the pixel size goes towards 0) a convolution of a Gaussian kernel in the spatial domain is equivalent to multiplication with a Gaussian kernel in the Fourier domain, as the Fourier transform of a Gaussian is itself a Gaussian. Using the fast Fourier transform, this approach has the far more tractable scaling $\mathbf{O}(p \ln p)$, [126], and is the method applied in PISAM. The smoothing procedure is outlined as follows:

- 0) Make an array, G with the dimensions of the simulation domain, with values representing a centered normalized Gaussian with the desired standard deviation, σ_b . σ_b is the amount of blurring in the spatial domain. Apply the fast Fourier transform on G to obtain $\mathcal{F}(G)$.
- 1) Let S be a source term obtained in a time step of PISAM. Apply the fast Fourier transform on S to obtain $\mathcal{F}(S)$.
- 2) Do element wise multiplication of $\mathcal{F}(A)$ and $\mathcal{F}(S)$.
- 3) The smoothed source, \mathcal{S} , is now obtained using the inverse fast Fourier transform of $\mathcal{F}(A) \cdot \mathcal{F}(S)$ i.e. $\mathcal{S}(S) = \mathcal{F}^{-1}(\mathcal{F}(G) \cdot \mathcal{F}(S))$.
- Steps 1-3 are repeated for each source at the end of each time step of PISAM.

Locality of Inelastic Collisions

As σ_b is increased the locality of each inelastic collision event is diminished. In the field-perpendicular plane, where PISAM particles are tracked, it was assumed when deriving the fluid model, that the resolved dynamics have a large length scale in comparison to the ion gyro radius ρ_i . To respect this assumption, PISAM should not be able to pass source terms to an area of the plasma not represented by the same macroscopic variables as the area where the event contributing to the source terms happened²⁵. If this is to be strictly respected, the width of the blur should not be larger than ρ_i i.e. $\sigma_b < \rho_i/2$ if the condition is to be met with $\approx 95\%$ accuracy. Satisfying this strict condition turns out not to be accessible with current numerical resources.

Realizing that the delocalization caused by smoothing will defy the underlying assumption of HESEL it is useful to express σ_b in terms of ρ_s , to explicitly quantify this defiance. This is achieved by introducing $\tilde{\sigma}_b = \frac{\sigma_b}{\rho_s}$. The hybrid ion gyro radius, ρ_s , is used rather than ρ_i as it is practical to use the normalization applied in HESEL.

To adjust (7.7) in order to account for blurring, the cell area in the radial poloidal plane $\rho_x \rho_y$ shall be substituted by $a \tilde{\sigma}_b^2 \rho_s^2$, where a is an appropriate constant scaling factor, and it has been assumed that $\rho_x = \rho_y$. In rewriting (7.7) to derive a relation for the specific problem at hand, it shall further be

²⁵See the section *Conditions of Applicability* in chapter 4 for a clarification of this reasoning.

assumed that the neutral density is proportional to the flux, C_f , of molecules over the outer radial boundary,

$$n_n(x, y) = \eta(x, y)C_f. \quad (7.8)$$

Where $\eta(x, y)$ is the inverse characteristic neutral radial velocity modified by a damping profile, the exact expression for η is however not of importance here. By applying $\rho_s = \frac{\sqrt{T_e m_i}}{eB}$ and utilizing (7.6), the statistical uncertainty ξ of (7.7) can be written

$$\xi = \sqrt{\frac{1}{\eta \langle \sigma v \rangle a \tilde{\sigma}_b^2 \rho_z}} \cdot \sqrt{\frac{WB^3 e^3}{m_i^2 T_e^2 n C_f}}, \quad (7.9)$$

which reveals the strong scaling of $B^{3/2}$ on the statistical error with magnetic field. In the current application the source terms do not need to be resolved in the field aligned direction (z-direction) as HESEL is 2D. ρ_z shall thus be set to unity length. Evaluated at characteristic reference values of the LCFS the relative statistical error yields

$$\xi_0 = \left(\langle \eta \rangle_y(x_s) \langle \sigma v \rangle_0 a \tilde{\sigma}_b^2 \right)^{-(1/2)} \cdot \sqrt{\frac{WB_0^3 e^3}{m_i^2 T_{e0} n_0 C_f}}, \quad (7.10)$$

where $\langle \cdot \rangle_y$ denotes an average over the poloidal axis. Except for the rate $\langle \sigma v \rangle_0$ which has a non-trivial dependence on $T_{e0,i0}$, the parameters in ξ_0 influenced by user input, all reside in the second factor. As a consequence of this analysis, the convergence of smoothness shall be formulated in terms of

$$P = \sqrt{\frac{WB_0^3 e^3}{m_i^2 T_{e0} n_0 C_f}} \quad (7.11)$$

where m_i and e are included to make P unitless²⁶.

Numerical Measure of Smoothness

(7.7) is only approximate, and capturing the true effects of blurring and the fact that multiple processes contribute differently to the same sources is mathematically complex. Rather than stepping onto these treacherous paths, a numerical smoothness measure shall be introduced. Specifically, the smoothness of a 2D array, A , shall be defined as the average 2D Laplacian of A divided by the average value of A . The 2D Laplacian of A is given by the convolution of A

²⁶As written here, P actually has units of $\text{m}^{-3/2}$, but since ρ_z equals unit length it can be used to cancel the units of both terms of (7.9) as these are purely spatial.

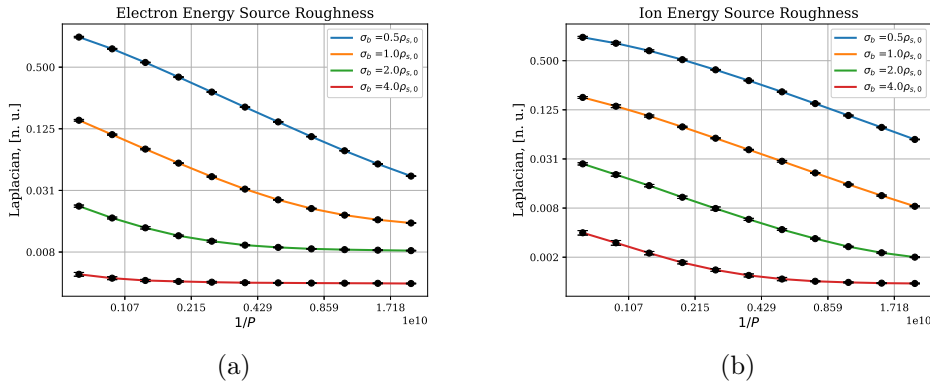


Figure 7.7: The plots show the normalized sum of the Laplacian of a particular source obtained at various values of $\tilde{\sigma}_b$ and P . The Laplacian is calculated by 2D convolution with a Laplacian kernel. The tiny error bars show the standard deviation from the mean of repeated simulations. (a): Electron energy density source. (b): Ion energy density source.

with an appropriate Laplacian kernel. To learn how the smoothness depends on P and the blurring magnitude $\tilde{\sigma}_b$, simulations on the static fields of figures 7.1 and 7.2, have been conducted with various values of these parameters. For each value of P the smoothness of every source has been evaluated at four different values of σ_b . A total of 11 different values of P were scanned. The 44 evaluations of smoothness were normalized by the least smooth source obtained. The results obtained from the electron and ion energy density sources are shown in figure 7.7 on the left and right sides respectively.

The conservative choice of blurring, $\tilde{\sigma}_b = 0.5$ corresponds to the blue curves in figure 7.7. Noting the logarithmic x-axis of figure 7.7, it is clear that convergence is very slow, and that a compromise between locality and numerical efficiency must be sought. The electron energy density source smoothness seems to have reached convergence at $1/P = 0.8 \cdot 10^{10}$ with $\sigma_s = 2$. The convergence of the ion energy density source is generally slower as CX atoms penetrate deep into the plasma where they are present with a small density and exchange much energy and momentum in each reaction. In the interest of good numerical performance, the value of $1/P$ sufficient for the electron energy density source to converge shall be deemed acceptable, even though the ion energy density source smoothness has not converged at this P . To evaluate the validity of this choice visually, a plot of the ion energy source contribution obtained at $1/P \approx 0.8 \cdot 10^{10}$ and $\sigma_s = 2$ is shown in figure 7.8. This grainy source term reflects the compromise between physical adequacy and numerical performance chosen for the PISAM-HESEL simulations presented in chapter 8. In the simulations of the coupled PISAM-HESEL model,

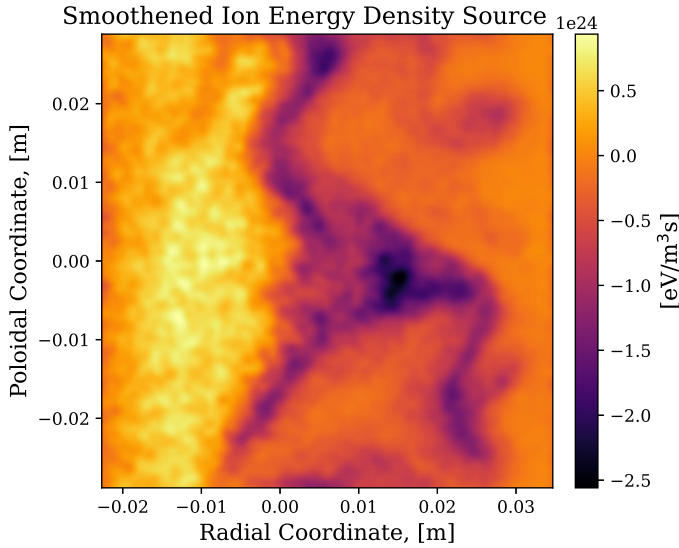


Figure 7.8: The ion energy density source term obtained in one timestep of a simulation of PISAM with $1/P = 0.811 \cdot 10^{10}$ and smoothing magnitude $\sigma_s = 2$.

the super-particle weight shall thus be set according to

$$W = 1.56 \cdot 10^{-20} \frac{m_i^2 T_{i,0} n_0 C_f}{B_0^3 e^3} \quad (7.12)$$

7.4 Elastic Collisions Between Neutrals and Plasma Particles

This section investigates the consequences of neglecting elastic collisions between neutrals and plasma particles. The effects of elastic electron-neutral collisions are expected to be small as the energy exchange is suppressed by the large mass ratio. The relative momentum transfer of the neutrals is equally suppressed by the mass ratio while the relative momentum transfer of an electron colliding elastically with a neutral is of order unity. This causes an energy transfer from the kinetic energy of electron fluid velocity to electron heat. This effect is however so small compared to the analogous effect of electron-ion collisions that it can certainly be neglected. In elastic ion-neutral collisions, on the other hand, the relative energy and momentum transfers are both of order unity. An estimate of the energy source terms arising from elastic plasma-neutral interactions is given below, while the discussion of the effects of momentum transfer in ion-neutral collisions is postponed to chapter 9. The contributions to the energy source terms can be estimated by the elementary theory of binary collisions combined with the assumption that the particles of the colliding species are in individual thermodynamic equilibrium

i.e. if the colliding species are termed 1 and 2, the velocity distributions of each species is a Maxwellian characterized by the macroscopic variables n_1 , \mathbf{u}_1 , T_1 and n_2 , \mathbf{u}_2 , T_2 respectively. For such fluids, the energy exchange rate is given by [127, 128],

$$\frac{dQ}{dt} = -3n_1 \frac{m_1 m_2}{(m_1 + m_2)^2} (T_1 - T_2) \nu_{12} \quad (7.13)$$

Where

$$Q = \int_0^\infty \frac{1}{2} m_1 v_1^2 f_1 d\mathbf{v}_1, \quad (7.14)$$

such that Q is the total energy ascribed thermal *and* fluid velocity. The frequency ν_{12} is defined by

$$\nu_{12} = \frac{4}{3} n_2 \left(\frac{8}{\pi} \right)^{1/2} K^{-1/2} \bar{q}_D. \quad (7.15)$$

Furthermore the following quantities have been defined

$$K = \left(\frac{2T_1}{m_1} + \frac{2T_2}{m_2} \right)^{-1} \quad (7.16)$$

$$q_D(g) = \int (1 - \cos \theta) \frac{d\sigma}{d\Omega}(g) d\Omega \quad (7.17)$$

$$\bar{q}_D = K^3 \int_0^\infty g^5 q_D(g) \exp(-Kg^2) dg \quad (7.18)$$

Such that $q_D(v)$ is the momentum transfer cross section and \bar{q}_D is the weighted average over the momentum transfer cross section, in accordance with the Maxwellian velocity distributions of each species. In the following let the subscript 1 indicate a plasma species and the subscript 2 indicate a neutral species. To estimate the energy exchange rate due to elastic plasma neutral collisions it is assumed that the neutrals are cold. \bar{q}_D shall be given as the momentum transfer cross section at the most probable energy of the plasma species i.e. T_1 . A simplified formula, still adequate for the relevant estimation can thus be written

$$\frac{dQ}{dt} \approx 8 \sqrt{\frac{2}{\pi}} n_1 n_2 T_1 \frac{m_1 m_2}{(m_1 + m_2)^2} \sqrt{\frac{2T_1}{m_1}} q_D(T_1) \quad (7.19)$$

Elastic Electron-Neutral Collisions

Using (7.19) for elastic electron-molecule collisions with the profiles of figure 7.2 and 7.5 and the momentum transfer cross section of [129] yields an estimate of the electron energy sources due to elastic electron-neutral collisions.

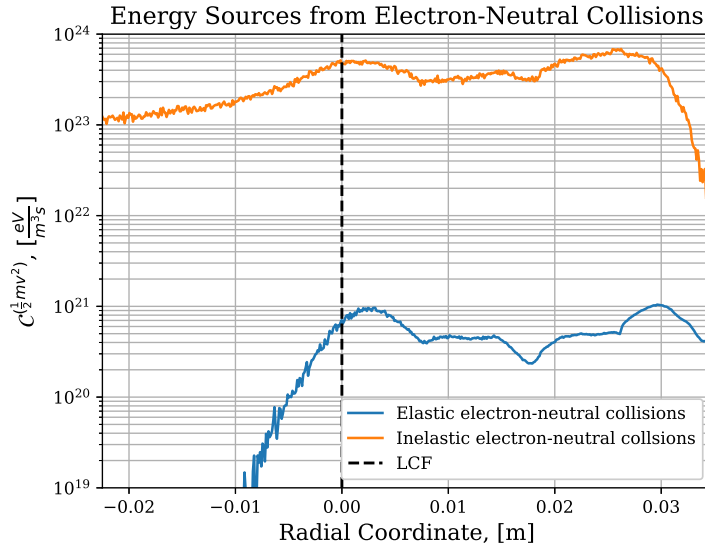


Figure 7.9: The profile of the ion energy density source term produced by PISAM during one time step, along with an estimate of the predicted source terms arising from elastic collisions between electrons and molecules. The simulation was conducted with a super particle size $7.2 \cdot 10^7$. The inflow rate of deuterium molecules was $5 \cdot 10^{20} \text{ m}^{-2} \text{s}^{-1}$ to accomplish a molecule density at the outer radial boundary of approximately 10^{18} m^{-3} .

The source profiles are created by taking the absolute value of the sources distributed in the 2D plain followed by an average over the poloidal axis. This estimate is plotted in figure 7.9 along with the sources obtained from the inelastic collisions currently adopted in the model. As expected from the large mass ratio, figure 7.9 shows that the electron energy density source due to elastic electron-molecule collisions is several orders of magnitude smaller than that of inelastic collisions. The simulation results used in this section are obtained at a higher super-particle weight than the simulation results presented earlier in this chapter. The other simulation parameters are however identical.

The literature on cross sections of elastic collisions between electrons and hydrogen atoms is sparse. It is however expected to be slightly smaller than that of hydrogen molecules [128], and can thus be safely neglected.

Elastic Ion-Neutral Collisions

The momentum transfer cross section of elastic ion-molecule collisions is provided in [130], while that of ion-atom collisions is obtained from [131], partially from extrapolation. Applying a similar procedure to elastic ion-neutral collisions as for the electron-neutral collisions results in the estimates plotted in figure 7.10. The source profiles are created by taking the absolute value of the

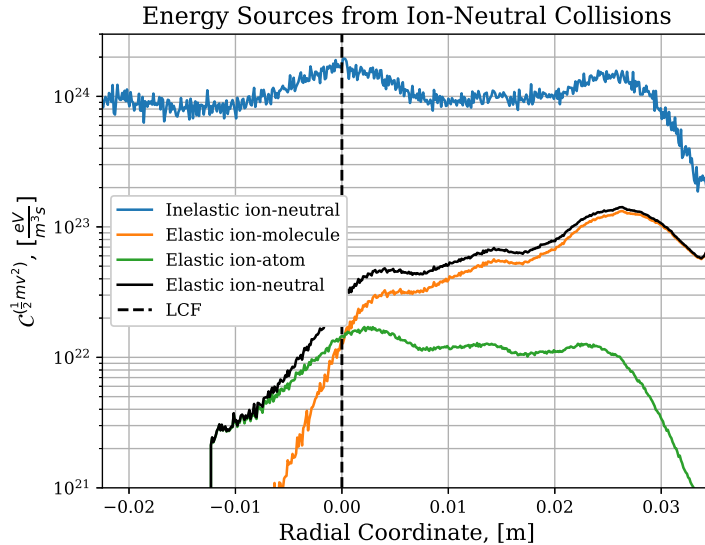


Figure 7.10: The profile of the ion energy density source term produced by PISAM during one time step, along with an estimate of the predicted source terms arising due to elastic collisions between ions and molecules. The simulation was conducted with a super particle size $7.2 \cdot 10^7$. The inflow rate of deuterium molecules was $5 \cdot 10^{20} \text{ m}^{-2} \text{s}^{-1}$ to accomplish a molecule density at the outer radial boundary of approximately 10^{18} m^{-3} .

sources distributed in the 2D plain followed by an average over the poloidal axis. For comparison, the ion energy density source profile is plotted alongside. The data of figure 7.9 shows that the ion energy density source due to elastic ion-neutral collisions is only about one order of magnitude smaller than the energy source due to inelastic collisions, in the region outside the LCFS. At the outer radial boundary, the two contributions are similar in magnitude.

7.5 Radiative Recombination

The primary source of neutrals in the conditions PISAM is tailored to simulate is external gas injection. For some devices recycling from the divertor might also give rise to significant neutral densities at the outboard mid-plane. Moreover, it seems intuitive that a large rate of neutral production could be provided by recombination of the ions and electrons making up the plasma. This section gives a brief argumentation of why such recombination events are not included in the model. The rate of radiative recombination as a function of electron temperature is provided by [86]. This rate is used with the profiles of figure 7.2 to calculate the atom creation rate due to radiative recombination. The result is shown in figure 7.11 along with the profile of atom creation due to the inelastic electron-neutral collisions included in PISAM. This figure

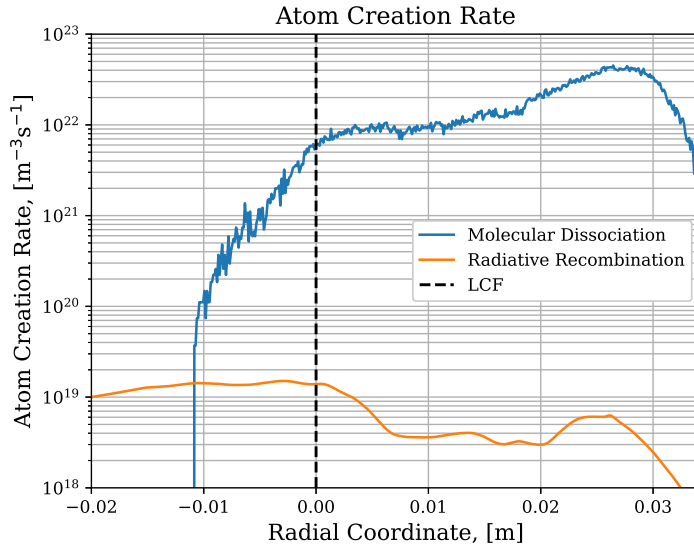


Figure 7.11: The profile of the atom creation rate of PISAM alongside an estimate of the predicted atom creation rate arising due to radiative recombination of ions and electrons. The simulation was conducted with a super particle size $7.2 \cdot 10^7$. The inflow rate of deuterium molecules was $5 \cdot 10^{20} \text{m}^{-2}\text{s}^{-1}$ to accomplish a molecule density at the outer radial boundary of approximately 10^{18}m^{-3} .

concludes that the atom creation rate due to the processes currently included in PISAM is orders of magnitude larger than the rate of recombination in the relevant part of the domain.

8 Results

This chapter presents high-resolution results of the source terms produced by PISAM with static fields, as well as source terms and plasma field profiles obtained using the PISAM-HESEL model in full functionality. The results obtained using static fields clarify many of the mechanisms in the influence of neutrals on edge plasma dynamics. The dynamic simulations provide a persuading qualitative verification of PISAM and its coupling to HESEL, and give rise to exciting ideas for future experiments.

8.1 PISAM with Static Fields

The data shown in this section are the results of a simulation conducted using the static fields of figures 7.1 and 7.2, with $1/P = 2.3 \cdot 10^{10}$, which, in the present case, results in around $2.5 \cdot 10^9$ super-particles in the domain at saturation.

Plasma Density Source

The plasma density source obtained in one randomly sampled time step of this simulation is shown in figure 8.1. The LCFS is located at $x = 0$ suggesting that for this highly turbulent frame, the vast majority of the density source is provided at the low field side of the LCFS. This indicates that for turbulence as significant as that of figure 7.1, gas puffing might not be the right option for fueling. The unbeneficial ionization on the low field side of the LCFS is self-enhancing, as the increased density results in an increased collision frequency of molecular dissociation and atomic ionization. This mechanism suggests that there may be a maximum obtainable fueling rate in gas puffing experiments, which would be interesting to investigate in dynamic simulations.

Electron Energy Density Source

The electron energy source obtained in one randomly sampled time step is shown in figure 8.2. As argued in chapter 5, the electron energy density source terms due to inelastic plasma-neutral collisions are negative in any

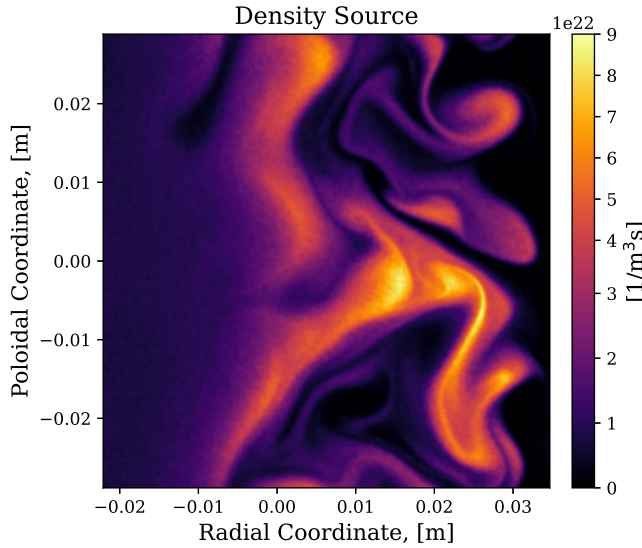


Figure 8.1: Plasma density source of one randomly sampled time step in a simulation of PISAM conducted on the static plasma frames of figure 7.1 and figure 7.2, with $1/P = 2.3 \cdot 10^{10}$ and $\sigma_b = 0.5$.

collision included in PISAM. Any event contributing to plasma density is a heat sink for electrons, and it is thus not surprising that the density source of figure 8.1 is highly correlated with the electron energy density source of figure 8.2. The combined result of the plasma density source and electron energy density source is thus to fill the SOL with cold plasma. Note that due to the low collisionality of a fusion plasma, which is especially true at SOL conditions, the fluid velocity parallel to the field lines is comparable to the thermal velocity. Cold plasma thus hangs in the SOL for longer as it spends more time drifting along the field lines before reaching the divertor. This effect contributes to the self-enhancing mechanism suggested in the previous section.

Ion Energy Density Source

The ion energy source obtained in one randomly sampled time step is shown in figure 8.3. The vast majority of this source originates from CX reactions or ionization of CX atoms. As noted in chapter 7, the image's graininess indicates the sparsity of CX atoms in combination with the large energy exchange that one reaction can entail. It is noted that similar to the effect of neutrals on electron temperature, the SOL ions are cooled due to charge exchange reactions. Figure 8.3 indicates that charge exchange reactions have the effect of moving energy back within the high field side of the LCFS, thus improving energy confinement. On the other hand, the ion energy source of 8.3 would

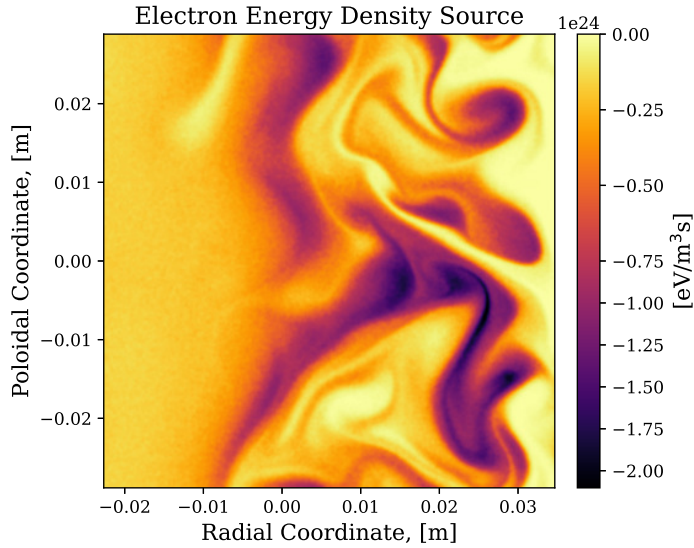


Figure 8.2: Electron energy density source of one randomly sampled time step in a simulation of PISAM conducted on the static plasma frames of figure 7.1 and figure 7.2, with $1/P = 2.3 \cdot 10^{10}$ and $\sigma_b = 0.5$.

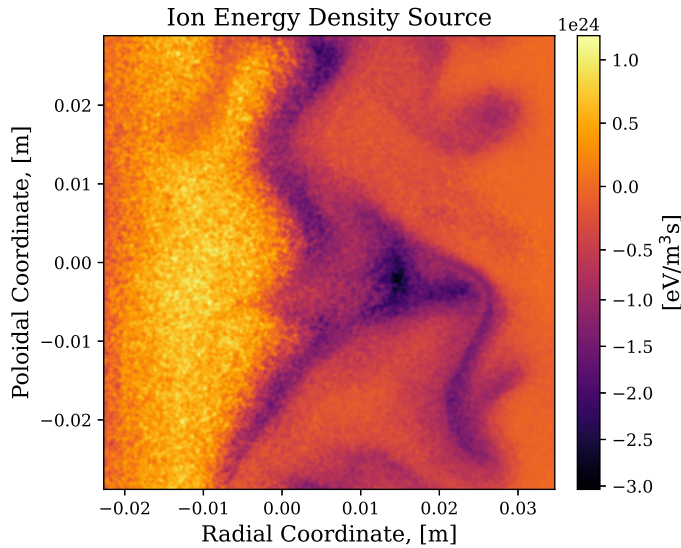


Figure 8.3: Ion energy density source of one randomly sampled time step in a simulation of PISAM conducted on the static plasma frames of figure 7.1 and figure 7.2, with $1/P = 2.3 \cdot 10^{10}$ and $\sigma_b = 0.5$.

seem to enhance the pressure gradient at the LCFS thus further destabilizing the plasma with respect to ballooning.

8.2 PISAM-HESEL

The following section presents simulation results from running the coupled PISAM-HESEL model with its full functionality. The reference quantities at

the LCFS used in the simulations are

$$n_0 = 1.85 \cdot 10^{19} \text{ m}^{-3}, \quad T_{e,0} = T_{i,0} = 60.0 \text{ eV}, \quad B_0 = 0.88 \text{ T}, \quad (8.1)$$

such that the time and length scales are set by

$$\Omega_{i0} = 4.23 \cdot 10^7 \text{ s}^{-1}, \quad \rho_{s0} = 1.7 \cdot 10^{-3} \text{ m}. \quad (8.2)$$

The simulation-specific parameters of the neutrals are

$$C_f = 1.5 \cdot 10^{21} \text{ 1/sm}^2, \quad W = 9.0 \cdot 10^6, \quad (8.3)$$

$$T_n = 0.3 \text{ eV}, \quad \gamma = 0.2, \quad \tilde{\sigma}_b = 2, \quad (8.4)$$

where C_f is the injection flux of deuterium molecules, W is the super particle weight, T_n is the temperature defining the Maxwellian velocity distribution of the injected molecules, γ is the wall absorption coefficient and $\tilde{\sigma}_b$ is the applied blur in units of ρ_{s0} . The reason for and effects of using the fairly high value of T_n is discussed in chapter 9. With these values, the smoothness of the source terms is characterized by $1/P = 0.76 \cdot 10^{10}$, with P defined in (7.11). The results plotted in this section all represent the mean of eight runs seeded with different perturbations on the initial plasma density profile. The runs using the HESEL model without the influence of neutrals have a duration of $1000\Omega_{i0}^{-1}$, while those using PISAM-HESEL have a duration of $450\Omega_{i0}^{-1}$. The first $100\Omega_{i0}^{-1}$ are considered to be a transient period and were not included when calculating the presented profiles. The shadows on the profile plots show two times the standard deviation of the values, from the eight different runs, averaged to obtain each particular data point. The orange curves represent results obtained from running HESEL without the influence of neutrals, while the blue curves represent results obtained from running PISAM-HESEL. Some figures show green curves with the results from running nHESEL with the influence of neutrals modeled by Thrysøes fluid model [70]. These simulations did however never converge, but stacked neutrals at tremendous densities at the edge of the domain. Even though unsuccessful, some results of these simulations are shown when they provide information on the difference between the results of using PISAM and the fluid model of Thrysøe. Moreover, many of the following figures indicate the part of the domain where profile forcing is invoked. An explanation of the applied profile forcing is given in chapter 6.3.

Source Terms Provided by PISAM

To assess the validity of the density source provided by PISAM, consider the condition of conservation of the particles entering and exiting the domain at

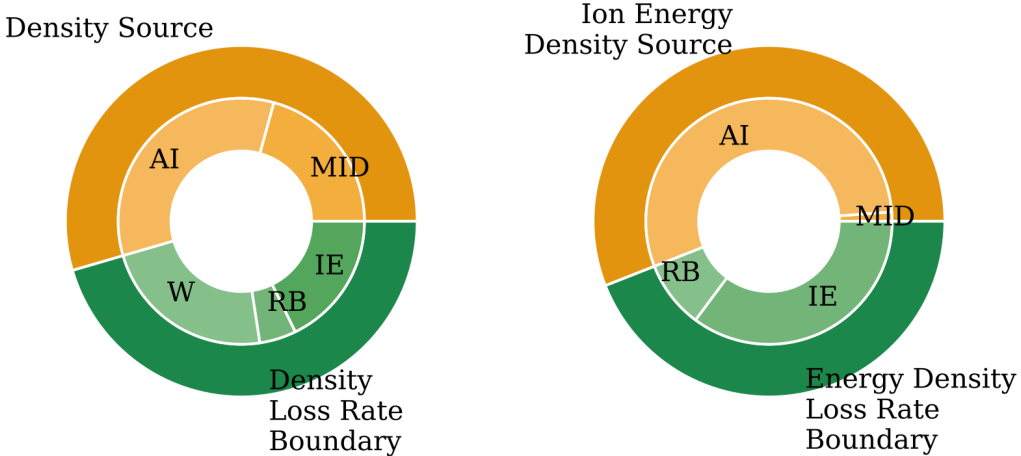


Figure 8.4: The left figure shows the distribution of neutral losses in a simulation on static fields representative of the conditions of the PISAM-HESEL simulations from which results are reported in this chapter. The right figure is analogous but shows the distribution of energy. AI = Atomic Ionization, MID = Molecular Ion Dissociation, W = Wall, RB = Outer Radial Boundary, IE = Inner Edge.

saturation

$$\begin{aligned} \frac{1}{V} \int_V I_{AI}^{(1)} + I_{MID}^{(1)} d\mathbf{r} + \frac{\gamma}{V} \int_{v_x^+} \int_{S^o} f_a \mathbf{v} \cdot d\mathbf{A} d\mathbf{v} + \frac{\gamma}{V} \int_{v_x^-} \int_{S^w} 2f_m \mathbf{v} \cdot d\mathbf{A} d\mathbf{v} \\ + \frac{1}{V} \int_{v_x^-} \int_{S^i} f_a \mathbf{v} \cdot d\mathbf{A} d\mathbf{v} = \frac{2C_f L_y L_z}{V} = \frac{2C_f}{L_x} \end{aligned} \quad (8.5)$$

where $V = L_x L_y L_z$ is the domain volume, with L_x , L_y , and L_z are the domain sizes in the radial, poloidal, and toroidal directions respectively. γ is the absorption coefficient, C_f is the flux of molecules over the outer radial boundary and f_s is the phase space distribution function of species s . The surfaces S^o , S^i , and S^w denote the surfaces of the outer radial domain boundary, the inner radial domain boundary, and the wall boundary. The notation used for the inelastic source terms $I^{(\cdot)}$ is introduced in chapter 2. The notation used for the velocity integrals should be read

$$\int_{v_x^+} d\mathbf{v} = \int_{v_x=0}^{\infty} \int_{-\infty}^{\infty} \int_{-\infty}^{\infty} d\mathbf{v}, \quad \int_{v_x^-} d\mathbf{v} = \int_{v_x=-\infty}^0 \int_{-\infty}^{\infty} \int_{-\infty}^{\infty} d\mathbf{v}. \quad (8.6)$$

(8.5) states that the average inflow rate per unit volume must equal the sum of particle density source and the loss rate at the boundaries per unit volume. The latter is divided into three terms, corresponding to the second, third, and fourth terms of (8.5). The second term gives the loss due to particles with a positive radial velocity being absorbed on the outer radial boundary.

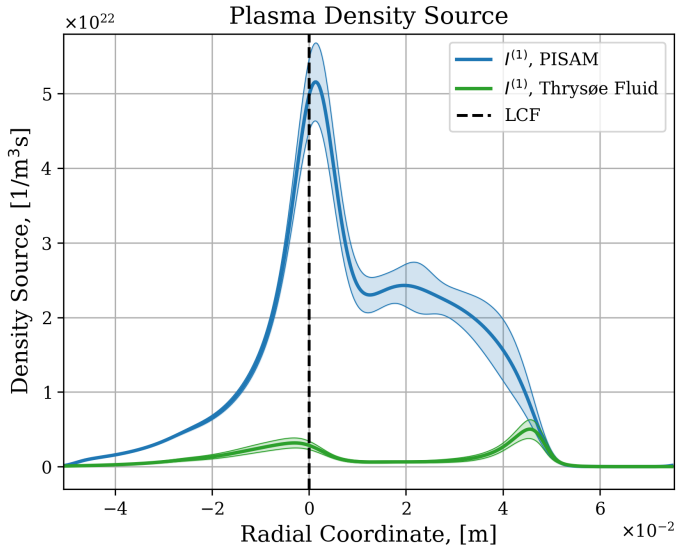


Figure 8.5: Radial density source profiles resulting from averaging the density source terms provided by PISAM in time and over the poloidal axis. The blue curve represents results obtained running PISAM, while the green curve represents results obtained from running Thrysøe’s fluid model [70].

Only atoms are included in this term as molecules cannot have positive radial velocities in the current implementation. The third term gives the loss of particles from molecules absorbed due to the wall boundary condition. Only molecules are included, as very few atoms are absorbed through this channel. The fourth term gives the loss due to particles leaving the domain through the inner edge. Only atoms are included in this term as practically not a single molecule will ever make it that far into the plasma at current molecule injection temperatures. The distribution of particle losses due to the terms on the LHS of (8.5) is shown on the left of figure 8.4. The necessary diagnostics were not fully implemented when dynamic PISAM-HESEL simulations were conducted. The results of figure 8.4 are thus obtained using static fields representative of the simulation conditions of the dynamic runs from which results are presented in this chapter. Including the atoms that escape through the inner edge, a total of $\sim 72\%$ of the injected nuclei end up as plasma ions. Only $\sim 55\%$ of the nuclei contribute to the plasma density within the domain. The radial profile of the plasma density source, made from these $\sim 55\%$, is shown in figure 8.5. Inspecting the shape of the density source from PISAM, it is apparent that some atoms and molecules ionize at large radial distances from the LCFS ($x \approx 3\text{cm}$). These reactions are caused by blobs of plasma escaping into the SOL. Many atoms do however make it to the LCFS where density and temperature rise rapidly and we see the peak of the density source, due to a large rate of ionization. On the high field side of the LCFS, the density source

has a steep cutoff resembling a damped random walk²⁷ of the CX atoms.

The left figure of 8.6 shows the electron energy density source. To validate the magnitude of this source, we note that for each molecule dissociated, the electrons have to supply around 12eV²⁸, while each ionization of an atom claims 13.6eV. The average electron energy density sink rate can then be approximated using the ratios of neutral removal shown in figure 8.4, and are found to be in good correspondence with the average value of the blue curve on the left of figure 8.6, thus verifying that PISAM works as intended with regard to energy exchange in electron neutral reactions. It is of no surprise that the shape of the electron energy density source profile is highly correlated with the density source profile as any inelastic collision contributing to the density source must have energy supplied from the electrons. The main difference between the two profiles except for their scale, is that the bump in the SOL is more distinct in the electron energy density source profile than in the density source profile. The reason is that molecular dissociation reactions are sinks of electron energy, but do not contribute to the density source. To assess the validity of the ion energy density source produced by PISAM, and shown on the right of figure 8.6, consider the energy conservation for the nuclei injected into the system as molecules

$$\begin{aligned}
 & -\frac{1}{V} \int_V I_{CX}^{(\frac{1}{2}mv^2)} d\mathbf{r} + 2\tilde{E}_{frag} \left(\frac{C_f}{L_x} - \frac{\gamma}{V} \int_{v_x^-} \int_{S^w} f_m \mathbf{v} \cdot d\mathbf{A} d\mathbf{v} \right) \\
 & = \frac{1}{V} \int_V I_{AI}^{(\frac{1}{2}mv^2)} + I_{MID}^{(\frac{1}{2}mv^2)} d\mathbf{r} + \frac{\gamma}{V} \int_{v_x^+} \int_{S^o} \frac{1}{2} m_a v^2 f_a \mathbf{v} \cdot d\mathbf{A} d\mathbf{v} \quad (8.7) \\
 & + \frac{\gamma}{V} \int_{v_x^-} \int_{S^w} \frac{1}{2} m_a v^2 f_a \mathbf{v} \cdot d\mathbf{A} d\mathbf{v} + \frac{1}{V} \int_{v_x^-} \int_{S^i} \frac{1}{2} m_a v^2 f_a \mathbf{v} \cdot d\mathbf{A} d\mathbf{v},
 \end{aligned}$$

where \tilde{E}_{frag} is the weighted average of fragment energy, in the lab frame, after dissociation (MD and MID). The LHS of (8.7) is the rate at which kinetic energy is transferred to the neutral atoms from ions and electrons, plus the rate of energy entering the system in the form of the kinetic energy of molecules that are not absorbed on the wall. The RHS of (8.7) is the rate at which energy is lost when neutrals are removed from the domain either due

²⁷This is a slightly biased random walk, as shown in Appendix 5.2.

²⁸A rough weighted average based on the rate and energy losses for MD and MID given in chapter 5.

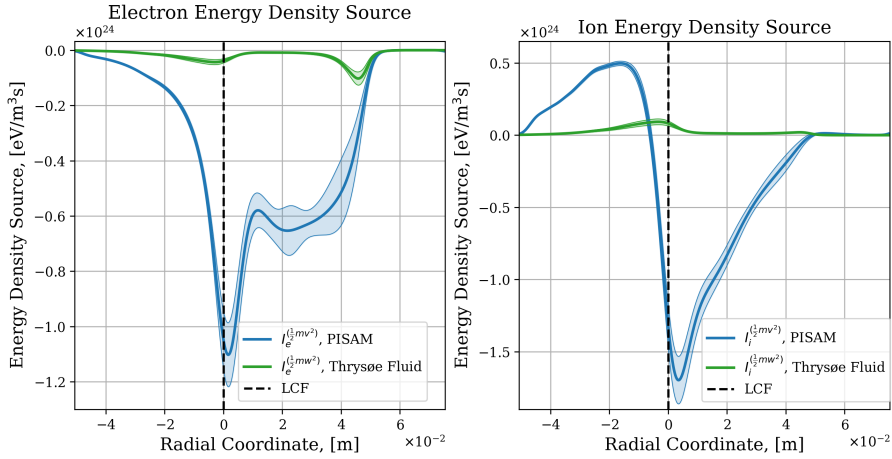


Figure 8.6: Radial energy density source profiles resulting from averaging the energy source terms provided by PISAM in time and over the poloidal axis. The electron and ion energy source profiles are depicted in the left and right figures respectively. The blue curve represents results obtained from running PISAM, while the green curve represents results obtained from running Thrysøe's fluid model [70]. As the legend indicates the results of [70] report the energy density source associated with the random velocity $\mathbf{w} = \mathbf{v} - \mathbf{u}$, rather than the full velocity, \mathbf{v} . The difference is however expected to be small as thermal velocities are assumed large in comparison with fluid velocities, and most momentum transfer cancels by symmetry.

to ionization or boundary losses. (8.7) indicates that if no atoms were lost at the boundaries the average value of the ion energy density profile of figure 8.6 should be $2\tilde{E}_{frag}C_f/L_x \approx 7.2 \cdot 10^{22}$. Two valuable observations can be drawn from comparing this number with the blue curve in figure 8.6. Firstly, the large fluctuations of the measured ion energy density source terms indicate that the energy transport due to CX reactions is very large in comparison to the energy exchange between electrons and ions mediated by neutrals. Secondly, since the blue curve in figure 8.6 integrates to a negative number of order 10^{23}eV/m^2 a large amount of energy carried by neutrals leaves the systems due to boundary losses. The right side of figure 8.4 shows the distribution between the channels from which energy carried by neutrals can be transferred to plasma particles or completely removed from the system. The initial kinetic energy of the deuterium molecules is not included in figure 8.4 as it is very small compared to the kinetic energy that the neutrals draw from the plasma. It is found that $\sim 35\%$ of the kinetic energy transferred to the neutrals from the plasma is transported all the way inside the inner edge of the domain. This energy is carried by only $\sim 23\%$ of the created atoms, with an average energy of $\sim 50\text{eV}$. The source term profiles have served to validate that PISAM behaves as expected, nicely resembling the results found with the static fields of the former section. Furthermore, they have shown how efficient charge exchange

reactions are in transporting particles and especially energy radially inwards. In the next section, the influences of these sources on the plasma fields are presented.

Plasma Density and Temperature Profiles

Figure 8.7 shows the plasma density profiles obtained running HESEL with and without the influence of neutrals. The profiles show a significant increase in SOL plasma density when neutrals are present. The increased magnitude and broadening of the density profile is a well-known phenomenon known as *shoulder formation*. The shoulder shape found here is similar to those found in experimental measurements on ASTEX reported in [132]. Figure 8.8 shows the plasma temperature profiles obtained running HESEL with and without the influence of neutrals. For the electrons, the largest fractional temperature discrepancy occurs in the SOL. At the LCFS where the electron energy density source is peaked, we barely see any change. This is expected to be due to the large advection transport in this highly turbulent part of the domain. For the ions, whose temperature profiles are shown on the right of figure 8.8, a far larger discrepancy between running the models with and without neutrals is reported. Furthermore, it is noted that even though the ion energy density source is positive at $x \lesssim -0.5\text{cm}$ the neutrals are cooled over the full domain. These observations are explained by the large ion heat conduction perpendicular to the field lines, which is due to the large ion mass. The results of figure 8.8 are in good correspondence with the simulation results reported in [133] based on the B2 EIRENE code [54].

8.3 Influence of Neutrals on the Electric Field

Figure 8.9 shows the profile of the radial electric field. The sign of the radial electric field is found to switch just inside the LCFS for both profiles, indicating that the current simulation resembles a reactor operating in H-mode [22, 23, 46], with a large poloidal flow oriented vertically downwards on the inside of the LCFS and an opposite poloidal flow just outside the LCFS. This poloidal shear flow is not changed significantly when introducing neutrals, and thus the current results do not find that gas puffing should cause a transition from H-mode to L-mode, for the specific circumstances under which the current simulations are conducted. As mentioned in chapter 4 the main contributor to advection of density and heat is the $\mathbf{E} \times \mathbf{B}$ -drift. Furthermore, discussion of interchange motion in chapter 1 revealed how charge-separating

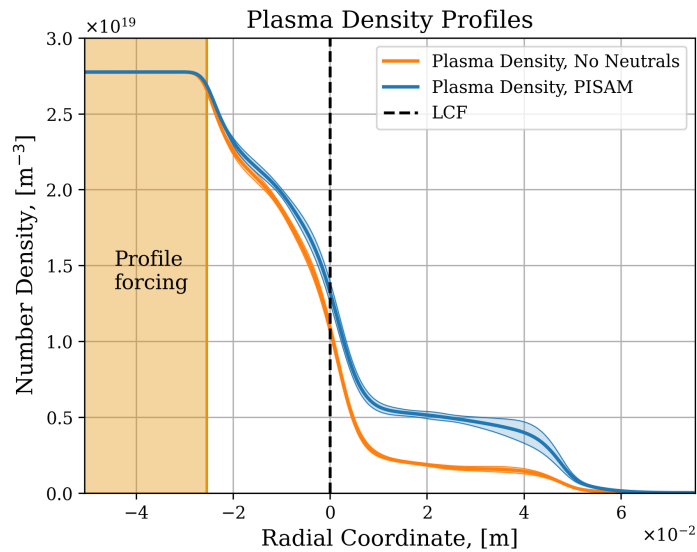


Figure 8.7: Radial density profiles resulting from averaging the plasma density in time and across the poloidal axis.

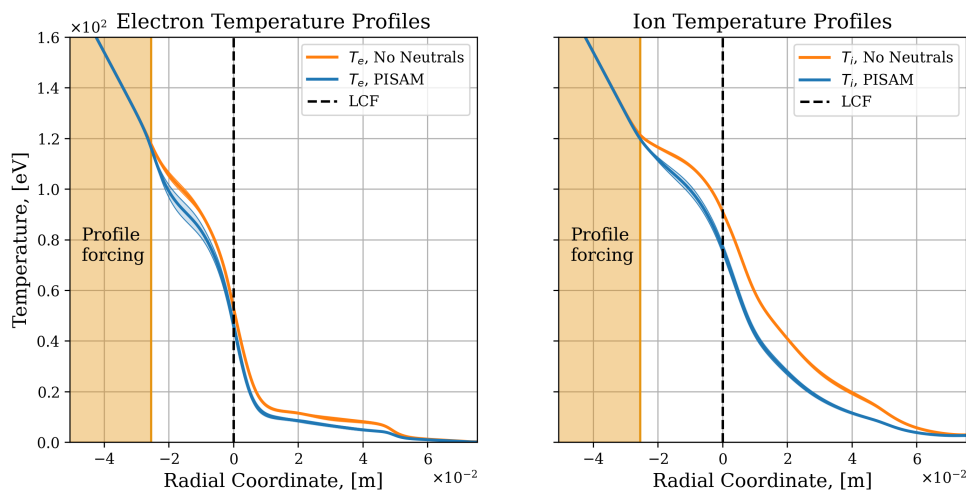


Figure 8.8: Radial temperature profiles resulting from averaging the plasma density in time and over the poloidal axis. The electron and ion temperature profiles are depicted in the left and right figures respectively.

drifts create a poloidal electric field at the outboard midplane giving rise to radial advection. It is thus of interest to investigate the influence of neutrals on the poloidal component of the electric field. Profiles of the poloidal electric field in themselves do however not contribute with interesting information, as averaging this field component in time and over the poloidal axis yields almost exactly zero. Instead, the radial flux reflecting the correlation between perturbations in the poloidal component of the electric field and perturbations in density is considered. The profiles of the radial flux due to $\mathbf{E} \times \mathbf{B}$ -advection are shown in figure 8.10. In the SOL the presence of neutrals is found to increase the particle flux, which is explained by the increased density in the SOL, shown in figure 8.7. The mechanism for decreasing the flux on the inside of the LCFS is not currently fully understood. The Shear-Alfvén law of (1.16) showed that the interchange instability depends on the radial component of the pressure gradient. No significant change to the radial part of the pressure gradients has however been found when adding neutrals. This suggests that either the magnitudes of the perturbations in density and poloidal electric field have decreased or $\sin \phi$, where ϕ is the phase difference between perturbations in density and the component poloidal of the electric field, has decreased. Albeit, density perturbations are expected to be enhanced in the presence of neutrals due to the increased ionization rate in dense regions of the plasma. To understand this puzzling behavior a mode analysis of the density and poloidal electric field perturbations should be performed, to investigate the influence of neutrals on their phase and magnitude.

At the LCFS there is no significant change to the radial flux. Since the ions are colder when neutrals are present as shown in figure 8.8 the energy transport across the LCFS due to $E \times B$ -advection is decreased when neutrals influence the edge plasma. Furthermore, the analysis of the ion energy density source showed how CX atoms carry significant amounts of energy far inside the LCFS. On the other hand, we know that the cooling outside in the SOL will increase the conduction losses of ion energy across the LCFS due to the increased ion temperature gradient. An analysis of the full energy flux across the LCFS with and without neutrals would be interesting to perform using PISAM.

8.4 Neutral Densities

Finally, we shall consider the neutral densities. The profiles of these are shown in figure 8.11. It is interesting to view the atom density profiles knowing that around a fourth of the created atoms escape the domain through the inner

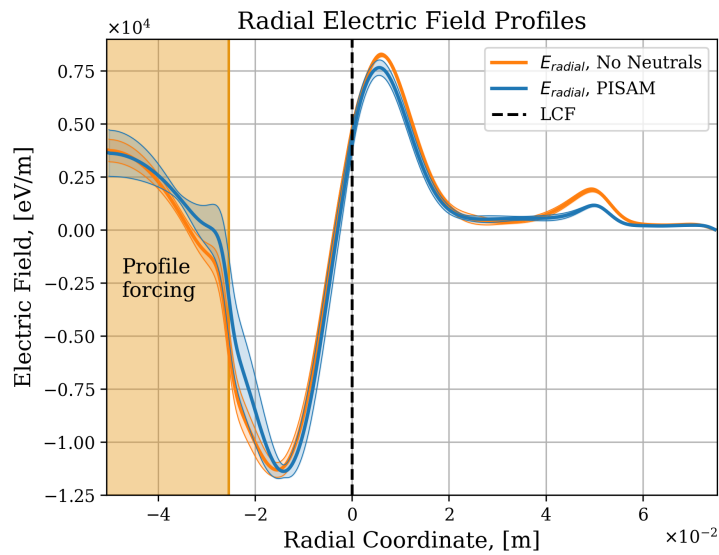


Figure 8.9: Profiles of the radial electric field resulting from averaging in time and over the poloidal axis.

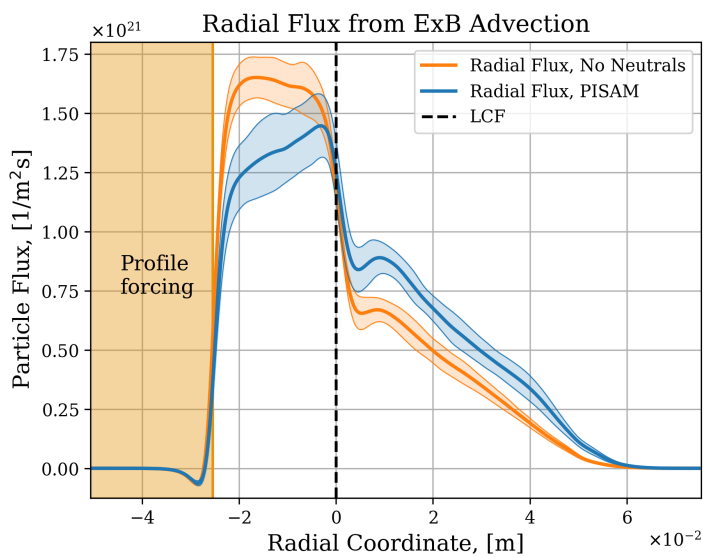


Figure 8.10: Profiles of the radial particle flux resulting from averaging in time and over the poloidal axis.

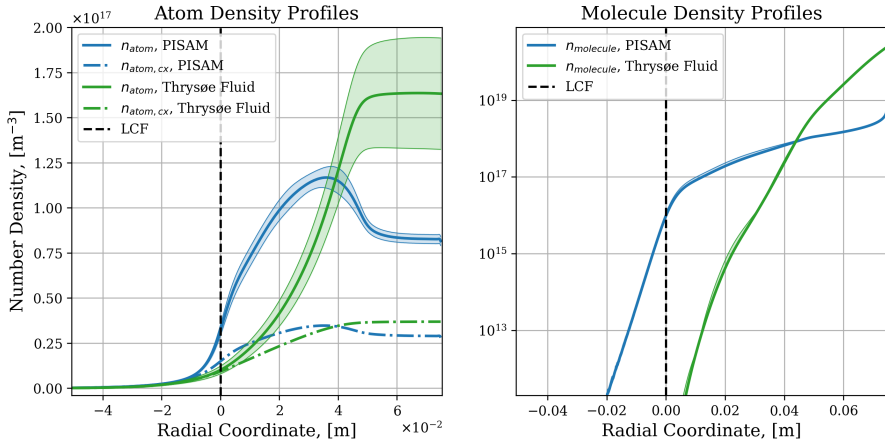


Figure 8.11: Profiles of the neutral densities resulting from averaging in time and over the poloidal axis. The atom densities are depicted on the right while the molecule densities are depicted on the left.

radial boundary. The low density at the boundary indicates that the atoms escaping through the inner radial boundary are moving at significantly greater speeds than the average atoms. Furthermore, it is noted only CX atoms make it further than $\sim 1\text{cm}$ inside the LCFS. Only a few results of the neutral densities in gas puffing experiments at the outboard midplane have been published, none of which are directly comparable to the current simulation. Measurements of the neutral molecule density in gas puffing experiments are expected to be lower near the outer radial boundary than what is shown on the right-hand side of figure 8.11. The reason is that usual gas puffing experiments use room temperature gas ($\sim 0.025\text{eV}$), while this simulation uses an injection temperature of 0.3eV . This does however not alter the density and energy balance equations of (8.5) and (8.7) as these depend on the flux of injected molecules. To know the exact effect of altering the injection temperature, experiments at various injection temperatures would have to be conducted. The expected effects are however discussed in the following chapter. This remark concludes the presentation of the current results of PISAM-HESEL. In the next chapter, the shortcomings of PISAM are presented and the future work to account for these is laid out.

9 Discussion

Many of the decisions in the design of PISAM have already been thoroughly addressed. Two topics regarding the collisions included in PISAM and how they are implemented do however deserve further attention. The first of these concerns the inclusion of multiple vibrational states of $D_2(X^1\Sigma_g^+)$. The second regards the neglection of the fluid velocity when evaluating collision frequencies in (3.4) and (3.11). The considerations on these topics are followed by reflections upon some of the many questions and challenges that arise when a 3D discrete particle model is coupled to a 2D fluid model. These reflections naturally lead to a discussion of the injection temperature of molecules in PISAM-HESEL simulations. At the end of the chapter, the conditions allowing PISAM to be applied in other domains than the outboard midplane of a Tokamak are discussed.

9.1 Including Vibrational States

As mentioned in the presentation of PISAM in chapter 5, only the vibrational ground state of the electronic ground state of D_2 molecules is currently included in the model. The primary channel of molecular dissociation is direct excitation to the unbound $b^3\Sigma_u^+$ state. [134] finds a strong relation between the vibrational state, v , of D_2 and the threshold energy of excitation to $b^3\Sigma_u^+$. Furthermore, the maximum cross sections differ by almost an order of magnitude depending on v . Similarly, the maximum cross sections of excitation to $B^1\Sigma_u^+$, $C^1\Pi_u$, and $D^1\Pi_u$ all differ by around two orders of magnitude depending on v , [103]. Generally, it should thus be expected that dissociation would occur further away from the LCFS than is the case in the current implementation, and thus the electron energy sink due to electron- D_2 would be broadened further outwards in the SOL.

Including all the 21 bound vibrational states of the D_2 -molecule is not in principle technically challenging, as PISAM is designed to ease such implementation. It is also expected that the effect of vibrational states can be implemented in PISAM at fairly low computational costs. The number of

different possible transitions does, however, become very large. Even if only the 2 most probable transitions for each vibrational state are included, 42 new reactions have to be added. The reaction rates of all of these 42 transitions must be known, which in itself demands rigorous research. Furthermore, the effect of wall interactions on the vibrational state must be taken into account when reflections occur, and last but not least the distribution of the vibrational states in the deuterium gas, as it initially enters the reaction chamber, must be known.

9.2 Momentum Transfer Mediated by Neutrals

As described in chapter 3, the fluid velocity is neglected in the evaluation of reaction rates in (3.4) and (3.11). In (3.4), describing the reaction rates of electron-neutral collisions, this is a good approximation due to the large ratio of the deuterium ion and -molecule mass to electron mass. For ions, however, the fluid velocity of the poloidal shear flows characteristic of H-mode can be up to 10% of their thermal velocity. By neglecting the fluid velocity in (3.11) ions are not allowed to transfer a net momentum to the neutrals. If on the other hand, the fluid velocity was taken into consideration in (3.11), charge exchange reactions would contribute with a viscosity-like effect, as the conduction-like effect caused by CX atoms currently seen in figure 8.6. Such a viscosity term is relevant in asserting whether neutrals influence H-mode, as it would act to slow down the poloidal shear flow creating the transport barrier governing H-mode. Allowing for elastic ion-neutral collisions would further contribute to such an effect, but with far less significance than charge exchange reactions, as the momentum transfer cross section is much smaller. In conclusion, for PISAM to be capable of asserting whether neutral injection can cause a transition from H-mode to L-mode the fluid velocity must be accounted for when calculating the velocity distribution of ions going into charge exchange reactions.

9.3 Coupling of Models with Different Dimensionalities

HESEL is considered a 2D model since the fluid velocities are only self-consistently solved for in 2 dimensions while the parallel velocity only enters as damping terms. This poses a problem in the distribution of energy and momentum in plasma-neutral interactions. As evident from (2.14) and (2.21),

proper introduction of the inelastic source terms in the transport equations requires knowledge of the fluid velocity vector \mathbf{u} . As HESEL is 2D the field-aligned component of \mathbf{u} is unknown. To circumvent this lack of knowledge it is assumed that the field-aligned fluid velocity is zero. This is certainly not the case in the SOL where blobs expand with velocities similar to the acoustic velocity [30]. The justification for this assumption is that the average field-aligned fluid velocity in the SOL is expected to be small. If one wishes to secure proper energy and momentum exchange in inelastic collisions, the parallel velocity component must either be approximated explicitly by parameterization or included self consistently in a full 3D model.

9.4 Coupling a Discrete Model with a Continues Model

The very foundation of PISAM-HESEL is that a discrete model can be coupled to a continuous model without violating the governing physics. Even though the validity of this idea seems somewhat intuitive, it is an intricate matter giving rise to the following paradox:

The precision of PISAM increases as the internal time step, including the update of the plasma fields, decreases. The same can be said for the fluid model, where the error in solving the differential equations decreases as the time interval between which the fields and source terms are updated decreases. The paradox is that the same is not true for the coupled model. The reason is the relation between the size of the time step and the statistical noise of the source terms supplied to HESEL by PISAM. In the limit where the time interval between the evaluation of source terms from inelastic plasma-neutral collisions goes towards zero, the source terms passed from PISAM to HESEL tend towards sputtered delta functions, revealing the discrete nature of PISAM. Such source terms are meaningless to apply in a fluid model that is intrinsically continuous, treating all sources as rates determined by local macroscopic properties.

The thorough reflection on the time step size of PISAM, presented in chapter 7, outlined a first approach in seeking a compromise to overcome the challenges resulting from the paradox described above. Given further time and computational resources, a natural next step would be to investigate the convergence of the results of the PISAM-HESEL model, when scanning over various values

of $1/P$ ²⁹.

9.5 Optimal Conditions and Injection Temperature

PISAM is developed to supply source terms from chemical reactions between gas and plasma constituents. The optimal conditions for using PISAM must be viewed in this light. The consequence of the paradox of the previous section is that the time interval between which source terms are evaluated by PISAM should be short enough for the dynamics concerning plasma-neutral interactions to be resolved, but also long enough for smooth sources to be obtained. In a simple case where the parameters determining the reaction rates are approximately uniform, this balance can be expressed from (7.7) as

$$\Delta t_{min} = \frac{W}{n_{n0}\rho_x\rho_y\rho_z n_0 \langle \sigma v \rangle_0 \xi_t^2} < \tau \quad (9.1)$$

Where n_n and n refer to the "particle"-species and the "fluid"-species respectively, the zeros indicate reference quantities at the LCFS, ξ_t is the maximally allowed relative statistic uncertainty, Δt_{min} is the minimum time step satisfying the criterion set by ξ_t , and τ is the characteristic timescale of change of the dynamics of interest. ξ_t would have to be determined by convergence tests. In the following, it is assumed that this value is given. (9.1) states that PISAM must produce a certain amount of reactions in each time step in each grid cell, for the statistical noise of the source term to reach a level that is acceptable in the context of a fluid model. The only parameter in (9.1) that can be adjusted without altering the physical system described is the super particle weight. The numerical complexity of PISAM is $\mathcal{O}(1/W)$, meaning that setting a very low weight requires extensive computational resources. The conclusion is that the reaction rate of the particles modeled by PISAM must be sufficiently high in comparison to the characteristic spatial and temporal rates of change, for PISAM to be an efficient simulation tool. If this condition is not satisfied a lot of numerical resources will be spent on pushing particles around that do not contribute significantly to the physics of interest. This undesirable scenario is realized close to the outer radial boundary when using PISAM at the outboard midplane. To avoid having a lot of molecules build up close to the edge where they are very weakly interacting with the plasma the

²⁹This quantity is defined in chapter 7.

injection temperature has been set to 0.3eV, and the wall boundary condition has been implemented. The effect of this increased temperature is a lower density of molecules at the outer radial boundary and a faster saturation of the system. If the molecules were injected at room temperature instead, a number of changes would occur. The average radial distance of atom creation from the LCFS would increase, causing a decreased flux of, especially non-CX, atoms over the LCFS. Furthermore, the behavior of blobs in the SOL would be affected. If the molecule density in the SOL is higher, the ionization rate around blobs going into the SOL is likewise higher meaning that blobs can be sustained further into the SOL before being diminished by the parallel sink terms. Since saturation would be slower, the next blobs venturing into the same part of the SOL as the former would experience a relatively low molecule density. The variance in blob size is thus expected to be larger at low injection temperatures. The energy balance of (8.7) is however unaffected by the increased temperature as the vast majority of neutral energy is drawn from the plasma. The rate of this plasma-neutral energy exchange almost solely depends on the molecule flux over the outer radial boundary. In conclusion, the qualitative effects of altering the injection temperature can be predicted, but simulation is necessary to assert their significance quantitatively. Low-temperature simulations are however numerically expensive with PISAM which is generally much better suited for the simulation of supersonic molecular beam injection than conventional gas puffing.

9.6 Future Experiments

The convincing results reported above only represent a small glance at the physics possible to uncover with PISAM-HESEL. As the next step, the diagnostics needed to monitor the flux of particles and energy across the LCFS should be implemented. This would allow PISAM to assert the fueling efficiency, especially, in supersonic molecular beam injection, for which PISAM should be perfectly suited, and compare the results to those obtained using a fluid model in [135].

Noting the change of the radial particle flux, ion temperature gradient, and thus energy transport due to the presence of neutrals, it would be natural to analyze the net effect of neutrals on energy confinement. Monitoring the radial energy flux due to the transport of neutrals would allow for such an analysis.

9.7 Beyond the Outboard Midplane and Beyond Fusion Plasma

Currently, the boundary conditions and injection routine of PISAM are specifically set up for the outboard midplane of a Tokamak. This can however fairly easily be altered such that PISAM can be used to describe neutral-plasma interactions in the divertor region, which is currently a subject being extensively researched [136–139]. There is no reason that PISAM should be restricted to use in fusion plasma. In any situation where weakly self-interacting particles are strongly coupled to a fluid model through chemical reactions, a modified version of PISAM can be used to evaluate the effects of such interactions. The coupling method developed as part of this thesis means that PISAM can be coupled to any MPI program, and since it is implemented in Python, writing modifications and extensions to PISAM is easily accessible.

10 Conclusion

For steady-state fusion to be realized the reactor must be fueled while operating, which is achieved by injection of neutrals into the reaction chamber. Furthermore, recycling from the divertors causes transport of neutrals to the plasma edge and SOL. An understanding of the penetration of such neutrals into the plasma is necessary to assert the efficiency of various fueling techniques. Moreover, the neutrals mediate a transport of momentum and energy within the plasma, an effect primarily ascribed to charge exchange reactions. Energy transport across the LCFS mediated by neutrals directly affects the energy confinement time, which is one the most important figures of merit of magnetic fusion reactors. Perhaps more importantly, the neutral-mediated momentum and energy transport is suspected to play a role in transitions from H-mode to L-mode, potentially causing a large decrease in energy confinement time. To address the challenge of investigating neutral transport phenomena in turbulent edge plasma without the need for extensive computational resources, the discrete particle model PISAM has been developed.

This thesis has presented PISAM and the 2D turbulent edge plasma model HESEL in thorough detail, using arguments drawn from first principles. Starting from the Boltzmann equation, the introduction of inelastic neutral source terms in the governing transport equations has been reviewed. These equations were closed by the methods of Braginskii [17]. Braginskii's equations altered with inelastic source terms were further reduced using drift ordering and a parameterization of the parallel velocity, which along with arithmetic simplifications and certain gradient truncations lead to the nHESEL equations. The detail in which these steps were performed revealed several mistakes, regarding higher-order terms, in the previously published nHESEL equations, which this work has served to revise. The main achievement of this thesis is the development and implementation of the discrete particle model PISAM and its MPI coupling to HESEL. The purpose of PISAM is to calculate the inelastic source terms necessary to close the nHESEL equations. The difficulty in building a successful discrete particle model for the current application lies in describing the governing physics in great detail, without creating

a model that is numerically too exhaustive. This is achieved in PISAM by immense research in the field of electron impact on the deuterium molecule. PISAM manages to compress an impressive amount of reaction channels into a numerically light implementation by a clever grouping of reaction channels whenever physically meaningful. By the use of symmetry arguments, PISAM manages to implement energy and momentum conservation without the need to sample over differential cross sections, with the only exception being charge exchange reactions. To deal with these reactions the axial symmetry of CX is utilized to create an extremely effective algorithm that correctly samples ions participating in CX reactions with energetic neutrals in full 3D. Furthermore, all quantum mechanical data, such as state energies and cross sections used in PISAM, originate from the most recent theoretical progress that has been shown to improve the correspondence with measurements.

All these details of PISAM are implemented in Python by the use of fully vectorized `numpy`-code achieving high performance and easy accessibility to other researchers. The embarrassingly parallel nature of PISAM has been utilized to parallelize the implementation to run with an even workload on an arbitrary number of cores. This parallel Python program has been coupled to a C++ implementation of HESEL by the use of MPI intercommunicators. Coupling an MPI parallel Python program with an MPI parallel C++ program in this innovative fashion is in itself pioneering work. The resulting one-of-a-kind solution has been implemented on the HPC cluster Marconi, where PISAM has been successful in running stably on more than 1000 cores while coupled to HESEL also running on multiple nodes.

The founding idea of having a discrete particle model supply sources to a fluid model has been discussed in great detail. Arguments relying on theoretical work as well as simulation data have been used to ensure the validity of the approach. This theoretical work revealed a strong scaling relation of the largest applicable super-particle weight with the magnetic field strength, i.e. $W_{max} \propto B^{-3/2}$.

Results from using PISAM have been reported applying it on static fields, as well as on dynamic fields in coupling with HESEL. These results have provided a persuading verification of PISAM. The results on the static fields are in beautiful correspondence with the prior expectations and furthermore clearly illustrate the transport mechanisms arising when neutrals are injected into the reaction chamber of a fusion reactor.

In presenting the results of PISAM-HESEL these were divided into two groups. Namely, profiles showing the source terms produced by PISAM, and profiles showing the influence of these sources on the plasma fields. The ion

energy density source profile showed a clear inwards radial transport of energy mediated by charge exchange reactions. A similar effect was not produced by the fluid model of [70], indicating that this model lacks energy conservation in the transfer of kinetic energy between plasma and neutrals.

The influence of neutrals on the profiles of plasma density and temperature was found to be in good qualitative agreement with prior measurements and simulation results, [132, 133]. The current simulation results show no disturbance of the poloidal shear flow governing the high containment mode in which the simulated reactor is operating. The ion fluid velocity should however be included when sampling ions going into CX reactions, before drawing conclusions concerning H-mode transitions. On the other hand, the ExB flux resulting from interchange dynamics shows significant changes in most of the simulation domain. Especially the lowered flux on the high field side of the LCFS is an interesting result motivating further investigations.

References

- [1] Valeria Jana Schwanitz and August Wierling. “Toward Sustainable Global Energy Production and Consumption”. In: *Responsible Consumption and Production*. Springer, 2022, pp. 839–850.
- [2] Ashwin Rode et al. “Estimating a social cost of carbon for global energy consumption”. In: *Nature* 598.7880 (2021), pp. 308–314.
- [3] Ahmed Elmelegi et al. “Optimized tilt fractional order cooperative controllers for preserving frequency stability in renewable energy-based power systems”. In: *IEEE Access* 9 (2021), pp. 8261–8277.
- [4] Dainius Genys and Ricardas Krikstolaitis. “Clusterization of public perception of nuclear energy in relation to changing political priorities”. In: *Insights into Regional Development* 2.4 (2020), pp. 750–764.
- [5] Jeffrey P Freidberg. *Plasma physics and fusion energy*. Cambridge university press, 2008.
- [6] Rainer Feldbacher and Manfred Heindler. “Basic cross section data for aneutronic reactor”. In: *Nuclear Instruments and Methods in Physics Research Section A: Accelerators, Spectrometers, Detectors and Associated Equipment* 271.1 (1988), pp. 55–64.
- [7] Larry L Lucas and Michael P Unterweger. “Comprehensive review and critical evaluation of the half-life of tritium”. In: *Journal of research of the National Institute of Standards and Technology* 105.4 (2000), p. 541.
- [8] Marek Rubel. “Fusion neutrons: tritium breeding and impact on wall materials and components of diagnostic systems”. In: *Journal of Fusion Energy* 38.3-4 (2019), pp. 315–329.
- [9] D Fasel and MQ Tran. “Availability of lithium in the context of future D-T fusion reactors”. In: *Fusion engineering and design* 75 (2005), pp. 1163–1168.

- [10] John D Lawson. “Some criteria for a power producing thermonuclear reactor”. In: *Proceedings of the physical society. Section B* 70.1 (1957), p. 6.
- [11] Michael Fitzgerald, Lynton C Appel, and Matthew J Hole. “EFIT tokamak equilibria with toroidal flow and anisotropic pressure using the two-temperature guiding-centre plasma”. In: *Nuclear Fusion* 53.11 (2013), p. 113040.
- [12] *Schematic drawing of Tokamak cross section.* <http://fusionwiki.ciemat.es/fusionwiki/images/5/58/Geometry.png>. [Online; accessed 2-March-2023]. 2023.
- [13] *Schematic drawing of Tokamak.* <https://upload.wikimedia.org/wikipedia/commons/2/2a/Schematic-of-a-tokamak-chamber-and-magnetic-profile.jpg>. [Online; accessed 14-February-2023]. 2023.
- [14] Eugene Curtin. “Another short proof of the hairy ball theorem”. In: *The American Mathematical Monthly* 125.5 (2018), pp. 462–463.
- [15] Lyman Spitzer Jr. “The stellarator concept”. In: *The Physics of Fluids* 1.4 (1958), pp. 253–264.
- [16] U Stroth et al. “Energy confinement scaling from the international stellarator database”. In: *Nuclear Fusion* 36.8 (1996), p. 1063.
- [17] SI Braginskii and MA Leontovich. *Reviews of plasma physics*. 1965.
- [18] AJ Wootton et al. “Fluctuations and anomalous transport in tokamaks”. In: *Physics of Fluids B: Plasma Physics* 2.12 (1990), pp. 2879–2903.
- [19] Paulett C Liewer. “Measurements of microturbulence in tokamaks and comparisons with theories of turbulence and anomalous transport”. In: *Nuclear Fusion* 25.5 (1985), p. 543.
- [20] J Candy and RE Waltz. “Anomalous transport scaling in the DIII-D tokamak matched by supercomputer simulation”. In: *Physical review letters* 91.4 (2003), p. 045001.
- [21] EZ Gusakov et al. “Anomalous transport and multi-scale drift turbulence dynamics in tokamak ohmic discharge as measured by high resolution diagnostics and modeled by full-f gyrokinetic code”. In: *Plasma Physics and Controlled Fusion* 55.12 (2013), p. 124034.

- [22] Fritz Wagner et al. “Regime of improved confinement and high beta in neutral-beam-heated divertor discharges of the ASDEX tokamak”. In: *Physical Review Letters* 49.19 (1982), p. 1408.
- [23] Fritz Wagner. “A quarter-century of H-mode studies”. In: *Plasma Physics and Controlled Fusion* 49.12B (2007), B1.
- [24] KH Burrell. “Effects of $E \times B$ velocity shear and magnetic shear on turbulence and transport in magnetic confinement devices”. In: *Physics of Plasmas* 4.5 (1997), pp. 1499–1518.
- [25] Hamed Biglari, PH Diamond, and PW Terry. “Influence of sheared poloidal rotation on edge turbulence”. In: *Physics of Fluids B: Plasma Physics* 2.1 (1990), pp. 1–4.
- [26] L Schmitz. “The role of turbulence–flow interactions in L-to H-mode transition dynamics: recent progress”. In: *Nuclear Fusion* 57.2 (2017), p. 025003.
- [27] Bogdan Teaca et al. “An overview of dynamical methods for studying transitions between states in sheared plasma flows”. In: *Philosophical Transactions of the Royal Society A* 381.2242 (2023), p. 20210238.
- [28] Z Yan et al. “Turbulence characteristics and flow dynamics impacts on the H-mode transition in favourable magnetic geometry with lower power threshold”. In: *Philosophical Transactions of the Royal Society A* 381.2242 (2023), p. 20210240.
- [29] Yasmin Andrew and Eun-jin Kim. *H-mode transition and pedestal studies*. 2023.
- [30] Jens Madsen et al. “Collisional transport across the magnetic field in drift-fluid models”. In: *Physics of Plasmas* 23.3 (2016), p. 032306.
- [31] W Fundamenski et al. “Dissipative processes in interchange driven scrape-off layer turbulence”. In: *Nuclear fusion* 47.5 (2007), p. 417.
- [32] OE Garcia, NH Bian, and W Fundamenski. “Radial interchange motions of plasma filaments”. In: *Physics of plasmas* 13.8 (2006), p. 082309.
- [33] Robert G Kleva and Parvez N Guzdar. “ β Limit Disruptions in Tokamaks”. In: *Physical review letters* 80.14 (1998), p. 3081.
- [34] Robert G Kleva and Parvez N Guzdar. “Nonlinear stability limit in high β tokamaks”. In: *Physics of Plasmas* 7.4 (2000), pp. 1163–1168.
- [35] Robert G Kleva and Parvez N Guzdar. “Fast disruptions by ballooning mode ridges and fingers in high temperature, low resistivity toroidal plasmas”. In: *Physics of Plasmas* 8.1 (2001), pp. 103–109.

- [36] ED Fredrickson et al. “Ballooning instability precursors to high β disruptions on the Tokamak Fusion Test Reactor”. In: *Physics of Plasmas* 3.7 (1996), pp. 2620–2625.
- [37] Ning Yan et al. “Statistical characterization of turbulence in the boundary plasma of EAST”. In: *Plasma Physics and Controlled Fusion* 55.11 (2013), p. 115007.
- [38] Volker Naulin. “Turbulent transport and the plasma edge”. In: *Journal of nuclear materials* 363 (2007), pp. 24–31.
- [39] JP Graves et al. “Self-similar density turbulence in the TCV tokamak scrape-off layer”. In: *Plasma physics and controlled fusion* 47.3 (2005), p. L1.
- [40] SJ Zweben et al. “High-speed imaging of edge turbulence in NSTX”. In: *Nuclear Fusion* 44.1 (2003), p. 134.
- [41] OE Garcia et al. “Two-dimensional convection and interchange motions in fluids and magnetized plasmas”. In: *Physica Scripta* 2006.T122 (2006), p. 104.
- [42] Richard D Hazeltine and James D Meiss. “Shear-Alfvén dynamics of toroidally confined plasmas”. In: *Physics Reports* 121.1-2 (1985), pp. 1–164.
- [43] Yao Lianghua et al. “Comparison of supersonic molecular beam injection from both low field side and high field side of HL-2A”. In: *Plasma Science and Technology* 12.5 (2010), p. 529.
- [44] CA Foster et al. “Solid hydrogen pellet injection into the Ormak tokamak”. In: *Nuclear Fusion* 17.5 (1977), p. 1067.
- [45] SJ Zweben et al. “Invited Review Article: Gas puff imaging diagnostics of edge plasma turbulence in magnetic fusion devices”. In: *Review of Scientific Instruments* 88.4 (2017), p. 041101.
- [46] F Wagner et al. “Importance of the divertor configuration for attaining the H-regime in ASDEX”. In: *Journal of Nuclear Materials* 121 (1984), pp. 103–113.
- [47] JW Hughes et al. “Edge profile stiffness and insensitivity of the density pedestal to neutral fuelling in Alcator C-Mod edge transport barriers”. In: *Nuclear Fusion* 47.8 (2007), p. 1057.
- [48] M Bernert et al. “The H-mode density limit in the full tungsten ASDEX Upgrade tokamak”. In: *Plasma Physics and Controlled Fusion* 57.1 (2014), p. 014038.

- [49] AR Field et al. “The influence of gas fuelling location on H-mode access in the MAST spherical tokamak”. In: *Plasma physics and controlled fusion* 46.6 (2004), p. 981.
- [50] AR Field et al. “The influence of neutrals on the L/H-transition”. In: *30th EPS Conference on Plasma And Controlled Fusion, Petersburg*. 2003, pp. 7–11.
- [51] Alexander S Thrysoe et al. “The influence of blobs on neutral particles in the scrape-off layer”. In: *Plasma Physics and Controlled Fusion* 58.4 (2016), p. 044010.
- [52] Alexander Simon Thrysoe et al. “Plasma particle sources due to interactions with neutrals in a turbulent scrape-off layer of a toroidally confined plasma”. In: *Physics of Plasmas* 25.3 (2018), p. 032307.
- [53] W Zholobenko et al. “The role of neutral gas in validated global edge turbulence simulations”. In: *Nuclear Fusion* 61.11 (2021), p. 116015.
- [54] Detlev Reiter, Martine Baelmans, and Petra Boerner. “The EIRENE and B2-EIRENE codes”. In: *Fusion science and technology* 47.2 (2005), pp. 172–186.
- [55] R Schneider et al. “B2-EIRENE simulation of ASDEX and ASDEX-Upgrade scrape-off layer plasmas”. In: *Journal of nuclear materials* 196 (1992), pp. 810–815.
- [56] Maarten Blommaert et al. “A spatially hybrid fluid-kinetic neutral model for SOLPS-ITER plasma edge simulations”. In: *Nuclear Materials and Energy* 19 (2019), pp. 28–33.
- [57] Yannick Marandet et al. “Influence of neutral particles on scrape-off layer turbulence with application to the interpretation of fast camera data”. In: *Journal of Nuclear Materials* 438 (2013), S518–S521.
- [58] C Wersal and P Ricci. “A first-principles self-consistent model of plasma turbulence and kinetic neutral dynamics in the tokamak scrape-off layer”. In: *Nuclear Fusion* 55.12 (2015), p. 123014.
- [59] D-M Fan et al. “Self-consistent coupling of the three-dimensional fluid turbulence code TOKAM3X and the kinetic neutrals code EIRENE”. In: *Contributions to Plasma Physics* 58.6-8 (2018), pp. 490–496.
- [60] M Giacomin et al. “The GBS code for the self-consistent simulation of plasma turbulence and kinetic neutral dynamics in the tokamak boundary”. In: *Journal of Computational Physics* 463 (2022), p. 111294.

- [61] Elaine S Oran, CK Oh, and BZ Cybyk. “Direct simulation Monte Carlo: recent advances and applications”. In: *Annual Review of Fluid Mechanics* 30.1 (1998), pp. 403–441.
- [62] John Robert Taylor. *Classical mechanics*. University Science Books, 2005.
- [63] Richard Fitzpatrick. *Physics of Plasmas*. 2016.
- [64] Sydney Chapman and Thomas George Cowling. *The mathematical theory of non-uniform gases: an account of the kinetic theory of viscosity, thermal conduction and diffusion in gases*. Cambridge university press, 1990.
- [65] Hee J Lee. *Fundamentals of Theoretical Plasma Physics: Mathematical Description of Plasma Waves*. World Scientific, 2019.
- [66] Tamas I Gombosi and Atmo Gombosi. *Gaskinetic theory*. Cambridge University Press, 1994.
- [67] Tatsuo Tabata and Toshizo Shirai. “Analytic cross sections for collisions of H+, H2+, H3+, H, H2, and H- with hydrogen molecules”. In: *Atomic Data and Nuclear Data Tables* 76.1 (2000), pp. 1–25.
- [68] Alexander Simon Thryssøe et al. “Gas puff fuelling simulation with a combined neutral/HESEL model”. In: *43rd EPS Conference on Plasma Physics*. 2016.
- [69] F Scotti et al. “Outer midplane neutral density measurements and H-mode fueling studies in NSTX-U”. In: *Nuclear Fusion* 61.3 (2021), p. 036002.
- [70] A. S. Thryssøe. *Influence of neutral particles on edge dynamics of magnetically confined plasmas*. 2018.
- [71] A Zeiler, JF Drake, and B Rogers. “Nonlinear reduced Braginskii equations with ion thermal dynamics in toroidal plasma”. In: *Physics of Plasmas* 4.6 (1997), pp. 2134–2138.
- [72] AI Smolyakov. “Gyroviscous forces in a collisionless plasma with temperature gradients”. In: *Canadian journal of physics* 76.4 (1998), p. 321.
- [73] OE Garcia et al. “Turbulence and intermittent transport at the boundary of magnetized plasmas”. In: *Physics of plasmas* 12.6 (2005), p. 062309.
- [74] D Pfirsch and A Schlüter. “Max Planck Institute Report MPI”. In: *PA/62* (1962).
- [75] Per Helander and Dieter J Sigmar. *Collisional transport in magnetized plasmas*. Vol. 4. Cambridge university press, 2005.

- [76] Anders Henry Nielsen et al. “Numerical simulations of blobs with ion dynamics”. In: *Plasma Physics and Controlled Fusion* 59.2 (2016), p. 025012.
- [77] Lyman Spitzer Jr and Richard Härm. “Transport phenomena in a completely ionized gas”. In: *Physical Review* 89.5 (1953), p. 977.
- [78] Odd Erik Garcia et al. “Fluctuations and transport in the TCV scrape-off layer”. In: *Nuclear fusion* 47.7 (2007), p. 667.
- [79] Ralph Kube et al. “Statistical properties of the plasma fluctuations and turbulent cross-field fluxes in the outboard mid-plane scrape-off layer of Alcator C-Mod”. In: *Nuclear Materials and Energy* 18 (2019), pp. 193–200.
- [80] Ratko K Janev, Detlev Reiter, and Ulrich Samm. *Collision processes in low-temperature hydrogen plasmas*. Vol. 4105. Forschungszentrum, Zentralbibliothek Jülich, 2003.
- [81] IL BeTgman et al. “Collisional de-excitation of metastable levels and the intensities of the resonance doublet components of hydrogen like ions in a laser plasma”. In: *Zh. Eksp. Teor. Fiz.* 71 (1976), pp. 975–983.
- [82] D Reiter et al. “The data file AMJUEL: additional atomic and molecular data for EIRENE”. In: *Forschungszentrum Juelich GmbH* 52425 (2000).
- [83] D Reiter. “The data file HYDHEL: Atomic and Molecular Data for EIRENE”. In: *Forschungszentrum Juelich GmbH* 52425 (2002).
- [84] Wade L Fite et al. “Lifetime of the 2 S State of Atomic Hydrogen”. In: *Physical Review* 116.2 (1959), p. 363.
- [85] Ya F Verolainen and A Ya Nikolaich. “Radiative lifetimes of excited states of atoms”. In: *Soviet Physics Uspekhi* 25.6 (1982), p. 431.
- [86] R Janev et al. “Elementary processes in hydrogen-helium plasmas”. In: *Nuclear Fusion* 28.3 (1988), p. 529.
- [87] D Reiter et al. “The EIRENE code user manual”. In: *Julich KFA Report* (2019).
- [88] G Staszewska and L Wolniewicz. “Transition Moments among 3Σ and 3Π States of the H₂ Molecule”. In: *Journal of molecular spectroscopy* 198.2 (1999), pp. 416–420.
- [89] G Staszewska and L Wolniewicz. “Adiabatic energies of excited $1\Sigma_u$ states of the hydrogen molecule”. In: *Journal of Molecular Spectroscopy* 212.2 (2002), pp. 208–212.

- [90] L Wolniewicz and G Staszewska. “Excited $1\Pi_u$ states and the $1\Pi_u \rightarrow X1\Sigma_g+$ transition moments of the hydrogen molecule”. In: *Journal of Molecular Spectroscopy* 220.1 (2003), pp. 45–51.
- [91] L Wolniewicz and K Dressler. “Adiabatic potential curves and nonadiabatic coupling functions for the first five excited $1\Sigma^+ g$ states of the hydrogen molecule”. In: *The Journal of chemical physics* 100.1 (1994), pp. 444–451.
- [92] L Wolniewicz. “Adiabatic Potentials of the Lowest in $1\Pi_g$ and $1, 3\Delta_g$ States of the Hydrogen Molecule”. In: *Journal of Molecular Spectroscopy* 169.2 (1995), pp. 329–340.
- [93] L Wolniewicz. “Relativistic energies of the ground state of the hydrogen molecule”. In: *The Journal of chemical physics* 99.3 (1993), pp. 1851–1868.
- [94] T Orlikowski, G Staszewska, and L Wolniewicz. “Long range adiabatic potentials and scattering lengths for the EF, e and h states of the hydrogen molecule”. In: *Molecular Physics* 96.10 (1999), pp. 1445–1448.
- [95] Liam H Scarlett et al. “Electron-impact dissociation of molecular hydrogen into neutral fragments”. In: *The European Physical Journal D* 72.2 (2018), pp. 1–8.
- [96] Cynthia S Trevisan and Jonathan Tennyson. “Calculated rates for the electron impact dissociation of molecular hydrogen, deuterium and tritium”. In: *Plasma physics and controlled fusion* 44.7 (2002), p. 1263.
- [97] Xianming Liu et al. “KINETIC ENERGY DISTRIBUTION OF H (1s) FROM H₂ X1Σ⁺ g-a3Σ⁺ g EXCITATION AND LIFETIMES AND TRANSITION PROBABILITIES OF a3Σ⁺ g (v, J)”. In: *The Astrophysical Journal* 716.1 (2010), p. 701.
- [98] Liam H Scarlett et al. “Complete collision data set for electrons scattering on molecular hydrogen and its isotopologues: II. Fully vibrationally-resolved electronic excitation of the isotopologues of H₂ (X1Σg⁺)”. In: *Atomic Data and Nuclear Data Tables* 139 (2021), p. 101403.
- [99] W Kol/os and Lech Wolniewicz. “Potential-Energy Curves for the X 1Σ g⁺, b 3Σ u⁺, and C 1Π u States of the Hydrogen Molecule”. In: *The Journal of Chemical Physics* 43.7 (1965), pp. 2429–2441.
- [100] Daniel A Erwin and Joseph A Kunc. “Rate coefficients for some collisional processes in high-current hydrogen discharges”. In: *IEEE transactions on plasma science* 11.4 (1983), pp. 266–273.

- [101] W Kolos and L Wolniewicz. “Vibrational and rotational energies for the $B\ 1\ \Sigma\ u+$, $C\ 1\ \Pi\ u$, and a $3\ \Sigma\ g+$ states of the hydrogen molecule”. In: *The Journal of Chemical Physics* 48.8 (1968), pp. 3672–3680.
- [102] W Koklos and J Rychlewski. “Ab initio potential energy curves and vibrational levels for the c, l, and i states of the hydrogen molecule”. In: *Journal of Molecular Spectroscopy* 66.3 (1977), pp. 428–440.
- [103] Jonathan K Tapley et al. “Electron-impact dissociative excitation cross sections for singlet states of molecular hydrogen”. In: *Physical Review A* 98.3 (2018), p. 032701.
- [104] Xianming Liu et al. “Electron and photon dissociation cross sections of the D₂ singlet ungerade continua”. In: *Journal of Physics B: Atomic, Molecular and Optical Physics* 45.10 (2012), p. 105203.
- [105] Martin Misakian and Jens C Zorn. “Dissociative excitation of molecular hydrogen by electron impact”. In: *Physical Review A* 6.6 (1972), p. 2180.
- [106] SA Astashkevich and BP Lavrov. “Lifetimes of the electronic-vibrational-rotational states of hydrogen molecule”. In: *Optics and Spectroscopy* 92.6 (2002), pp. 818–850.
- [107] A Pardo. “Radiative lifetimes for the $B1\Sigma u+$ and $C1\Pi u$ states of the H₂ molecule”. In: *Spectrochimica Acta Part A: Molecular and Biomolecular Spectroscopy* 57.5 (2001), pp. 1057–1060.
- [108] H Abgrall et al. “The emission continuum of electron-excited molecular hydrogen”. In: *The Astrophysical Journal* 481.1 (1997), p. 557.
- [109] Jinjun Liu et al. “Determination of the ionization and dissociation energies of the deuterium molecule (D 2)”. In: *The journal of chemical physics* 132.15 (2010), p. 154301.
- [110] Keiji Sawada and Takashi Fujimoto. “Effective ionization and dissociation rate coefficients of molecular hydrogen in plasma”. In: *Journal of applied physics* 78.5 (1995), pp. 2913–2924.
- [111] J Hussels et al. “Improved ionization and dissociation energies of the deuterium molecule”. In: *Physical Review A* 105.2 (2022), p. 022820.
- [112] Dirk Wunderlich and Ursel Fantz. “Franck–Condon factors for molecule–ion reactions of H₂ and its isotopomers”. In: *Atomic Data and Nuclear Data Tables* 97.2 (2011), pp. 152–185.

- [113] Mark C Zammit, Dmitry V Fursa, and Igor Bray. “Electron scattering from the molecular hydrogen ion and its isotopologues”. In: *Physical Review A* 90.2 (2014), p. 022711.
- [114] Liam H Scarlett et al. “Kinetic-energy release of fragments from electron-impact dissociation of the molecular hydrogen ion and its isotopologues”. In: *Physical Review A* 96.2 (2017), p. 022706.
- [115] LH Andersen et al. “Dissociative-recombination and excitation measurements with $H^- n > 2$ and $HD^- s$ ”. In: *Physical Review A* 55.4 (1997), p. 2799.
- [116] MO Abdellahi El Ghazaly et al. “Total cross sections and kinetic energy release for the electron impact dissociation of $H^- 2$ and $D^- 2$ ”. In: *Journal of Physics B: Atomic, Molecular and Optical Physics* 37.12 (2004), p. 2467.
- [117] M Fifirig and M Stroe. “Dissociation of $H^- 2$ ions by collisions with electrons”. In: *Journal of Physics B: Atomic, Molecular and Optical Physics* 44.8 (2011), p. 085202.
- [118] M Landau, RI Hall, and F Pichou. “Proton production from H_2 by electron impact excitation of autoionising states near threshold”. In: *Journal of Physics B: Atomic and Molecular Physics (1968-1987)* 14.9 (1981), p. 1509.
- [119] Jeppe Olsen et al. “Temperature dynamics and velocity scaling laws for interchange driven, warm ion plasma filaments”. In: *Plasma Physics and Controlled Fusion* 58.4 (2016), p. 044011.
- [120] Stefan Van Der Walt, S Chris Colbert, and Gael Varoquaux. “The NumPy array: a structure for efficient numerical computation”. In: *Computing in science & engineering* 13.2 (2011), pp. 22–30.
- [121] BD Dudson et al. “BOUT++: A framework for parallel plasma fluid simulations”. In: *Computer Physics Communications* 180.9 (2009), pp. 1467–1480.
- [122] F Iannone et al. “MARCONI-FUSION: The new high performance computing facility for European nuclear fusion modelling”. In: *Fusion Engineering and Design* 129 (2018), pp. 354–358.
- [123] Zhi-Xin Sun et al. “Proper cell dimension and number of particles per cell for DSMC”. In: *Computers & Fluids* 50.1 (2011), pp. 1–9.

- [124] Michail A Gallis et al. “Convergence behavior of a new DSMC algorithm”. In: *Journal of Computational Physics* 228.12 (2009), pp. 4532–4548.
- [125] Nicolas G Hadjiconstantinou et al. “Statistical error in particle simulations of hydrodynamic phenomena”. In: *Journal of computational physics* 187.1 (2003), pp. 274–297.
- [126] Rafael C Gonzales and Paul Wintz. *Digital image processing*. Addison-Wesley Longman Publishing Co., Inc., 1987.
- [127] Edward A Desloge. “Exchange of energy between gases at different temperatures”. In: *The Physics of Fluids* 5.10 (1962), pp. 1223–1225.
- [128] Peter Banks. “Collision frequencies and energy transfer electrons”. In: *Planetary and Space Science* 14.11 (1966), pp. 1085–1103.
- [129] Jung-Sik Yoon et al. “Electron-impact cross sections for deuterated hydrogen and deuterium molecules”. In: *Reports on Progress in Physics* 73.11 (2010), p. 116401.
- [130] Predrag S Krstic and David R Schultz. “Elastic and vibrationally inelastic slow collisions: H+ H₂, H++ H₂”. In: *Journal of Physics B: Atomic, Molecular and Optical Physics* 32.10 (1999), p. 2415.
- [131] Predrag S Krstić and David R Schultz. “Consistent definitions for, and relationships among, cross sections for elastic scattering of hydrogen ions, atoms, and molecules”. In: *Physical Review A* 60.3 (1999), p. 2118.
- [132] M Agostini et al. “Neutral density estimation in the ASDEX upgrade divertor from deuterium emissivity measurements during detachment and shoulder formation”. In: *Plasma Physics and Controlled Fusion* 61.11 (2019), p. 115001.
- [133] DP Coster et al. “Simulation of the edge plasma in tokamaks”. In: *Physica Scripta* 2004.T108 (2004), p. 7.
- [134] Liam H Scarlett et al. “Isotopic and vibrational-level dependence of H₂ dissociation by electron impact”. In: *Physical Review A* 103.2 (2021), p. L020801.
- [135] G Avdeeva et al. “Influence of injection parameters on fueling efficiency of supersonic molecular beam injection into turbulent fusion plasmas”. In: *Physics of Plasmas* 27.6 (2020), p. 062515.
- [136] Mirko Wensing. *Drift-related transport and plasma-neutral interaction in the TCV divertor*. Tech. rep. EPFL, 2021.

- [137] Niels Horsten et al. “Application of spatially hybrid fluid–kinetic neutral model on JET L-mode plasmas”. In: *Nuclear Materials and Energy* 27 (2021), p. 100969.
- [138] Niels Horsten et al. “Validation of SOLPS-ITER simulations with kinetic, fluid, and hybrid neutral models for JET-ILW low-confinement mode plasmas”. In: *Nuclear Materials and Energy* 33 (2022), p. 101247.
- [139] MS Islam et al. “Simulation of plasma and neutral particles during H gas puffing in the divertor region of GAMMA 10/PDX using the fluid and kinetic neutral code”. In: () .
- [140] D Reiter. “The data file HYDHEL: Atomic and Molecular Data for EIRENE”. In: *Forschungszentrum Juelich GmbH* 52425 (2020).
- [141] EL Vold et al. “The neutral diffusion approximation in a consistent tokamak edge plasma-neutral computation”. In: *Journal of nuclear materials* 176 (1990), pp. 570–577.
- [142] D Schwörer et al. “Influence of plasma background including neutrals on scrape-off layer filaments using 3D simulations”. In: *Nuclear Materials and Energy* 12 (2017), pp. 825–830.

A : Definitions in Kinetic Theory

This appendix introduces the basic entities of density, fluid velocity, temperature, and pressure in the context of kinetic theory.

A.1 Average Macroscopic Variables

Let the phase space distribution function $f_s(\mathbf{r}, \mathbf{v}, t)$ of particle species s , be defined such that the number of particles within the phase space volume $d\mathbf{r}d\mathbf{v}$ at the point $(\mathbf{r}, \mathbf{v}, t)$ is given by

$$f_s(\mathbf{r}, \mathbf{v}, t)d\mathbf{r}d\mathbf{v}. \quad (\text{A.1})$$

It thus follows that the density is obtained by integrating over velocity space, i.e.

$$n_s(\mathbf{r}, t) = \int f_s(\mathbf{r}, \mathbf{v}, t)d\mathbf{v}. \quad (\text{A.2})$$

More generally the mean value, which will also be referred to as the expectation value, $\langle \phi \rangle(\mathbf{r}, t)$, of any physical quantity $\phi(\mathbf{r}, \mathbf{v}, t)$, is defined by

$$\langle \phi \rangle(\mathbf{r}, t) = \frac{1}{n_s(\mathbf{r}, t)} \int \phi(\mathbf{r}, \mathbf{v}, t) f_s(\mathbf{r}, \mathbf{v}, t) d\mathbf{v}. \quad (\text{A.3})$$

In the work presented in this thesis, ϕ will be a tensor of order 0, 1, or 2. In fluid theory the goal is to express the evolution of certain macroscopic quantities i.e. density n , fluid velocity \mathbf{u} and temperature T , by the current state of those exact quantities, where \mathbf{u} and T are defined by

$$\mathbf{u} = \langle \mathbf{v} \rangle = \frac{1}{n} \int \mathbf{v} f d\mathbf{v}, \quad \frac{1}{2} m \langle w^2 \rangle = \frac{m}{2n} \int w^2 f d\mathbf{v} = \frac{3}{2} k T, \quad (\text{A.4})$$

where the random velocity \mathbf{w} is defined as $\mathbf{w} = \mathbf{v} - \mathbf{u}$, and the subscript s as well as the explicit dependence on free parameters have been omitted to ease the notation. Through (A.4) this work employs the kinetic theory definition of temperature as presented, among others, by Chapman and Cowling in [64]. The macroscopic quantities, n , \mathbf{u} , and T are of certain interest as their microscopic counterparts particle number, particle momentum, and particle energy are summational invariants of elastic collisions. A fact that is seen to introduce certain simplifications in the fluid equations derived in chapter 2.

A.2 Generalized Pressure

Following [64] let dS be a small surface element containing the point P within a fluid, and let $\hat{\mathbf{n}}$ be the positive normal unit vector of this surface element. Furthermore, let dS share the motion of the fluid at point P , i.e. let dS have velocity $\mathbf{u}(\mathbf{r}_P, t)$. The pressure \mathbf{p}_n across dS towards its positive side is defined as the rate of flow of momentum across dS per unit area in the positive direction. Through simple geometrical arguments, it is shown that $\mathbf{p}_n = \hat{\mathbf{n}} \cdot \bar{\mathbf{p}}$, where the pressure tensor, $\bar{\mathbf{p}}$, is the expectation value of the random velocity dyad multiplied by mass density, such that

$$\bar{\mathbf{p}}_{ij} = mn\langle w_i w_j \rangle = m \int w_i w_j f d\mathbf{v}. \quad (\text{A.5})$$

The component of the pressure \mathbf{p}_n along $\hat{\mathbf{n}}$ is given by

$$\hat{\mathbf{n}} \cdot \mathbf{p}_n = \bar{\mathbf{p}}_{ij} n_i n_j = \bar{\mathbf{p}} : \hat{\mathbf{n}} \hat{\mathbf{n}}, \quad (\text{A.6})$$

where Einstein notation is used, the notation $\bar{\mathbf{a}} : \bar{\mathbf{b}}$ is used for the double scalar product of second-order tensors, and \mathbf{ab} denotes the dyad formed by the vectors \mathbf{a} and \mathbf{b} . If $\hat{\mathbf{n}}$ is parallel to a coordinate axis, say x, the x-component of the pressure on a surface dS in the yz-plane is

$$\hat{\mathbf{x}} \cdot \mathbf{p}_x = \bar{\mathbf{p}}_{xx} = mn\langle w_x^2 \rangle. \quad (\text{A.7})$$

The sum of normal pressures across three planes parallel to the coordinate planes is thus

$$p_{xx} + p_{yy} + p_{zz} = mn\langle w^2 \rangle. \quad (\text{A.8})$$

As the orientation of the coordinate axes is arbitrary the mean of normal pressures across any three orthogonal planes is

$$p = \frac{1}{3}mn\langle w^2 \rangle = \frac{1}{3}\text{Tr}(\bar{\mathbf{p}}) = nT, \quad (\text{A.9})$$

where $\text{Tr}(\bar{\mathbf{t}})$ is the trace of tensor $\bar{\mathbf{t}}$. p as defined by (A.9) shall be denoted as the scalar pressure. In the last equality of (A.9) the definition of T in (A.4) was used, showing that these formal definitions of p and T give the relation between scalar pressure and temperature known from the ideal gas law.

A.3 The Viscous Stress Tensor

It is practical to divide the pressure tensor into its isotropic and anisotropic parts, thus expressing it as

$$\bar{\mathbf{p}} = p \bar{\mathbf{I}} + \bar{\pi} \quad (\text{A.10})$$

where $\bar{\bar{\mathbf{I}}}$ is the second order unit tensor and the viscous stress tensor $\bar{\bar{\boldsymbol{\pi}}}$ is defined by

$$\bar{\bar{\boldsymbol{\pi}}}_{ij} = \bar{\bar{\mathbf{p}}}_{ij} - p\delta_{ij} = mn\langle w_i w_j - \frac{1}{3}w^2\delta_{ij}\rangle. \quad (\text{A.11})$$

This division is necessary in the simplification of the fluid equations sought when employing a fluid ordering, since the isotropic parts of $\bar{\bar{\mathbf{p}}}$ are usually significantly larger than the anisotropic parts, and hence the drifts arising from these quantities will not contribute to the same order. The reason for this difference in magnitude arises since collisions will drive the distribution function in velocity space toward a Maxwellian, as proven in chapter 3. As a Maxwellian is spherically symmetric around \mathbf{u} the expectation value of odd powers of w_i will be zero if f is purely Maxwellian. Only perturbations to the Maxwellian distribution can contribute to the off-diagonal elements of $\bar{\bar{\boldsymbol{\pi}}}$, and such perturbations are generally assumed to be small for collisional fluids. The notion of a fluid as collisional is specified in the discussion of fluid closure in chapter 4.

B : Derivation of the Boltzmann Collision Operator

The Boltzmann collision operator seeks to describe the rate of change of phase space density due to elastic binary collisions. Consider the phase space distribution function f_i of species i in a composite system consisting of n species belonging to the set $s = \{1, 2, \dots, n\}$. A particle of species i can participate in a binary collision with a particle of any species $j \in s$ including species i itself, which is accounted for by a division of the collision operator

$$\mathcal{E}_i = \sum_{j=0}^n \mathcal{E}_{ij}. \quad (\text{B.1})$$

\mathcal{E}_{ij} gives the rate of change of the phase space density of particle species i due to collisions with particles of species j . In the following, only the derivation of \mathcal{E}_{12} shall be considered. The remaining terms in the collision operator \mathcal{E}_i are obtained from \mathcal{E}_{12} by simple index substitution. Let \mathbf{G} and $\mathbf{g}_{12} = \mathbf{v}_1 - \mathbf{v}_2$ refer to the center of mass velocity and relative velocity of the two colliding particles. Then

$$\mathbf{v}_1 = \mathbf{G} + \frac{\mu}{m_1} \mathbf{g}_{12}, \quad \mathbf{v}_2 = \mathbf{G} - \frac{\mu}{m_2} \mathbf{g}_{12}, \quad (\text{B.2})$$

where μ is the reduced mass. Velocities of particles after a collision shall be denoted by primes, not to be confused with the primes introduced in chapter 3 to denote the neutral frame.

The goal of the following is to determine the net change, N , in the number of particles belonging to the phase space volume $d\mathbf{r}d\mathbf{v}_1$ located at \mathbf{r} , \mathbf{v}_1 , in the short time interval dt , due to collisions between particles of species 1 and 2. This net change is a result of two competing processes. Any particle initially present in $d\mathbf{r}d\mathbf{v}_1$ that participates in a collision during dt will be removed from $d\mathbf{r}d\mathbf{v}_1$ as its velocity is changed as a result of the collision. On the other hand, two particles of species 1 and 2 respectively, both inside the spatial volume $d\mathbf{r}$ have a possibility of colliding such that the velocity \mathbf{v}'_1 of the particle of species 1 after the collision is within the range $\mathbf{v}_1 + d\mathbf{v}_1$, thus increasing the

number of particles in $d\mathbf{r}d\mathbf{v}_1$. The net change of particles in $d\mathbf{r}d\mathbf{v}_1$ is divided into the change caused by each of these processes

$$N = N_+ - N_-.$$
 (B.3)

The collisions contributing to N_- are termed *direct* while those contributing to N_+ are termed *inverse*. To simplify notation, the phase space distribution function $f_s(\mathbf{r}, \mathbf{v}_s, t)$ of species s evaluated at position \mathbf{r} , velocity \mathbf{v}_s and time t shall be denoted f_s . Here \mathbf{v}_s is the velocity of the particle of species s going into a direct collision. Furthermore, the net change in the phase space volume $d\mathbf{r}, d\mathbf{v}_1$ owing to collisions with particles $\mathbf{v}_2, d\mathbf{v}_2$ is denoted dN .

dN_- is easily determined by expanding the argument leading to (3.2). This is accomplished by multiplying (3.2) by the number of particles of species 1 in the phase space volume $\mathbf{v}_1, d\mathbf{v}_1$ i.e. $f_1 d\mathbf{r}d\mathbf{v}_1$. dN_- can thus be written as

$$dN_-(\mathbf{v}_1, \mathbf{v}_2, \chi, \epsilon) = g f_1 f_2 \sigma_{12} d\mathbf{r}d\mathbf{v}_1 d\mathbf{v}_2 dt.$$
 (B.4)

In elastic binary collisions of particles interacting by a central force, $(\mathbf{v}'_1, \mathbf{v}'_2)$ are uniquely determined by $(\mathbf{v}_1, \mathbf{v}_2)$, ϵ and χ . Here ϵ is an azimuthal angle giving the orientation of the plane in which \mathbf{g}_{12} is confined. Momentum and energy conservation ensure that the CM velocity, \mathbf{G} , and the magnitude of the relative velocity, g , are conserved i.e. in the CM frame the collision results merely in a rotation of the relative velocity vector. The angle of this rotation defines χ . Introducing the differential cross section $(\frac{d\sigma}{d\Omega})_{12}$, giving the relative probability of scattering into the solid angle $\sin \chi d\epsilon d\chi$, (B.4) can be rewritten to yield

$$dN_- = \int_0^\pi \sin \chi d\chi \int_0^{2\pi} d\epsilon \left(\frac{d\sigma}{d\Omega} \right)_{12} g f_1 f_2 d\mathbf{r}d\mathbf{v}_1 d\mathbf{v}_2 dt.$$
 (B.5)

To get the total number of collisions where a particle of species 1 has initial velocity \mathbf{v}_1 , dN_- is integrated over all velocities \mathbf{v}_2 yielding

$$N_- = d\mathbf{r}d\mathbf{v}_1 dt \int d\mathbf{v}_2 \int_0^\pi \sin \chi d\chi \int_0^{2\pi} d\epsilon \left(\frac{d\sigma}{d\Omega} \right)_{12} u f_1 f_2.$$
 (B.6)

To determine N_+ the symmetry of direct and inverse encounters is exploited. For each direct collision specified by the quantities $(\mathbf{v}_1, \mathbf{v}_2, \mathbf{v}'_1, \mathbf{v}'_2)$, there is a corresponding inverse collision $(\mathbf{v}'_1, \mathbf{v}'_2, \mathbf{v}_1, \mathbf{v}_2)$, with the same χ and ϵ and thus the same differential cross section, [64]. Let $\mathbf{v}'_1, d\mathbf{v}'_1$ and $\mathbf{v}'_2, d\mathbf{v}'_2$ be velocity ranges, such that each collision with initial velocities in the ranges $\mathbf{v}_1, d\mathbf{v}_1$ and $\mathbf{v}_2, d\mathbf{v}_2$ specified by χ, ϵ result in velocities within $\mathbf{v}'_1, d\mathbf{v}'_1$ and $\mathbf{v}'_2, d\mathbf{v}'_2$. Given the transformation of (B.2) and the fact that \mathbf{g}_{12} is merely rotated during an

elastic binary collision, with the rotation specified by χ and ϵ , it is clear that a unique mapping between $(\mathbf{v}_1, \mathbf{v}_2)$ and $(\mathbf{v}'_1, \mathbf{v}'_2)$ exists when χ and ϵ are specified. It can be shown that the determinant of the Jacobian of the coordinate transformation defined by this mapping is unity i.e. $d\mathbf{v}_1 d\mathbf{v}_2 = d\mathbf{v}'_1 d\mathbf{v}'_2$. The number of inverse collisions defined by $(\mathbf{v}'_1, \mathbf{v}'_2, \chi, \epsilon)$, such that the relative velocity is rotated into the orientation of the direct collision, happening within $d\mathbf{r}$ during dt is thus given by

$$g f'_1 f'_2 \left(\frac{d\sigma}{d\Omega} \right)_{12} \sin \chi d\epsilon d\chi d\mathbf{r} d\mathbf{v}_1 d\mathbf{v}_2 dt, \quad (\text{B.7})$$

such that dN_+ can be written in analogy with (B.5) as

$$dN_+ = \int_0^\pi \sin \chi d\chi \int_0^{2\pi} d\epsilon \left(\frac{d\sigma}{d\Omega} \right)_{12} g f'_1 f'_2 d\mathbf{r} d\mathbf{v}_1 d\mathbf{v}_2 dt, \quad (\text{B.8})$$

where f'_1 is read $f_1(\mathbf{r}, \mathbf{v}'_1(\mathbf{v}_1, \mathbf{v}_2, \chi, \epsilon), t)$. N_+ is obtained by integration over the unit sphere and all velocities \mathbf{v}_2

$$N_+ = d\mathbf{r} d\mathbf{v}_1 dt \int d\mathbf{v}_2 \int_0^\pi \sin \chi d\chi \int_0^{2\pi} d\epsilon \left(\frac{d\sigma}{d\Omega} \right)_{12} g f'_1 f'_2. \quad (\text{B.9})$$

The Boltzmann collision operator of collisions between particles of species 1 and 2 is now obtained by combining (B.3), (B.6), (B.9), and dividing by $d\mathbf{r} d\mathbf{v}_1 dt$ to get the change of particles in phase space at $\mathbf{r}, \mathbf{v}_1, t$ per unit phase space volume per unit time

$$\mathcal{E}_{12}(\mathbf{r}, \mathbf{v}_1, t) = \int d\mathbf{v}_2 \int_0^\pi \sin \chi d\chi \int_0^{2\pi} d\epsilon \left(\frac{d\sigma}{d\Omega} \right)_{12} g(f'_1 f'_2 - f_1 f_2). \quad (\text{B.10})$$

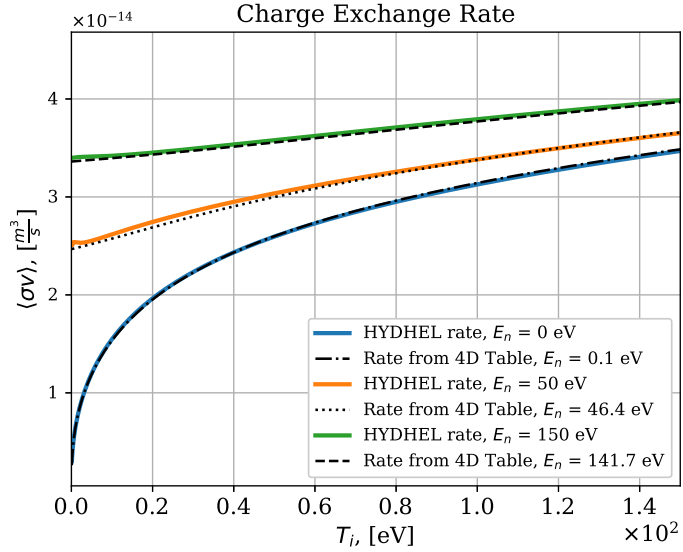


Figure C.1: The CX reaction rate of a deuterium atom with energy E_n from the HYDHEL database plotted as solid lines, along with the reaction rates calculated using the 4D distribution obtained from calculating the integrand of C.1.

C : Asymmetry of Charge Exchange Reactions

As described in chapters 3 and 5 charge exchange reactions should be treated with specific care for two reasons. Firstly, since the colliding particles have similar mass resulting in a significant momentum exchange, which due to the spatial asymmetry of charge exchange reactions is not expected to cancel when averaging over many collisions. Secondly, the energy and momentum exchange, in CX reactions, is strongly dependent on the velocity of the reacting particles, meaning that the distribution of the velocities of ions going into charge exchange reactions must be determined. The method for determining this distribution was outlined in chapter 5. This appendix will validate the approach and show relevant speed- and angular distributions and their dependence on ion temperature and neutral energy.

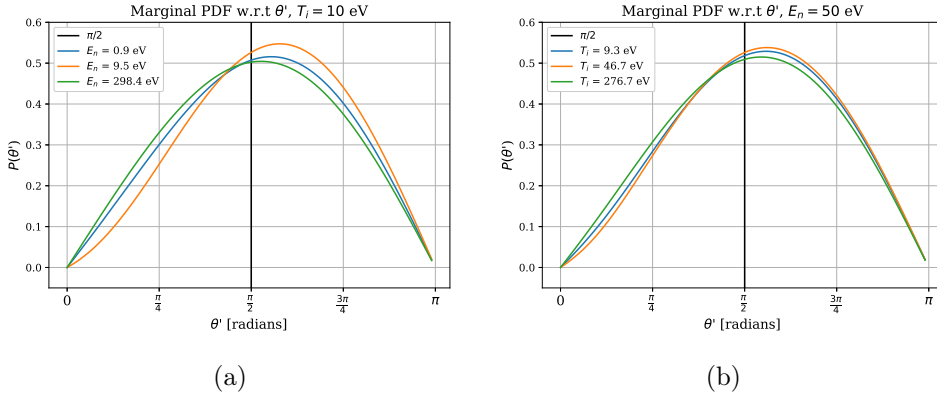


Figure C.2: The marginal probability distribution with respect to θ' at various neutral energies, E_n , and ion temperatures, T_i . In (a) the ion temperature is kept constant at 10 eV, while (b) shows results obtained at a constant neutral energy of 50 eV. The black line shows $\pi/2$ to give a sense of the asymmetry.

C.1 Validation

To validate the 4D CX reaction rate distribution obtained from calculating the integrand of 3.13, the total reaction rates obtained at a number of different temperatures and energies have been calculated by summing over the contributions from all ion velocities w_i and poloidal angles θ'^{30} . These total reaction rates are plotted in figure C.1 along with the reaction rates given as a polynomial fit in the database HYDHEL [140], which is the rates used for CX in the EIRENE code as well as in PISAM. Figure C.1 shows a convincing correspondence between the total reaction rate calculated from summing over the 4D CX reaction rate distribution, and the fit given in HYDHEL, thus providing a solid validation of the calculations.

C.2 Asymmetry

Figure C.2 shows the marginal probability distribution of velocities going into CX reactions, with respect to θ' , at various neutral energies, E_n , and ion temperatures, T_i . If the neutral energy is neglected as in (3.4) these distributions would be symmetrical around $\pi/2$. Albeit a slight bias towards the high θ' -side is seen in figure C.2. This bias is most significant in situations where the ion temperature and neutral energy are equal. The symmetry is equally restored for $T_i \gg E_n$ and $T_i \ll E_n$. Generally, the effect of monitoring

³⁰See figure 3.1

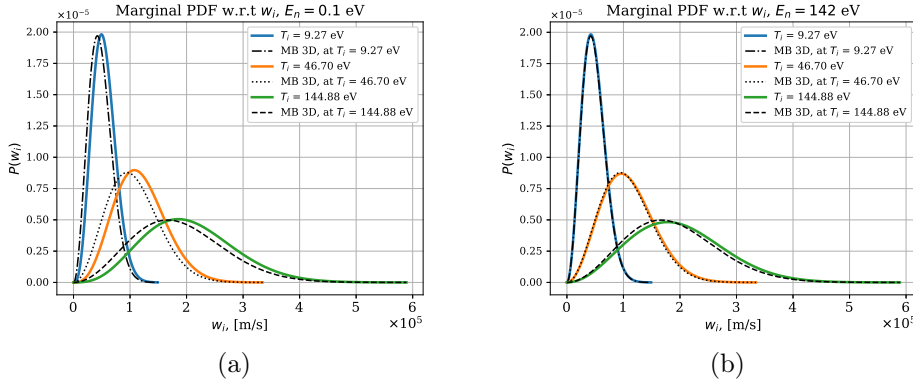


Figure C.3: The marginal probability distribution with respect to w_i at various neutral energies, E_n , and ion temperatures, T_i . In (a) the neutral energy is kept constant at 0.1 eV, while (b) shows results for a constant neutral energy of 142 eV. The black lines show the Maxwell-Boltzmann speed distribution at the corresponding temperature.

the deflection angles in CX is seen to be quite small. It is however an important feature to investigate as it is common in the literature to model the transport of CX neutrals by diffusion, as in [141] and [142]. If however, one found highly asymmetric distributions of the deflection angle θ' , in CX reactions, meaning that neutrals would have a tendency to turn around in each CX reaction, the CX atoms would exhibit something inherently different than a random walk, and thus the diffusion model might not be justified. Figure C.3 shows the marginal probability density function with respect to the ion random velocity w_i , along with the Maxwell-Boltzmann distributions defined by the corresponding ion temperatures. 3(a) gives the marginal PDFs for a low neutral energy of $E_n = 0.1\text{eV}$ at various ion temperatures. As expected the distribution of ions going into charge exchange reactions is shifted towards higher velocities as compared to the corresponding Maxwell-Boltzmann distribution. 3(a) gives the marginal PDFs for the high neutral energy $E_n = 142\text{eV}$ at varying temperatures. Only the distribution representing comparable ion and neutral energies is shifted with respect to the corresponding MB distribution. The reasoning is that when E_n is large in comparison with the ion temperature, the vast majority of collisions happen due to the speed of the neutral particle itself, not the ion speed. The neutral particle bumps into the ions, which are practically standing still from the neutral's point of view.

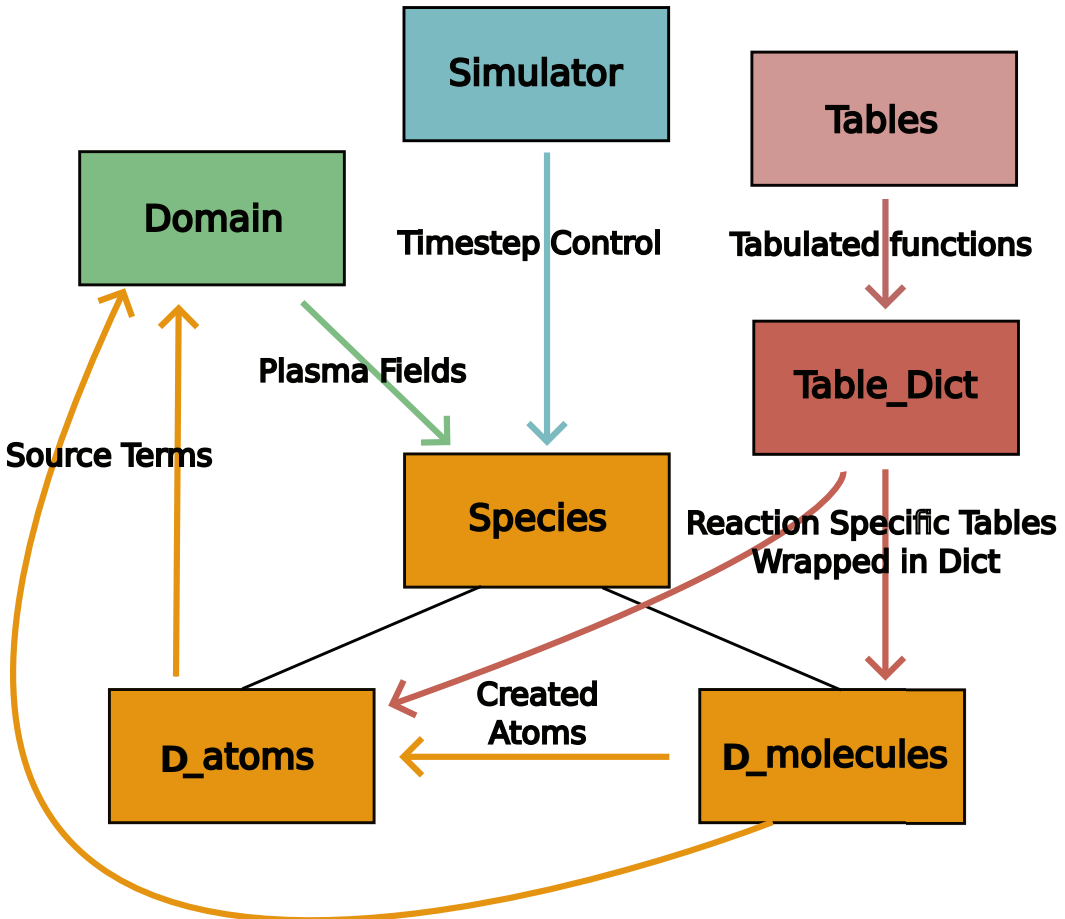


Figure D.1: This diagram shows the most important design features regarding the structure of the implementation of PISAM. The boxes represent Python classes, with equal coloring indicating inheritance. The colored arrows represent the exchange of information between the classes.

D : Design of the PISAM Implementation

In designing the implementation of PISAM there have been two main focus points; 1) Maximizing performance and 2) making it easy to add further particles and reactions. These are accomplished by an object-oriented approach demanding each type of particle to provide certain information and implement certain methods. A diagram of the overall structure of the implementation is shown in figure D.1. The colored arrows represent the most important information exchange between the classes of which PISAM consists. Below, a brief presentation of each class and its functionality is reviewed:

- **Species:**

The species class is the main class of PISAM. It holds the minimal attributes required for each type of particle added to the system e.g. mass, inflow rate, inflow temperature, etc. Furthermore, it stores the positions, velocities, and surrounding temperatures for each particle of the species it represents.

It implements the `step()` function called for each species in each time step. This function outlines all the processes making up a simulation timestep.

```

1  def step(self):
2      #Get initial positions and velocities of new particles flowing
3      #into the system in this timestep.
4      new_xs, new_ys, new_vxs, new_vys, new_vzs = self.init_pos_vs()
5      #Inject the particles, filling the vacant parts of memory
6      #where information about removed particles reside.
7      self.inflow(new_xs, new_ys, new_vxs, new_vys, new_vzs)
8      #Get the indices of the grid cell of the plasma simulation
9      #That each particle is in.
10     self.set_plasma_inds()
11     #Read the fields surrounding each particle
12     self.set_Te()
13     self.set_Ti()
14     self.set_n()
15     #Calculate the rates of each reaction for each particle
16     #based on the relevant field values and tables.
17     self.get_rates()
18     #calculate the probability of reacting
19     self.probs_arr[:, 0:self.max_ind] =
20     self.get_probs_from_rates(self.probs_arr[:, 0:self.max_ind])
21     #For each particle determine what reactions happen if any,
22     #by sampling using uniform random numbers.
23     specify_interaction = self.calc_interaction(self.probs_arr)
24     #Perform the interactions. This involves removing and breeding
25     #new particles, calculating the source terms, etc.
26     self.do_interaction(specify_interaction)
27     #Move the particles according to their speed and apply
28     #the relevant boundary conditions.
29     self.translate()

```

- **D_atoms and D_molecules:**

These are both sub-classes of `Species`, and serve to implement the characteristics of the reactions of atoms and molecules respectively i.e. the rate of each reaction, and the actions performed in each collision.

- **Domain:**

The `Domain` class holds all the information that is domain specific rather than particle specific. The `Domain` thus monitors the values of the plasma fields n , T_e , and T_i and makes this information accessible to each instance of `Species`. Furthermore, `Domain` stores the source terms obtained in each time step on a grid equal in shape to the grid of the plasma simulation. `Domain` also keeps track of the total time passed in the simulation which is used in the synchronization with HESEL.

- **Tables and Table_Dict:**

The `Tables` class implements a number of different tables. These all store discrete numerical data in up to four dimensions. The data is sampled from functions representing reaction rates, fragment kinetic energy distributions, etc. The reason for creating such tables rather than using splines representing the relevant functions is the large overhead from calculating each required value using splines. As the probability of each reaction for each particle has to be evaluated at each time step, the performance of this part of the program is paramount. Many of the tables are logarithmically rather than linearly sampled to get precise function descriptions using a minimal amount of data points. Due to this irregularity, all `Tables` implement a `get_indices()` function that returns the indices along a dimension d given an array of values along that dimension, allowing users to read table data safely and efficiently. The `Table_Dict` class is a wrapper class for `Tables`, storing the large number of tables used by each species in a single object to increase readability and flexibility.

- **Simulator:**

The `Simulator` class controls all the processes in a full simulation. It instantiates `Domain` and any instance of `Species` applied in the simulation and finalizes the simulation by saving the data obtained during the simulation, as well as the state of the `Domain` and `Species` objects at simulation end. `Simulator` is responsible for exchanging the necessary information with the binding layer between PISAM and HESEL, making it possible to synchronize the temporal evolution of PISAM and HESEL.